Ph.D. DISSERTATION

Study of the Electrode Effects
on Ferroelectric Hf$_{0.5}$Zr$_{0.5}$O$_2$ Thin Film

by

Young Hwan Lee

February 2020

DEPARTMENT OF MATERIALS SCIENCE AND ENGINEERING

COLLEGE OF ENGINEERING

SEOUL NATIONAL UNIVERSITY

Study of the Electrode Effects
on Ferroelectric Hf$_{0.5}$Zr$_{0.5}$O$_2$ Thin Film

Advisor : Prof. Cheol Seong Hwang

by

Young Hwan Lee

A thesis submitted to the Graduate Faculty of Seoul National
University in partial fulfillment of the requirements for the
Degree of Doctor of Philosophy
Department of Materials Science and Engineering
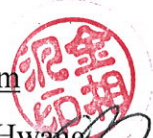
February 2020

Approved

by

Chairman of Advisory Committee : Sang Bum Kim

Vice-chairman of Advisory Committee : Cheol Seong Hwang

Advisory Committee : Jin Young Kim

Advisory Committee : Min Hyuk Park

Advisory Committee : Yu Jin Kim

Abstract

Ferroelectricity of doped HfO_2 was first reported in 2011 by NaMLab in Dresden, Germany. Ever since the discovery of the unprecedented ferroelectric orthorhombic $Pca2_1$ phase in doped HfO_2, a number of research have been conducted. Unlike conventional ferroelectric perovskite materials, which show degraded ferroelectric property under certain critical thickness, fluorite structured-doped HfO_2 maintains its property under few nm thickness, which is a high gain in terms of scaling and three dimensional structure. Its Si compatibility is another intriguing factor for manufacturing. Numerous studies have been conducted to find the origin of ferroelectric orthorhombic phase within doped HfO_2, including effects from film thickness, dopant type, annealing condition, top electrode presence. A number of studies on the first principle calculation based on thermodynamics have been also conducted. However, very few research has been conducted on the kinetics and bottom electrode effect, on which this dissertation aims to emphasize.

Finding the origin of the unprecedented ferroelectricity within doped HfO_2 has suffered from a serious gap between its theoretical calculation, mostly based on thermodynamic approach. To fill the gap, the first part of the dissertation proposes to consider the kinetic energy, providing the evidence of the kinetic energy barrier upon a phase transformation from the tetragonal phase to the monoclinic phase affected by the TiN top electrode (capping layer). 10 nm thick $Hf_{0.5}Zr_{0.5}O_2$ thin films were

deposited and annealed with or without the TiN capping layer with subsequent annealing at different time and temperature. Arrhenius plot is constructed to obtain the activation energy for the tetragonal-to-monoclinic phase transformation by calculating the amount of the transformed phase using X-ray diffraction pattern. Johnson–Mehl–Avrami and nucleation-limited transformation models are utilized to describe the characteristic nucleation and growth time and calculate the activation energy for the monoclinic phase transformation of the $Hf_{0.5}Zr_{0.5}O_2$ thin film. Both models demonstrate that the TiN capping layer provides a kinetic energy barrier for tetragonal-to-monoclinic phase transformation and enhances the ferroelectric property.

The second part of the dissertation explains the bottom electrode effect, especially Ru electrode. Ru has been reported to be oxidized to RuO_2 during initial atomic layer deposition process when using O_3 for oxidant. This formation of RuO_2 layer on Ru electrode is expected to act as a layer to hinder the growth of a non-ferroelectric monoclinic phase and promote the tetragonal phase formation, which can transform into a metastable ferroelectric orthorhombic phase. It turned out that $Hf_{0.5}Zr_{0.5}O_2$ thin film is crystallized on Ru electrode aided by the formation of RuO_2 layer at as-deposited condition without any further post-annealing process. As-deposited film, however, showed high leakage current and endurance problem, which required further annealing, which caused Ru diffusion into the dielectric layer and degraded the ferroelectric property. Without the post-annealing process, ~10 nm $Hf_{0.5}Zr_{0.5}O_2$

thin film produced a large amount of orthorhombic phases which aided in high remnant polarization of ~17 $\mu C/cm^2$ at 4 MV/cm with ~10^8 endurance cycling.

Student Number: 2016-38100

                           Young Hwan Lee

Table of Contents

List of Tables

List of Figures

List of Abbreviations

FE	Ferroelectric
P_r	Remnant polarization
m-phase	Monoclinic phase
o-phase	Orthorhombic phase
ALD	Atomic layer deposition
t-phase	Tetragonal phase
XRD	X-ray diffraction
HZO	$Hf_{0.5}Zr_{0.5}O_2$
TE	Top electrode
JMA	John-Mehl-Avrami
NLT	Nucleation limited transformation
BE	Bottom electrode
AO	Al_2O_3
CSD	Chemical solution deposition
NLS	Nucleation-limited switching
PMA	Post-metallization annealing
PDA	Post-deposition annealing

RTA	Kolmogorov–Avrami–Ishibashi (KAI)
SEM	Scanning electron microscope
AES	Auger electron spectroscopy
CVD	Chemical vapor deposition
GPC	Growth per cycle
XRD	X-ray diffraction

1. Introduction

1.1. Ferroelectric Doped-HfO₂ Thin Film

Ferroelectricity was first reported in Rochelle salt by Valasek in the early 1920s, and it has been utilized in various applications such as microelectromechanical systems (MEMS), radio frequency identification (RFID) chips, and semiconductor memory devices.[1-3] Ferroelectric (FE) materials possess two remnant polarization states $\pm P_r$ even when the electric field is removed, and these two states can be assigned to "0" and "1" states for memory applications.[3] Most of the conventional FE thin films are based on perovskite structured materials, like $Pb(Zr,Ti)O_3$ (PZT), $BaTiO_3$ (BTO), and $SrBi_2Ta_2O_9$ (SBT).[3] However, they did not show high interface quality on Si substrate which results in an interfacial SiO_2 layer leading to formation of depolarization field, weakening two stable polarization states. In general, these conventional ferroelectric materials have several weaknesses which include relatively small electrical bandgap (E_g of 3-4 eV), making them vulnerable to leakage current and electrical breakdown.[3] Therefore, relatively large film thickness (t_f~100nm) is required for charge-based FeRAM, which is a huge demerit for fabrication of three-dimensional capacitor structures with a technology node of a few tens of nanometers.[4] Also, relatively weak bonding energy of oxygen with the constituent

metal ions generates defects like oxygen vacancies, which is the cause of fatigue, imprint and retention problems.[5] In addition, Pb in PZT is environmentally hazardous which brings the attention to developing new lead-free FE materials that are compatible with Si and possess large E_g, P_r, and high bonding energy between metal ions and oxygen.

Fluorite structured HfO_2 is of special interest because it is a simple binary oxide with high P_r at low film thickness of few nm depending on dopants and possesses energy gap of ~5.3-5.7 eV.[6] HfO_2 is usually in monoclinic phase (m-phase) which is non-FE. The ferroelectricity of HfO_2 arises from Pca2$_1$ orthorhombic phase (o-phase) due to its non-centrosymmetric lattice structure. When the electric field is applied, oxygen ions shift within the lattice resulting in ion displacement and internal dipole, as is shown in Figure 1.1. When the electric field is removed, the oxygen ions stay where they were, having certain P_r value. Its maximum remnant polarization values vary with different dopants such as Si, Zr, Y, Al, Gd, Sr, and La.[7-26] The P_r values of the HfO_2-based films are usually in the range of 15-25 $\mu C/cm^2$ for Si-, Al-, Gd-, Zr- and Sr-doped films and La-doped HfO_2 films exhibit a maximum P_r value of ~ 40 $\mu C/cm^2$ at a thickness of ~10 nm, using highly matured deposition techniques such as atomic layer deposition (ALD).[27] The realization of FE property depends on various factors. Film thickness, grain size, asymmetric stress, dopants, top capping and annealing. Although it is not definite of which factor outruns the other, their effects intermingle to result in more enhanced ferroelectricity.
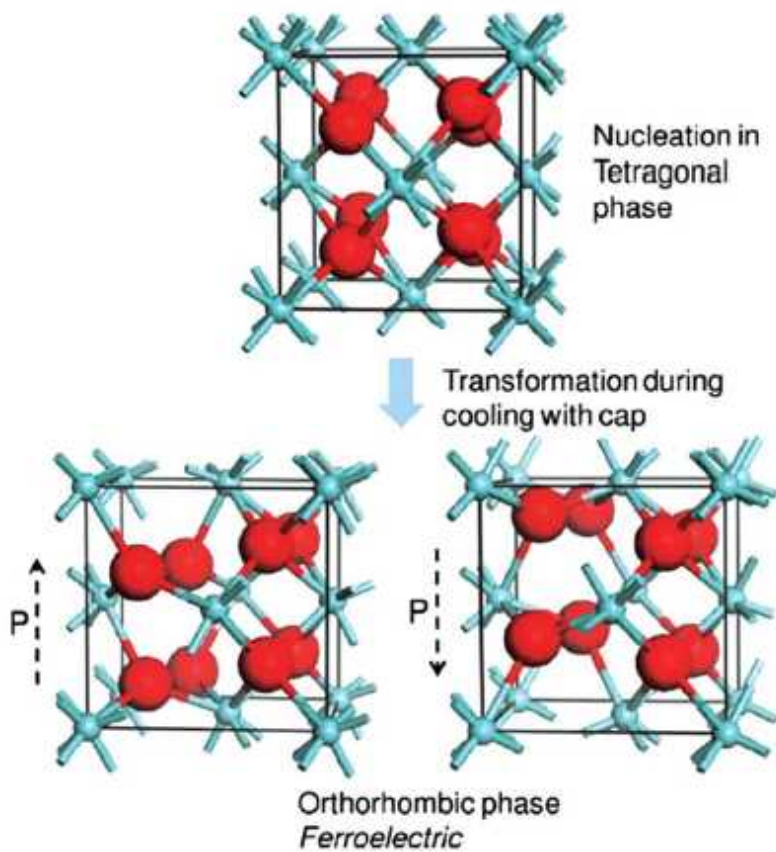
Figure 1.1. Formation of ferroelectric orthorhombic phase with and without top electrode capping. Oxygen ions which are in red create displacement when the field is applied which creates dipole moment leading to polarization. [6]

1.2. Objective and Chapter Overview

The objective of this dissertation focuses on the top and bottom electrode effect on FE Zr-doped HfO_2.

Chapter 2 contains the literature studies on the external factors affecting the FE property of doped-HfO_2 thin film. Literature study in depth on top and bottom electrode effect is included.

Chapter 3 discusses on the presence of a kinetic energy barrier upon phase transformation from metastable tetragonal (t-phase) or o-phase to bulk stable m-phase. Phase evaluation is mainly conducted using X-ray diffraction (XRD) of $Hf_{0.5}Zr_{0.5}O_2$ (HZO) thin film with and without TiN top electrode (TE). Classical Johnson-Mehl-Avrami (JMA) model is applied with limitation of using such model for polycrystalline HZO film. Then, new nucleation limited transformation (NLT) model is proposed to describe the nucleation and growth behavior of HZO film. It turned out that TiN TE capping layer induces higher activation energy barrier for the phase transformation to the m-phase, and it not only slows down the nucleation of the m-phase but also disperses its nucleation time in HZO thin film.

Chapter 4 covers the Ru bottom electrode (BE) effect on HZO thin film. Formation of RuO_2 layer between the Ru metal and oxide layer during initial ALD process hinders the m-phase formation but promotes the metastable t-phase, which can potentially phase transform to the FE o-phase. HZO thin film showed a FE behavior

at as-deposited state with $2P_r$ of ~33 μC/cm^2, which has never been reported on Ru electrode. However, it showed high leakage current which rendered poor endurance performance. Insertion of Al_2O_3 (AO) suppressed the leakage current but fatigue problem was still present. When frequency was varied, the film showed $2P_r$ value of 17 μC/cm^2 at cycling number of 10^8.

Finally, in chapter 5, the conclusion of the dissertation is made.

1.3. Bibliography

1. J. Valasek, Phys. Rev. 15, 527 (1920).

2. J. Valasek, Phys. Rev. 17, 475 (1921).

3. J. F. Scott, Ferroelectric Memories, Springer-Verlag, Berlin, Germany (2000).

4. D. S. Jeong , R. Thomas , R. S. Katiyar , J. F. Scott , H. Kohlstedt , A. Petraru , C. S. Hwang , *Rep. Prog. Phys. 75* , 076502 (2012).

5. N. Setter , D. Damjanovic , L. Eng , G. Fox , S. Gevorgian, S. Hong , A. Kingon , H. Kohlstedt , N. Y. Park , G. B. Stephenson, I. Stolitchnov , A. K. Taganstev , D. V. Taylor , T. Yamada , S. Streiffer, *J. Appl. Phys. 100* , 051606 (2006).

6. T. S. Böscke , J. Müller , D. Bräuhaus , U. Schröder , U. Böttger , *Appl. Phys. Lett. 99* , 102903 (2011).

7. U. Schroeder , E. Yurchuk , J. Müller , D. Martin , T. Schenk , P. Polakowski , C. Adelmann , M. I. Popovici , S. V. Kalinin , T. Mikolajick , *Jpn. J. Appl. Phys. 53* , 08LE02 (2014).

8. T. S. Böscke , St. Teichert , D. Bräuhaus , J. Müller , U. Schröder , U. Böttger , T. Mikolajick , *Appl. Phys. Lett. 99* , 112904 (2011).

9. D. Zhou , J. Müller , J. Xu , S. Knebel , D. Bräuhaus , U. Schröder , *Appl. Phys. Lett. 100* , 082905 (2012).

10. D. Zhou , J. Xu , Q. Lu , Y. Guan , F. Cao , X. Dong , J. Müller , T. Schenk , U. Schröder , *Appl. Phys. Lett. 103* , 192904 (2013).

11. E. Yurchuk , J. Müller , S. Knebel , J. Sundqvist , A. P. Graham , T. Melde , U. Schröder , T. Mikolajick , *Thin Solid Films 533* , 88 (2013).

12. P. D. Lomenzo , P. Zhao , Q. Takmeel , S. Moghaddam , T. Nishida , M. Nelson , C. M. Fancher , E. D. Grimley , X. Sang , J. M. LeBeau , J. L. Jones , *J. Vac. Sci. Technol. B 32* , 03D123 (2014).

13. J. Müller , T. S. Böscke , D. Bräuhaus , U. Schröder , U. Böttger , J. Sundqvist , P. Kücher , T. Mikolajick , L. Frey , *Appl. Phys. Lett. 99* , 112901 (2012).

14. J. Müller , T. S. Böscke , U. Schröder , S. Mueller , D. Bräuhaus , U. Böttger , L. Frey , T. Mikolajick , *Nano Lett. 12* , 4318 (2012).

15. M. H. Park , H. J. Kim , Y. J. Kim , W. Lee , H. K. Kim , C. S. Hwang , *Appl. Phys. Lett. 102* , 112914 (2013).

16. M. H. Park , H. J. Kim , Y. J. Kim , W. Lee , T. Moon , C. S. Hwang , *Appl. Phys. Lett. 102* , 242905 (2013).

17. M. H. Park , H. J. Kim , Y. J. Kim , T. Moon , C. S. Hwang , *Appl. Phys. Lett. 104* , 072901 (2014).

18. M. H. Park , H. J. Kim , Y. J. Kim , W. Jeon , T. Moon , C. S. Hwang , *Phys. Status Solidi RRL 8* , 532 (2014).

19. M. H. Park , H. J. Kim , Y. J. Kim , W. Lee , T. Moon , K. D. Kim , C. S. Hwang , *Appl. Phys. Lett. 105* , 072902 (2014).

20. J. Müller , U. Schröder , T. S. Böscke , I. Müller , U. Böttger , L. Wilde , J. Sundqvist , M. Lemberger , P. Kücher , T. Mikolajick , L. Frey , *J. Appl. Phys. 110* , 114113 (2011).

21. T. Olsen , U. Schröder , S. Müller , A. Krause , D. Martin , A. Singh , J. Müller , M. Geidel , T. Mikolajick , *Appl. Phys. Lett. 101* , 082905 (2012).

22. S. Starschich , D. Griesche , T. Schneller , R. Waser , U. Böttger , *Appl. Phys. Lett. 104* , 202903 (2014).

23. S. Mueller , J. Mueller , A. Singh , S. Riedel , J. Sundqvist , U. Schroeder , T. Mikolajick , *Adv. Funct. Mater. 22* , 2412 (2012).

24. P. Polakowski, S. Riedel, W. Weinreich, M. Rudolf, J. Sundqvist, K. Seidel , J. Müller , in *Proc. IEEE 6th International Memory Workshop* 1 (2014).

25. S. Mueller, C. Adelmann, A. Singh, S. V. Elshocht, U. Schroeder, T. Mikolajick , *ECS J. Solid St. Sci. 1* , N123 (2012).

26. T. Schenk, S. Mueller, U. Schroeder, R. Materlik, A. Kersch, M. Popovici , C. Adelmann , S. V. Elshocht , T. Mikolajick , in *Proc. Eur. Solid-State Device Res.Conf.* 260 (2013).

27. C. S. Hwang , *Atomic Layer Deposition for Semiconductors* , Springer, New York, USA (**2013**).

2. Literature

2.1. External Factors Affecting Ferroelectricity of Doped-HfO$_2$

The FE property of doped HfO$_2$ strongly depends on the film thickness and corresponding grain size since it is generally known that film thickness and temperature budget affect the average grain size. Yurchuk et al. first reported a decrease of P$_r$ as the film thickness gets thicker, which comes together with crystallization during deposition leading to m-phase formation.[1] Park et al. also pointed out on the FE property dependency on film thickness for HZO films.[2] They varied the thickness from 5.5 to 25 nm and annealing temperature from 400 to 800 °C, and figured out that the film showed the highest P$_r$ value of 15 μC/cm^2 at a film thickness of ~10 nm.[2] Its P$_r$ value decreased to ~12 and ~5 μC/cm^2 as film thickness increased to 17 and 25 nm, respectively, which might have come from the m-phase formation as the film thickness gets thicker.[1]

It is known that grain size of the polycrystalline HfO$_2$ and ZrO$_2$ thin film has large impact on the phase stabilization at a given thickness. The critical grain size to obtain a t-phase is known to be ~4 nm and ~32 nm for HfO$_2$ and ZrO$_2$, respectively, which gives the critical grain size of HZO about ~18 nm using the Vegard's law.[3,4] Under this critical grain size, HZO thin film would be able to obtain the t-phase induced by

the surface or grain boundary effect. Although doped HfO_2 films grown by ALD seem to show the critical thickness of ~20 nm over which the m-phase starts to dominate, considering that Y-doped HfO_2 grown by chemical solution deposition (CSD) show FE characteristic up to film thickness of 70 nm, the actual limitation of thickness cannot be clearly defined.

The asymmetric stress that is applied to the doped HfO_2 film can also affect the phase formation. Park et al. have examined on the c/a ratio of the t-phase and the 2b/(a+c) ratio of the o-phase of the bulk HfO_2 and ZrO_2. It should be noted that the lattice parameter of the c-axis of the o-phase, the polarization direction, is the shortest, whereas the nonpolar b-axis is the longest. For the t-phase, on the other hand, the c-axis is the longest lattice parameter, which makes the c-axis of the t-phase corresponding to the b-axis of the o-phase upon the phase transition. Hence, the 2b/(a+c) ratios of the o-phase (of both HfO_2 and ZrO_2) becomes higher than c/a ratios of the t-phase. Also, the difference between the 2b/(a+c) ratio of the o-phase and c/a ratio of the t-phase were higher for ZrO_2 (1.015–1.016 for the t-phase and 1.036 for the o-phase, differed by ~2 %) than that of HfO_2 (1.028–1.029 for the t-phase and 1.038 for the o-phase, differed by ~1 %). [5-7] Therefore, transition from the t- to o-phase requires much higher stress (~4 GPa) for ZrO_2 than HfO_2. Park et al. calculated the strain along a-, b-, and c-axis of the grains of various orientations using the in-plane stress conditions of the thin film. [2] as a result, the 110-orientation was the most favorable for the formation of the oIII-phase from t-phase, whereas the 111-

orientation was the worst, since almost equivalent strains were formed along the a-, b-, and c-axis (none of the a-, b-, and c-directions can be tensile while other direction is compressive). This was indeed the case in an experiment on the HZO prepared by ALD process on the highly 111-oriented Pt electrode, which resulted in the highly 111-oriented film. [2] with no polarization value due to symmetrically applied stress. In contrast, the HZO film simultaneously grown on a TiN electrode showed no preferred orientation, and feasible P–E hysteresis, revealing the FE performance (Figure 2.1).
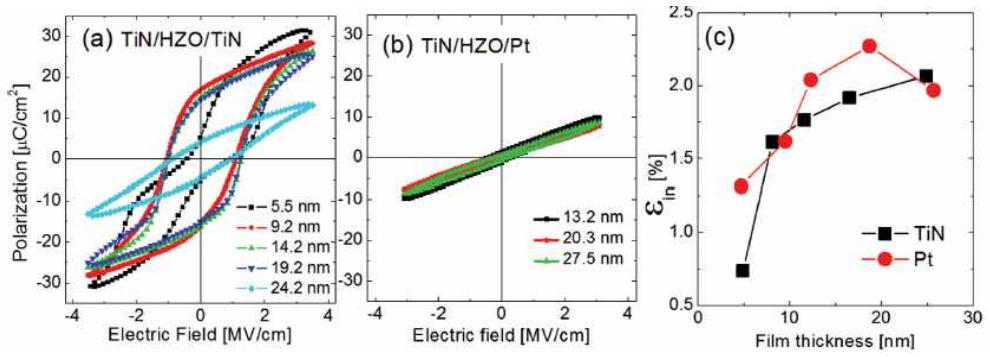
Figure 2.1 ~10 nm $Hf_{0.5}Zr_{0.5}O_2$ film on (a) TiN and (b) Pt. (c) calculation of in-plane strain on different electrodes.[2]

2.2. Top Electrode Capping Effect

The FE o-phase is the metastable phase that is stable under certain condition. Boscke et al. explained that TE capping avoids shearing and volume expansion of the unit cell during the crystallization process. [1] As shown in the Fig. 2.2, when there is a TE capping, the t-phase can transform to the o-phase while non-capping induces the m-phase. When the annealing temperature rises, the t-phase becomes stable, and when the temperature drops to room temperature, according to the thermodynamic point of view, the m-phase should be the stable phase without considering the surface energy effect at thin films of ~10 nm. Since t-phase to m-phase transition requires volume expansion and shearing effect, if the capping layer hinders such effect, then the t-phase may become stable which can potentially transform into the FE o-phase.

Cao et al. reported on the effects of various capping electrode on FE properties of $Hf_{0.5}Zr_{0.5}O_2$ thin films. [8] Authors explained that P_r value of FE capacitors with different TE demonstrated increase trend as the thermal expansion coefficient of the electrode decreases. Also, asymmetry in top and bottom electrodes with different work function caused internal bias and shifted the hysteresis. As shown in Fig. 2.3.

Kim et al. reported that the thickness of the TE can also affect FE behavior of HZO thin film, as shown in Fig. 2.4.[9] Fig. 2.4 shows the P-E hysteresis curves of HZO thin film deposited on TiN BE with and without TE during annealing process. It can be seen that the film does not show ferroelectricity when there is no capping during

annealing process, indicating that a large portion of the m-phase is grown. On the other hand, when there is a TE capping layer, the ferroelectricity can be clearly seen. Also, as the thickness of the TiN TE becomes thicker, FE behavior is enhanced. This is due to the large mechanical stress from the TiN TE working as a tensile stressor on the HZO film during the annealing process.

Park et al. compared the TiN and RuO_2 TE on ~10 nm HZO thin films. [10] RuO_2 TE was expected to enhance the FE behavior of HZO thin film because conducting oxide electrodes are known to enhance the fatigue behavior. [11-14] However, when post-annealing process was conducted, diffusion of Pt and Ru top electrode degraded ferroelectric property, as shown in Fig. 2.5. Also the reduction of RuO_2 TE by the chemical reaction with the reactive TiN BE was one of the causes for ferroelectricity degradation.
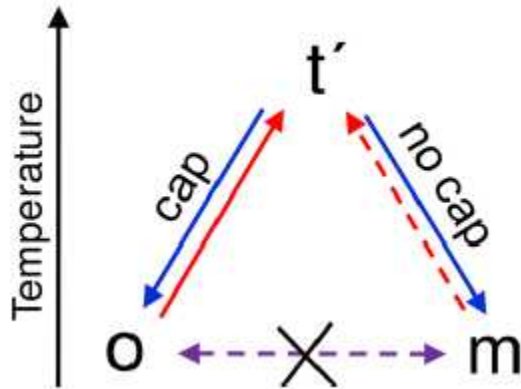
Figure 2.2. Schematic diagram representing experimentally observed transitions between the ferroelectric orthorhombic phase, anti-ferroelectric tetragonal phase and non-ferroelectric monoclinic phase.[1]
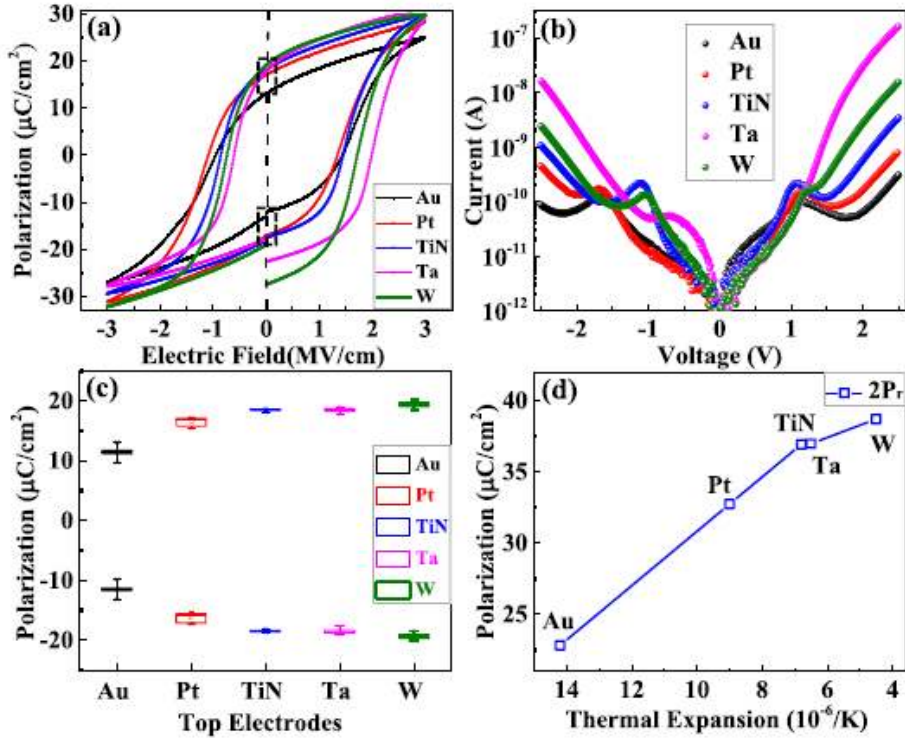
Figure 2.3 (a) polarization hysteresis loops (b) current-voltage and (c) statistical results of +/- remnant polarization value. (d) summary of $2P_r$ as a function of the alpha, thermal expansion coefficient of top electrode for $Hf_{0.5}Zr_{0.5}O_2$ ferroelectric capacitors with Au, Pt, TiN, Ta, W top electrode, respectively.[8]
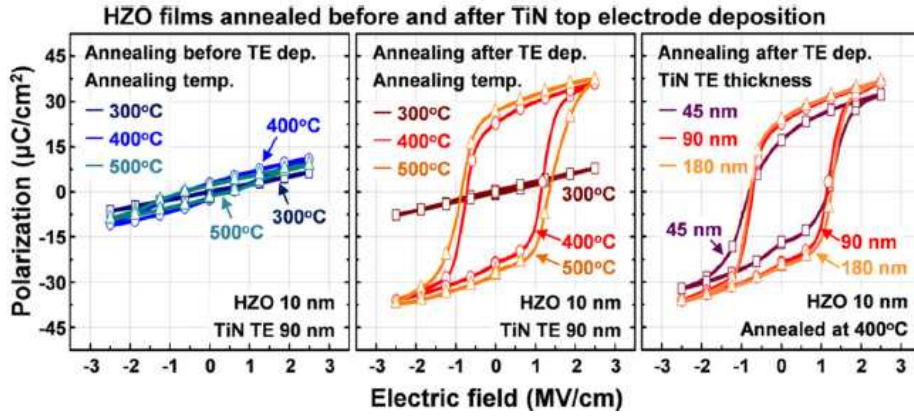
Figure 2.4. Polarization-electric field curves of 10-nm-thick HZO-based metal-insulator-metal (MIM) capacitors after wake-up field cycling (10^5 cycles at 2.5MV/cm) annealed at 300 °C to 500 °C before and after TiN top electrode deposition
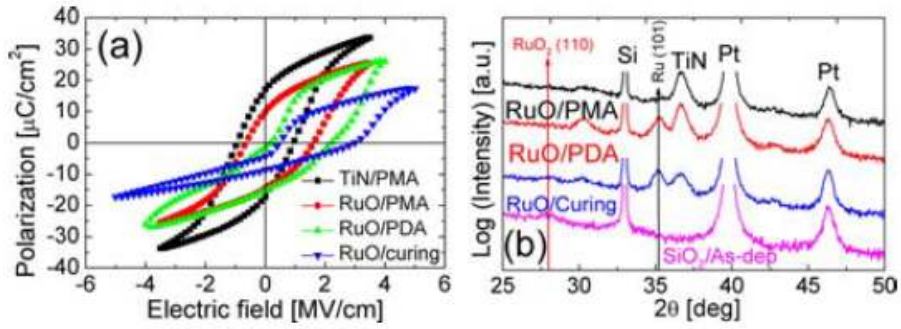
Figure 2.5. Polarization-electric field curves of 10.5-nm-thick $Hf_{0.5}Zr_{0.5}O_2$ capacitors with a TiN and RuO_2 top electrode with various annealing conditions. (b) Glancing-incidence angle X-ray diffraction spectra of the $Hf_{0.5}Zr_{0.5}O_2$ and SiO_2 films with an RuO_2 top layer with various annealing conditions.

2.3. Choice of Bottom Electrode

As covered in Chapter 2.2, the TE has large influence on the FE property of HZO thin film. The BE has a large impact as well. Various studies have shown that FE property is easily seen on TiN BEs. Although HZO thin film possesses amorphous phase at as-deposited state, it crystallizes to the anti-FE t-phase or FE o-phase as post-annealing process follows. Although TiN is widely chosen as the BE, other choices of electrodes are studied as well.

Fig. 2.6 shows that different substrates renders different electrical properties. It is due to the compressive/tensile stress that is applied to the dielectric layer during anneealing process. This in-plane tensile strain is necessary for the phase transformation from the t-phase to the o-phase. [15] The FE properties were enhanced with decreasing thermal expansion coefficient, with the largest P_r value being obtained on the SiO_2 substrate.

Also, Park et al. reported on the FE property of HZO thin films on Ir electrode as well. [16] The critical thickness to show FE behavior degraded fast on Ir BE. This was due to the oxygen supply from IrO_x to HZO layer during initial ALD process which cuased the formation of smaller in-plane tensile strain and larger grain size of the HZO films. As a result, different growth behavior was observed which resulted in different evolution of phases as the film grows.

There was a report on ferroelectricity of ZrO_2 monolayer on Pt electrode without post-annealing process.[17] ~10 nm ZrO_2 thin film usually shows anti-FE behavior as t-phase becomes stable.[18] Also, HZO thin film grown by ALD process on Pt usually does not show FE behavior due to the symmetric in-plane strain that is applied to the film.[19] In this report, remote plasma ALD growth at 300 ℃ provided sufficient heat and thermal stresses during the deposition stage to induce the t- to o- phase transformation in nanoscale ZrO_2 thin films on Pt electrode.
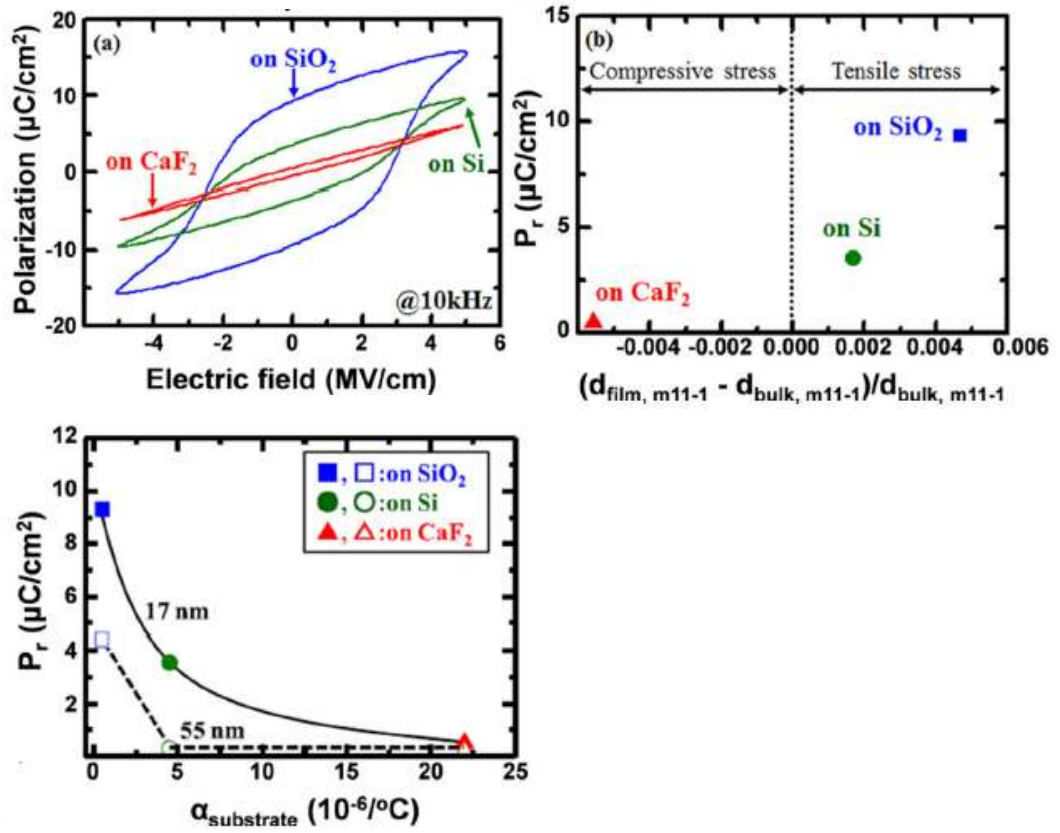
Figure 2.6 (a) Polarization-electric field hysteresis curves, (b) remnant polarization and deviation of the lattice spacing and (c) thermal expansion coefficient of the substrate dependence of P_r of $Hf_{0.5}Zr_{0.5}O_2$ films deposited on SiO_2, Si, and CaF_2 substrates.
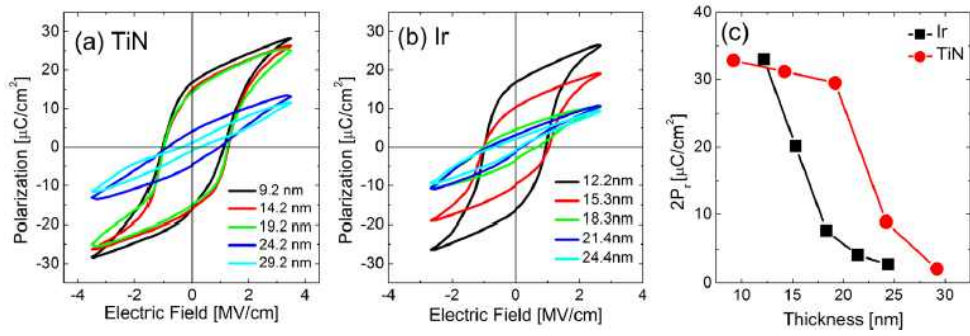
Figure 2.7. Polarization-electric field hysteresis curves of $Hf_{0.5}Zr_{0.5}O_2$ thin film with different thickness on (a) TiN and (b) Ir. (c) change in $2P_r$ with respect to the thickness of $Hf_{0.5}Zr_{0.5}O_2$ thin film.

2.4. Bibliography

1. T. S. Böscke , St. Teichert , D. Bräuhaus , J. Müller , U. Schröder , U. Böttger , T. Mikolajick , Appl. Phys. Lett. 99, 112904 (2011).

2. M. H. Park , H. J. Kim , Y. J. Kim , T. Moon , C. S. Hwang , Appl. Phys. Lett. 104, 072901 (2014).

3. M. W. Pitcher , S. V. Ushakov , A. Navrotsky , B. F. Woodfi eld , G. Li , J. Boerio-Goates , J. Am. Ceram. Soc. 88, 160 (2005).

4. M. Shandalov , P. C. Mclntyre , J. Appl. Phys. 2009 , 106 , 084322. 5. M. V. Nevitt , Y. Fang , S. K. Chan , J . Am. Ceram. Soc. 7, 3, 2502 (1990).

6. T. Tojo , T. Atake , T. Mori , H. Yamamura , J. Chem. Thermodyn. 31, 831 (1999).

7. J. E. Jaffe , R. A. Bachorz , M. Gutowski , Phys. Rev. B 72, 144107 (2005).

8. R. Cao, Y. Wang, S. Zhao, Y. Yang, X. Zhao, W. Wang, X. Zhang, H. Lv, Q. Liu, M. Liu IEEE Electron Device Letters 39, 8 (2018)

9. S. J. Kim, J. Mohan, S. R. Summerfelt, J. Kim Journal of the Minerals 71, 1 (2019)

10. M. H. Park, H. J. Kim, Y. J. Kim, W. Jeon, T. Moon, C. S. Hwang Phys. Status Solidi RRL, 1-4 (2014)

11. C. B. Eom et al., Appl. Phys. Lett. 63, 2570 (1993).

12. J. F. Scott and M. Dawber, Appl. Phys. Lett. 76, 3801 (2000).

13. I. K. Yoo and S. B. Desu, Phys. Status Solidi A 133, 565 (1992).

14. J. J. Lee, C. L. Thio, and S. B. Desu, J. Appl. Phys. 78, 5073 (1995).

15. M. H. Park, H. J. Kim, Y. J. Kim, T. Moon, C. S. Hwang Appl. Phys. Lett. 104, 072901 (2014)

16. M. H. Park, H. J. Kim, Y. J. Kim, W. Lee, T. Moon, K. D. Kim, C. S. Hwang Appl. Phys. Lett 105, 072902 (2014)

17. B-T. Lin, Y-W. Lu, J. Shieh, M-J. Chen Journal of the European Ceramic Society 37, 1135 (2017)

18. J. Muller, T. S. Boscke, U. Schroder, S. Mueller, D. Brauhaus, U. Bottger, L. Frey, T. Mikolajick Nano Lett. 12, 4318 (2012)

19. M. H. Park, H. J. Kim, Y. J. kim, W. Lee, H. K. Kim, C. S. Hwang Appl. Phys. Lett. 102, 112914 (2013)

3. Nucleation-limited Ferroelectric Orthorhombic Phase Formation in Hf$_{0.5}$Zr$_{0.5}$O$_2$ Thin Films

3.1. Introduction

Numerous studies have been conducted to find the origin of ferroelectricity in doped- or undoped-HfO$_2$, and (Hf,Zr)O$_2$ is the material with high advantage in device scaling by possessing a high remnant polarization (P_r) value at a thickness of ~10 nm.[1–7] It is also completely complementary metal-oxide-semiconductor compatible and can be grown by highly matured atomic layer deposition (ALD) techniques as thin films. Unprecedented ferroelectricity in HfO$_2$ can only occur when a non-centrosymmetric orthorhombic phase (o-phase, space group: $Pca2_1$) is present, and its formation has been reported to be highly influenced by various factors such as film thickness, stress, capping layer, annealing temperature, and time, or type of dopants.[5,8–12] Not one of these factors dominates the others and critically influences the formation of the FE o-phase, but they intermingle to determine the final phase formation.

A number of computational researches have attempted to simulate the experimental results by employing such factors into the modeling based on the density functional theory. These works adopted mostly the thermodynamic approach, to more accurately

comprehend the ferroelectricity phenomena within doped- or undoped-HfO_2 thin films. These efforts sprouted from the fact that the emergence of the FE o-phase cannot be solely explained by the bulk free energy. Materlik et al. calculated the Gibbs/Helmholtz free energy of the stable phase under a given condition by engaging the stress and strain effect, combined with the surface energy contribution to stabilizing the o-phase.[1] They suggested that the bulk and surface free energies of the o-phase are in between those of the tetragonal phase (t-phase, space group: $P4_2/nmc$) and monoclinic phase (m-phase, space group: $P2_1/c$) and that there exist a specific film thickness and grain size range for the o-phase stabilization. For HfO_2 and $Hf_{0.5}Zr_{0.5}O_2$ (HZO) thin films, the thickness ranges for the o-phase stabilization were 3–5 and 7–15 nm, respectively. Batra et al. sorted out appropriate dopants which induce ferroelectricity in HfO_2 materials by using the first principles calculation and concluded that dopants with larger ionic radii and lower electronegativity favor the polar *Pca*2_1 o-phase.[13] Kunneth et al. explored the influence of the grain surface interlayer on the interface free energy model by exploiting the grain radius distribution.[3] In that report, they concluded that the thermodynamic model, employing the film composition and size effects from the surface or interface energy, is not sufficient to fit the experimental observations and requires the inclusion of several other factors into the model.[3]

Recently, Park et al. commented on the discrepancy between the theoretical expectation and experimental results and presented that the phase transition kinetics

during the cooling step may be the potential key factor to fill the gap. [14] They pointed out that no matter what the interface/grain boundary energy value was chosen compared to the surface energy value, the thermodynamic calculation could not solely reproduce the experimental results. Especially, the effect of annealing temperature on the m-phase fraction could not be understood based on the thermodynamic model. Since the entropy of the metastable t-phase or o-phase is higher than that of the m-phase, the m-phase fraction is expected to be invariable or even decrease with increasing temperature. From experiment, however, the m-phase fraction increased as the temperature increased, which implies that the tetragonal-to-monoclinic (t-to-m) phase transition is a thermally activated process. Moreover, they also concluded the presence of a higher activation energy barrier of the t-to-m phase transition than that of the tetragonal to- orthorhombic (t-to-o) phase transition by quantifying the activation energy barrier of each case. However, they did not consider the annealing time dependency of the phase transformation, which could render different value of the activation energy barrier.

Even though many reports have recognized the experimental effects on the evolution of the FE o-phase, only few researches have extensively examined the TE capping effect and its ramification upon the phase transformation rate change induced by its kinetic energy barrier. Capping effect refers to how the presence of the TE affects the phase formation in the oxide layer during annealing, and it is known to deter the formation of a non-FE m-phase of doped- HfO_2.[9] Toriumi et al. showed

that the Si capping layer on HfO$_2$ thin film provided a higher kinetic energy barrier for the phase transformation between the cubic phase (c-phase, space group: *Fm*3*m*) and the m-phase than the one without it.[15] They proved that such Si capping layer stalled the phase transformation from the t-/c-phase to the m-phase, but the formation of the FE o-phase was not dealt with in that paper.

Many reports experimentally proved that doped-HfO$_2$ thin oxide films with the capping show more enhanced FE properties than the one without the capping layer, yet an extensive investigation on such phenomena was not conducted. Refractory metal capping, such as TiN, is well known to hinder the surface migration of atoms on the film surface.[16] As a result, the TiN capping layer would potentially limit the grain growth as annealing proceeds, which is closely related to determining the surface energy value and a resultant stable phase formation. Nonetheless, a few reports experimentally showed that the grain size might not be the largest contributing factor to determine the final phase formation, [14,17] implying that there could be other potential factors, such as stress effect. Combined effects of the electrode intermixing, such as Ti or N diffusion into the oxide layer from the TiN electrode, the lattice mismatch between the oxide layer and the electrode, and the thermal coefficient difference of the dielectric layer and the substrate upon annealing could engender mechanical confinement on the dielectric layer and influence the final phase formation. [2,11,18–23]

This work aims to demonstrate the capping layer effect by the TiN electrode on the HZO thin film, based on the phase transformation rate and the kinetic energy point of view, and underscores its importance when considering the origin of the FE o-phase in the HZO film. Classical Johnson–Mehl–Avrami (JMA) model was implemented to describe the nucleation and growth behavior of the HZO thin film. It was found that the TiN electrode capping on the HZO thin films provided a higher activation energy barrier of 2–3 eV f.u.−1, where f.u. stands for formula unit, upon phase transition from the high temperature induced t-phase to the m-phase than to the o-phase. Classical JMA model, however, could not precisely describe the nucleation and growth behavior of the HZO thin film. Therefore, an alternative model of nucleation-limited transformation (NLT) was suggested, of which the origin resides on the nucleation-limited switching (NLS) model, a model to describe the kinetics of polarization switching within polycrystalline FE thin films. Quantitative analysis based on the phase transition kinetics can yield useful information about the nucleation and growth rate dependence on the electrode, an essential parameter for materials design.

3.2. Experimental

Approximately 10 nm HZO thin films were deposited on a TiN(50 nm)/Ti(5 nm)/SiO$_2$(100 nm)/Si substrate using an ALD technique at a wafer temperature of 280 °C. Hf[N(C$_2$H$_5$)CH$_3$]$_4$, Zr[N(C$_2$H$_5$)CH$_3$]$_4$, and ozone were used for Hf precursor, Zr precursor, and an oxygen source, respectively. Zr/(Hf+Zr) ratios were controlled by the ALD cycle ratio of Hf and Zr sources and kept at 1:1 ratio, with an equivalent growth rate of HfO$_2$ (1.2 Å per cycle) and ZrO$_2$ (1.2 Å per cycle). Approximately 50 nm thick TiN BE and ~5 nm thick TiN TE were deposited using magnetron sputtering. To achieve a reasonable amount of the t- and the o- phase within the film, in the first place, all samples were annealed using rapid thermal annealing at 600 °C for 20 s at N$_2$ ambiance with the TiN TE in place. These samples are referred to as a "pristine sample" in this work. Then, in order to differentiate PMA samples (annealed with the top TiN electrode placed) from PDA samples (annealed without the top TiN electrode), PDA samples are prepared by removing the top TiN electrode by dipping the pristine samples into the SC1 solution (H$_2$O:H$_2$O$_2$:NH$_4$OH = 50:2:1) at 50 °C for 6 min. The etch rate of TiN by the SC1 solution was ≈1.6 ± 1.0 nm min−1, so 6 min were sufficient to etch out the upper 5 nm thick TiN electrode. Subsequent annealing was followed for both PMA and PDA samples at 400, 500, 600, and 700 °C, using RTA. RTA was utilized for 10^0, 10^1, and 10^2 s samples, whereas a furnace was utilized for

10^3 and 10^4 s samples. The surfaces for the PDA samples were examined by a SEM (SU70, Hitachi) analysis. Because the SC1 solution could not etch away the (partially) oxidized TiN top electrode during subsequent annealing, etching with diluted HF solution was attempted, but the additionally annealed TiN electrode still could not be removed, possibly due to the significant oxidation or intermixing with the HZO film. Therefore, SEM analysis could not be applied to the PMA cases. The grain size analysis was conducted using a watershed method implemented by Gwyddion software.[48] The composition and the film thickness were examined using X-ray fluorescence (Quant'X, Thermo SCIENTIFIC) and the depth profiling was conducted by AES (PHI-700, ULVAC-PHI) analysis. The crystalline structure was analyzed using the GIXRD (incidence angle = 0.5°) mode of the X-ray diffractometer (X'pert pro, PANalytical) equipped with a Cu Kα X-ray source. The P–V and small signal alternating current (10 kHz) ε–V curves were measured by a ferroelectric tester (TF Analyzer 2000, Aixacct Systems) and an impedance analyzer (HP 4194, Hewlett Packard), where the bias was applied to the TE (with an area 8×10^4 μm^2, defined by a metal shadow mask) while the common BE was grounded.

3.3. Results and Discussions

First, the typical grazing incidence X-ray diffraction (GIXRD) and electrical data of a pristine HZO thin film, annealed at 600 °C for 20 s at N_2 ambiance with the TiN top electrode in place, are presented in Fig. 1. Distinct GIXRD peak at ~30.5° in Fig. 1a and deconvolution of the cumulative peak into 011t/111o and 111m peaks in Fig. 1b clearly indicate that a large amount of the 011t/111o peaks at ~30.5° was created within the film with small amount (4 ± 1%) of the 111m at ~31.6°. Hysteresis curve of polarization–voltage (P–V) and butterfly-shaped dielectric constant–voltage (ε–V) graphs of the pristine sample in Fig. 1c verify the FE switching behavior, indicating that FE o-phase has been formed in the HZO thin film. Electrical data were obtained after the wake-up process of 10^5 field cycling with double rectangular pulses with a height of 3 V at a frequency of 10^5 Hz. The values of $2P_r$ and peak dielectric constant near the coercive voltage were ≈35 μC cm−2 and ~37, respectively, revealing that the quality of the film appropriately fits the criteria of this work to observe the phase transition from the ferroelectric phase to non-FE phase.

Next, postmetallization annealing (PMA) and postdeposition annealing (PDA) samples were prepared as described in the Chapter 3.2 to analyze the influences of PMA and PDA processes on the phase transition in HZO thin film. The initially annealed HZO thin films with (PMA) or without (PDA) of the top electrode were additionally annealed at 400, 500, and 600 °C for 10^0, 10^1, 10^2, 10^3, and 10^4 s of which

GIXRD patterns are illustrated in Fig. 2a-f. Annealing temperatures of 400, 500, and 600 °C were selected because HZO thin film is usually heat treated under such temperature range.[5–8] Annealing below 10^2 s was performed using rapid thermal annealing (RTA), whereas annealing above 10^2 s could not be completed using RTA due to the possible high load on the RTA machine and, therefore, the furnace was selected instead. Temperature rising and cooling rate are much faster for the RTA (15 °C s−1 for rising and 7.5 °C s−1 for falling) than that of the furnace annealing (0.2 °C s−1 for rising and 0.1 °C s−1 for falling). However, considering the long annealing time above 10^2 s, such difference could hardly produce a significant disparity in the phase outcome and, therefore, was neglected. Each annealing condition rendered the collective combination of different phases, and the peak intensity of the t-/o-phase decreased as annealing time increased with increase in the m-phase peak intensity, representing the transitional phase transformation from the t-/o-phase to the m-phase. Clear difference in GIXRD patterns of the PMA and PDA samples annealed at the same temperature indicates that the presence of the top electrode produced different phase outcome. Although epitaxial growth is hardly applicable to polycrystalline thin film, the local epitaxial growth along the plane direction of the TiN electrode should not be neglected as a potential factor to influence the phase outcome. In fact, few works have reported a possible epitaxial growth of ZrO^2 or HZO thin film on TiN electrode under limited conditions.[24,25] However, local epitaxial growth was generally not observed in the past works,[26,27] unless the film

32

deposition condition is carefully controlled, because the lattice constant difference is as large as ~15% between the HZO thin film and the TiN electrode (t-HZO lattice constant: $a = b = 5.04$ A, $c = 5.13$ A, c-TiN lattice constant: $a = 4.28$ A).[1] Also, Kim et al. have presented that the FE behavior and the orientation of the HZO thin film, grown on amorphous Al_2O_3 and TiN, were almost the same.[27] Therefore, local epitaxial growth of HZO thin film along the plane direction of the TiN electrode and corresponding phase outcome can be neglected in this work.

In order to compare (semi-)quantitative fraction of each phase created for different samples, the GIXRD peaks near ~28.5°, 30.5°, and 31.6° were de-convoluted for the t-/o-phase and the m-phase, a similar procedure conducted in Fig. 1b. Although the peak area integration near such degree range cannot precisely represent the relative fraction of the t-/o-phase in the whole film, peak intensity is strong enough to easily compare and analyze the phase fraction relativity. Such method of deducing the relative amount of the phase created in the film has been widely accepted, [5] and a similar approach was conducted in this study as well. Peak positions of the −111m at 28.5°, 111o/011t at ≈30.5°, and 111m at 31.6° are indicated in the figure as dotted lines. Here, hklx stands for hkl plane of the x-phase, where x can be t (tetragonal), o (orthorhombic), or m (monoclinic). Additional peak was present near 27.5° in Fig. 2c,f, which could be ascribed to a rutile (110) TiO_2 peak, and further analysis on its formation is to be followed for the subsequent 700 °C annealing experiment discussed later.

After peak deconvolution, m-phase percentage was calculated using $(I_{111m} + I_{-111m})/$ $(I_{111m} + I_{-111m} + I_{011t/111o})$ to obtain the relative fraction of the transformed m-phase from the t-/o-phase with respect to the annealing time and temperature. Here, I_{hklx} stands for the areal intensity of the hkl diffraction peak from the x-phase. The quantified fraction of the transformed m-phase can be substituted into the JMA model to comprehend the mechanism of the phase transformation kinetics. The JMA stochastic model predicts the phase transformation fraction as a function of time with a general form of Equation (1) for isothermal phase transformation, where r_m is the ratio of the transformed m-phase, k the rate constant, n the Avrami exponent or the dimensionality factor.

$$r_m = 1 - e^{-(kt)^n} \qquad (1)$$

Amount of the m-phase in the pristine sample (after the first crystallization annealing at 600 °C for 20 s) obtained from Figure 1b was comparable in every sample, which was calculated to be $\approx 0.05 \pm 0.01$. Then, r_m under each annealing condition was calculated using peak deconvolution. Assuming that the nucleation and growth behavior in HZO thin film follows the JMA model, the natural logarithm of the transformed m-phase ratio versus annealing time is plotted in Fig. 3. The slope of the best-fitted line indicates the dimensionality of the nucleation and growth behavior, which came out to be 0.17–0.37 and 0.20–0.44 for PMA and PDA samples for all

34

temperature ranges. Rest of the constant values are summarized in Table 3-1. The slope value increment as annealing temperature increases indicates a faster transformation rate into the m-phase as the RTA temperature increases, which is a reasonable outcome considering that the t-to-m phase transformation is a thermally activated process. However, the obtained dimensionality factors are quite low compared to the normal n value (between 1 and 3) reported, [28–30] although it is comparable to the value of ~0.3, obtained by Toriumi et al.[15] They, however, did not conduct further analysis on such low dimensionality, even though the dimensionality of the nucleation and growth to be less than 1 is difficult to comprehend. In JMA model, slope n can be further expressed as $n = a + b \times c$, where a represents time-dependent nucleation rate, b, the dimensionality of the growing particles, and c, the growth mode with 0.5 to be volume-diffusion controlled and 1 to be interface-migration controlled. [28,29] When the value is equivalent to 1, it refers to a constant nucleation and growth time. When the value is smaller (or larger) than 1, it indicates that the nucleation rate is decreasing (or increasing) as annealing time increases. Rate decreasing behavior can be interpreted as such that the presence of the TiN electrode impeded the growth of nuclei within HZO thin film. Considering that non-uniform nucleation can lead to a reduction of the crystallization rate, [31] TiN TE seems to encourage the inhomogeneous nucleation behavior. It was, therefore, necessary to take nucleation inhomogeneity into account to more precisely explicate the nucleation behavior in HZO thin film by utilizing different model from JMA.

The growth of polarization domain during ferroelectric switching occurs in a similar geometry to the nucleation and growth, and thus, the same equation can be utilized to explain the nucleation and growth behavior of the m-phase in the HZO film. In fact, a number of reports on ferroelectric domain switching have employed the nucleation model to explain the FE switching kinetics.[32–34] JMA model of nucleation and growth is similar to the Kolmogorov–Avrami–Ishibashi (KAI) model in FE switching field, where KAI model describes the polarization switching kinetics in terms of the unrestricted growth of domain in response to the applied electric field.[35,36] KAI model has generally been applied to the uniform switching behavior of ferroelectric single crystals or epitaxial thin film.[33,34] However, it has been reported that such model cannot be applied to polycrystalline films due to the broad distribution of switching time.[33] As mentioned, the JMA model is based on the assumption of homogenous nucleation and unimpeded growth, which is unlikely to happen in polycrystalline HZO thin films. When the new phase is nucleated by the embryos which already exist in the mother phase, kinetics of the phase change can be demonstrated by a combination of factors such as density, growth, and transformed volume of embryos in regard to a characteristic time scale.[32] NLS model takes into account such condition by integrating the Lorentzian distribution of logarithmic switching time during the domain growth.[33] Hence, such analysis can be applied to the results obtained in this study by integrating the Lorentzian distribution time of nucleation to JMA model, with a general form of Equations (2) and (3), and it will be

36

referred to as NLT in this study. In these equations, r_m is the ratio of the transformed m-phase, n the dimensionality factor, t_0 the characteristic nucleation time, A the normalization constant, and w the half-width at half-maximum of a central value, $t_{0,med}$.

In the oxide thin films, defects such as vacancies are present even at well-prepared single-crystal surfaces, and a number of defects in a polycrystalline thin film potentially are very likely to drive the nucleation and growth more readily.[37] Because the film was previously annealed at 600 °C for 20 s using RTA, the film was mostly crystallized into a polycrystalline phase which was confirmed by the clear GIXRD peaks. Moreover, the presence of the TiN TE could also induce the distribution of the transformation rate of different regions under the electrode compared to the free surface. Therefore, adapting the NLT model would be an adequate approach to describe the nucleation and growth behavior of HZO thin film.

$$r_m = \int_{-\infty}^{\infty} \left(1 - e^{-(t/t_0)^n}\right) F(\log\ t_0)\, d(\log\ t_0) \tag{2}$$

$$F(\log\ t_0) = \frac{A}{\pi} \left[\frac{w}{(\log\ t_0 - \log\ t_{0,m\ ed})^2 + w^2}\right] \tag{3}$$

Fig. 4a, b shows the fitting of the NLT model onto the raw data of the transformed m-phase amount at each annealing temperature, obtained from the GIXRD deconvolution. Although it would be more conclusive to conduct the fitting using a

larger number of raw data points, the given number of data points was just enough to confirm the overall trend of the nucleation and growth behavior within the different temperature range of PMA and PDA. It can be seen that NLT fitting appropriately approximated the data points under different temperature. Data values were normalized to the value of 100, which implies that as annealing time approaches an infinite value, all phases will eventually fully transform to the m-phase. This assumption arose from the fact that portion of the m-phase increased in the HZO thin film even without grain growth as the temperature increased, indicating that once thermally activated, the m-phase formation is inevitable despite the surface energy contribution. It should be also noted that the most stable phase in HZO thin film in terms of the bulk free energy for all tested conditions would be the m-phase. In order to decrease the uncertainty that could come from various fitting parameters, n value was fixed as 1, which implies a constant nucleation rate since the cluster tends to grow steadily beyond the critical size. [38] Such assumption was also made for the HfO$_2$ thin film in several previous reports. [14,28]

From the NLT plot, the $t_{0,med}$ value can be deduced, which indicates the median value of t_0 with Lorentzian distribution. For nucleation and growth model, $t_{0,med}$ would indicate the time when the nucleation readily occurs. The value of the $t_{0,med}$ decreased from 4×10^7 to 10^4 s and from 4×10^5 to 5×10^2 s for PMA and PDA samples, respectively, as the RTA temperature increased from 400 to 600 °C. $t_{0,med}$ values of PMA samples were proven to be higher than that of PDA samples by approximately

38

two orders of magnitudes, which implies that the capping layer increased the nucleation barrier within HZO thin film and lowered its rate, which is a similar result deduced from the activation energy of linear JMA fitting. This again explains why n came out to be smaller than 1 in a previous JMA model fitting because the presence of the electrode suppressed the nucleation just as the different $t_{0,med}$ values indicated. Although the $t_{0,med}$ value of the PMA samples could have come out to be lower than that of the PDA samples due to a large number of defects created between the electrode and the oxide layer, giving more probabilities for the nuclei creation, a large activation energy barrier formation by the capping effect seems to be more effectively involved than the defect effects. Fig. 4c, d shows a distribution function with respect to log t_0. Lorentzian distribution parameters of w for PMA and PDA samples are embedded within the figures. Compared to the PMA samples, $t_{0,med}$, which is the t_0 value at the highest distribution function peak in the figure, of the PDA samples was formed at a smaller $t_{0,med}$ value with a narrower width (smaller w value) of the distribution peak. These results imply that the TiN capping layer not only delays the nucleation of the m-phase within the HZO film but also disperses its nucleation time resulting in a more inhomogeneous nucleation and growth behavior.

To obtain the activation energy value of the transformation rate of each PMA and PDA type, Arrhenius plot of $t_{0,med}$ was constructed as shown in Fig. 4e. Activation energy calculation was built on the assumption that the phase transition occurred via thermal activation. The slope was obtained from the best -linear-fitting, which was

converted to activation energy values of ~2.14 and 1.67 eV f.u.−1, for PMA and PDA, respectively, by multiplying the Boltzmann's constant. Higher activation value of the transformation rate into the m-phase for PMA samples clearly demonstrates that the TiN capping layer posed a higher activation energy barrier upon t-to-m phase transformation. As a result, higher amount of the t-/o-phase remained which resulted in the enhanced ferroelectric properties produced in several reports.[5–8,10–12,39–42]

Compared to the reported activation energy value of 1.2 eV f.u.−1 for the c-phase to the m-phase of Si capped HfO_2 thin film[15] or ~0.3 eV f.u.−1 for the t-phase to the m-phase of TiN capped HZO thin film,[14] the activation energy obtained in this study was quite high. 1.2 eV f.u.−1 of the work of Toriumi et al. was higher than that of the work of Park et al. because the former activation energy value was obtained under the assumption that n was ~0.3, whereas, the latter ~0.3 eV f.u.−1 was obtained under the assumption that n was 1. The reason why the value obtained in this study was higher than ~0.3 eV f.u.−1, even though n was considered to be 1, can be understood by the pre-crystallization process conducted in this study. It is known that pre-developed state like that of the nano-crystalline phase can influence the growth of the subsequent phase after annealing. [17] Already in a polycrystalline form with the t-phase being dominant after the first RTA at 600 °C for 20 s, pristine HZO sample would only obtain the m-phase from the adequate distortion and phase transformation from the already present t-phase. However, when the film was in an amorphous state, once the activation energy was overcome by the heating, crystallization with lower

energy would be stabilized, and the m-phase would more readily form. Also, defect concentration in the oxide layer or the interface layer could be different, leading to a different kinetic energy barrier value, considering that oxygen vacancy diffusion has a higher activation energy barrier of 1–3 eV. [43,44] To sum up, both the JMA and NLT models effectively showed that the capping layer generated a higher kinetic energy barrier and hampered the nucleation of the m-phase within HZO thin film.

To aid in understanding, schematics in Fig. 5 show the comparison between the JMA and the NLT based nucleation and growth behavior. For pristine samples after the RTA process, the initially dominant crystalline phase would be the t-phase as shown in the figure. The phase transition from the o-phase to the t-phase with increasing temperature has been confirmed in previous studies. [26,45–47] The polycrystalline film was assumed in the NLT model schematic, filled with different size and plane direction of the phase domain. JMA model assumes that nucleation and growth occurs homogeneously within the film, which may well apply to the (mostly) single crystalline mother phase. Although the pristine samples will be in a combination of t-phase, o-phase, and m-phase, t-phase will be the dominant phase as the figure indicates. Therefore, for simplicity, it is assumed that only the t-phase is present in the pristine state. Once the embryo reaches the critical radius as annealing time increases, it starts growing homogenously at a similar rate, indicated as a shaded circle in the JMA growth schematic. On the other hand, the NLT model presumes that the film consists of several areas that possess independent nucleation time. Once the

nuclei of the m-phase are formed within the t-phase domain, it will grow at a relatively higher rate than the nucleation rate. In other words, the growth time is not a dominant factor in determining the phase transformation rate, but the nucleation time. As time continues, the transformed area will depend on the rate of the m-phase nuclei formation within the t-phase domain, which will be influenced by the TiN TE in this study.

Next, grain size was analyzed using SEM to figure out if any other factor like the grain size could have affected the m-phase formation retardation. Due to the difficulty of removing (partially) oxidized TiN TE for the cases of PMA samples, SEM analysis for only PDA samples was conducted. Fig. 6 shows the distribution of the grain size of the PDA samples of different annealing time and temperature using a watershed method implemented by Gwyddion program. [48] Gwyddion program compares the contrast image of the grain and grain boundary to find out a local minimum of the contrast and calculate the grain size distribution within the selected SEM image. Many reports have used such method to compare the grain size distribution effectively, and detailed procedures can be found elsewhere. [14,49,50] Because the distribution of the grain size was sporadically plotted (raw data plotted within the figure as transparent dots), it was difficult to compare the distribution of each annealing condition. Hence, the Gaussian fitting of the dispersed data was employed as drawn with a solid line. Although a slight difference in grain size could be observed for different annealing temperatures, the difference was insignificant. This finding

implies that the different annealing time and temperature in this experiment had little influence on the grain size, and, thus, the observed difference in the m-phase fraction can hardly have a relationship with the grain size.

Auger electron spectroscopy (AES) analysis on the PMA and PDA samples were conducted with representative annealing time of 10^3 and 10^4 s at 600 °C as illustrated in Fig. 7. Compared to Fig. 7a, showing the atomic concentration profile of the pristine sample, Fig. 7b, c proves that TiN TE was still present for PMA samples, whereas Fig. 7d, e proves that TiN TE was completely removed for PDA samples. Fig. 7b–e show that high concentration of oxygen diffused into the electrode layer in tandem with the electrode elements diffusing into the oxide layer, as depicted with a broader width of Ti and N concentration. A number of results were reported that Ti and N diffusion could lower the t-phase free energy and promote its formation over the m-phase. [18–20] A number of reports have commented that the electrode materials can readily diffuse into the oxide layer and intermix together with the oxide layer. [51–53] This could be a possible reason for the no etching of the TiN TE after the PMA by both SC1 ($H_2O:H_2O_2:NH_4OH = 50:2:1$) and diluted hydrofluoric acid (HF) solutions.

To further support the NLT model, higher thermal budgets of 700 °C for 10^2, 10^3, and 10^4 s were applied for PMA and PDA samples. In this case, only furnace annealing was utilized. The furnace annealing for 10^1 s was not conducted because controlling annealing time of 10^1 s was not viable—it would not make much difference from 10^2 s sample. When the GIXRD analysis was conducted as shown in

Fig. 8a-c, not a dramatic change of the m-phase at either 28.5° or 31.6° was observed as time increased, which implies that a transformation into the m-phase was significantly deterred even though the annealing temperature was the highest. It must be reminded that the m-phase fraction was already quite high even at the shortened time of 10^2 s (see Fig. 9 for more quantitative analysis).

Interestingly, at an annealing temperature of 700 °C, putative rutile (110) TiO_2 phase XRD peak was observed at 27.5°, which was only present in the 10^3 and 10^4 s annealing at 600 °C. Considering that more intermixing of the electrode can occur at 700 °C, rutile TiO_2 seems to hamper the further m-phase formation. As annealing temperature increased from 600 to 700 °C, the rutile TiO_2 formation became more active than the m-phase formation. Considering that grain size difference was negligible as annealing time increased at 700 °C as discussed in Fig. 6d, grain size effect can be ruled out. Fig. 9a–d summarizes the variations in the m-phase fraction and average grain size as a function of annealing time for the case of PDA samples, when the annealing was performed at 400, 500, 600, and 700 °C, respectively. These figures more clearly show that the relative fraction of the m-phase increased as annealing temperature and time increased, while the grain size almost stayed constant. Such results coincide with the results obtained by Park et al. that different annealing temperature did not produce any difference in the grain size. [17] Grain size is closely related to the surface and interface/grain boundary energy, and it has a large contribution to the phase formation in HZO thin films. When as-deposited, nano-

44

crystalline nuclei are more prone to the t-/o-phase formation at room temperature due to the surface and interface/grain boundary energy involvement. However, as nuclei fully grow and form grains during the annealing process, the surface and interface/grain boundary energy contribution alone cannot sufficiently stabilize the t-/o-phase over the m-phase at room temperature. They can only decrease the difference in relative Gibbs free energy between the t-/o-phase and the m-phase, when compared to the bulk free energy difference. Nonetheless, the t-/o-phase and the m-phase can coexist at room temperature due to other predominant effects, such as the kinetic energy barrier in this case. When the metastable nuclei form the high-temperature t-/o-phase at the annealing temperature, they seem to retain the very t-phase and not a more stable m-phase when cooled down to room temperature, due to the presence of the kinetic energy barrier. As annealing temperature and time increase, the t-/o-phase starts obtaining enough thermal energy to overcome the kinetic energy barrier and transforms to the more stable m-phase. Once the m-phase is formed, it cannot change back to the metastable phases at room temperature. Similar interpretation based on the kinetics can be applied for thicker films as well. According to the nucleation theory, a larger driving force results in a smaller nuclei size and higher nucleation rate. [54] There will be a large driving force for the phase transition toward the m-phase during deposition of thick films because not only the m-phase is the more stable phase at the deposition temperature of 280 °C, but also the longer deposition is needed. Therefore, the nucleation of the m-phase might sufficiently occur due to the higher

nucleation rate and longer deposition time. Analysis on the nucleation kinetics of HZO films with different thickness is beyond the scope of the present work, and more qualitative experiments are to be followed.

It could be argued that relative fraction of the m-phase seems to have saturated to the maximum degree at a faster rate at 700 °C so that no further phase transformation would occur even the annealing time proceeds. However, when additional annealing was conducted at 600 °C for a longer time of 105 s, the relative fraction of the m-phase surpassed the amount of the m-phase created at 700 °C for 10^4 s (data not shown), which infers that there is a room for more m-phase transformation even at 700 °C. To comprehend such results, a literature survey was conducted. Seo et al. reported that the rutile TiO_2 phase could hinder the m-phase formation of HfO_2 and support the t-phase formation due to the small lattice mismatch between them (rutile-TiO_2 and t-phase HfO_2). It is believed that a similar phenomenon was observed in this experiment. [55] Retardation of the m-phase growth may not be solely attributed to the rutile TiO_2 formation, but the experimental results evidently show that the m-phase formation decreased once rutile TiO_2 phase had formed. Such results are also in accordance with the report that Ti and N stabilized the metastable t- and o-phases. [18–20] More interpretation on such behavior is to be conducted in depth in the future.

Fig. 10 shows the GIXRD peak shift of the t-/o-phase as annealing temperature and time change. t-/o-phase peak slightly shifted toward the lower degree range, as annealing time increased for all temperature range. As the annealing time increased,

the t-phase transformed to the o-phase possibly due to the 2D stress effect as reported elsewhere. [6,21] When the t-/o-peak positions were compared for PMA and PDA samples annealed at the same temperature, they were present at a higher 2θ degree for PMA than PDA. Higher 2θ degree value implies a smaller interplanar spacing of the HZO t-/o-phase, which again infers that stronger tensile stress was applied to the film when capping was present. A few reports have emphasized the importance of the in-plane tensile stress in controlling the ferroelectric properties of HZO thin film. [56,57] TiN TE layer induced a tensile stress effect on the HZO film, which was why PMA samples usually showed more enhanced FE behavior than PDA samples. In addition, as discussed in Fig. 7, Ti and N diffusion from the TE (combined with effects from the BE) deters the formation of the non-ferroelectric m-phase, since Ti decreases the t-phase free energy over the m-phase energy of HfO_2 when the relaxation patterns of metal–oxygen bond were considered from the first principles calculation.[18] Small doping of N also assists the HfO_2 ferroelectricity.[18] Therefore, a tensile stress effect and TE interfacial effect, combined with Ti or N diffusion into the HZO layer, helped to mitigate the rapid phase transition from the t-phase to the m-phase. This resulted in the more t-/o-phase formation, as experimentally supported by the higher activation energy barrier value, combined with a larger $t_{0,med}$ and w value from NLT model described in this work.
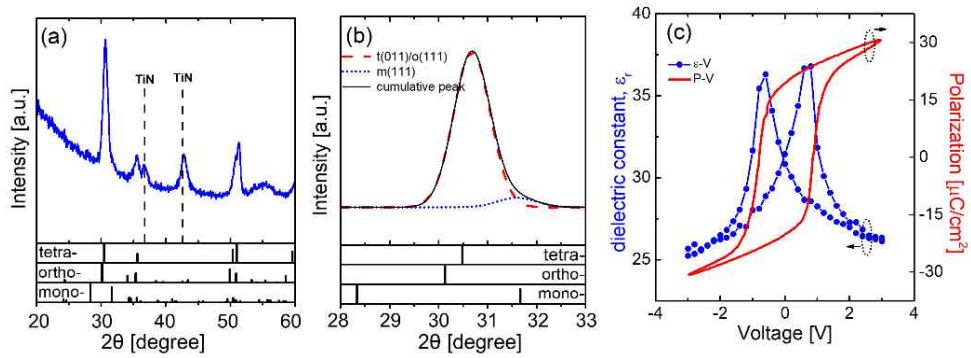
Figure 3.1. The grazing-angle incidence X-ray diffraction patterns of ~10 nm Hf$_{0.5}$Zr$_{0.5}$O$_2$ thin film a) after rapid thermal annealing at 600 °C for 20 s. b) Peak deconvolution with −111m, 011t/111o, and 111m at 28.5°, ~30.5°, and 31.6°, respectively. c) *P–V* and *ε–V* indicate the adequate polarization switching behavior. The reference powder patterns were obtained from the Inorganic Crystal Structure Database on HfO$_2$ with the reference codes 98-002-7313 (monoclinic P2$_1$/c), 98-017-3966 (tetragonal P4$_2$/nmc), and 03-065-5759 (cubic Fm3m TiN). The orthorhombic Pca2$_1$ reference peaks were calculated from the literature.
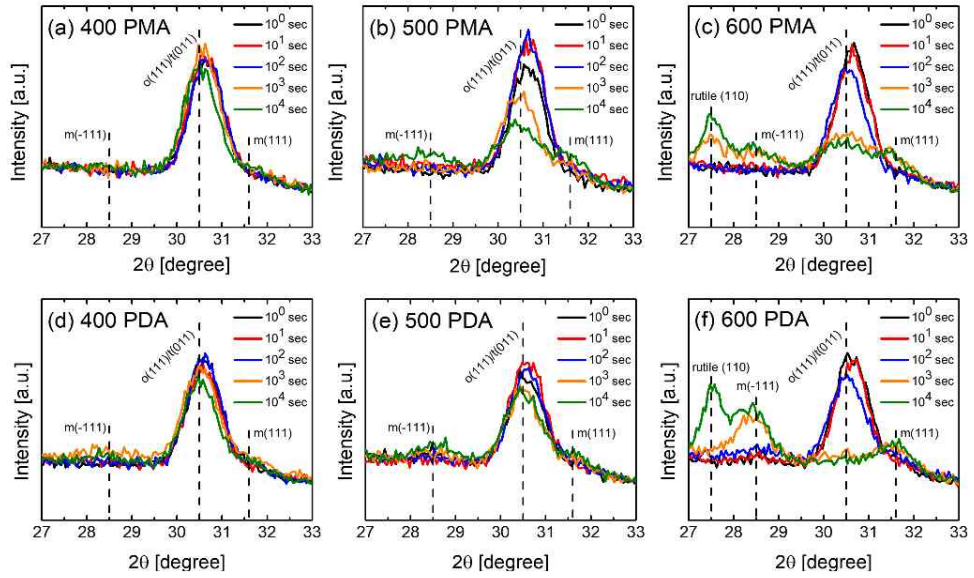
Figure 3.2. The grazing-angle incidence X-ray patterns of ≈10 nm $Hf_{0.5}Zr_{0.5}O_2$ thin film after subsequent rapid thermal annealing process at a,d) 400 °C, b,e) 500 °C, and c,f) 600 °C for postmetallization annealing/postdeposition annealing with annealing time variations of 10^0, 10^1, 10^2, 10^3, and 10^4 s. Representative phase peaks are indicated as dotted lines.
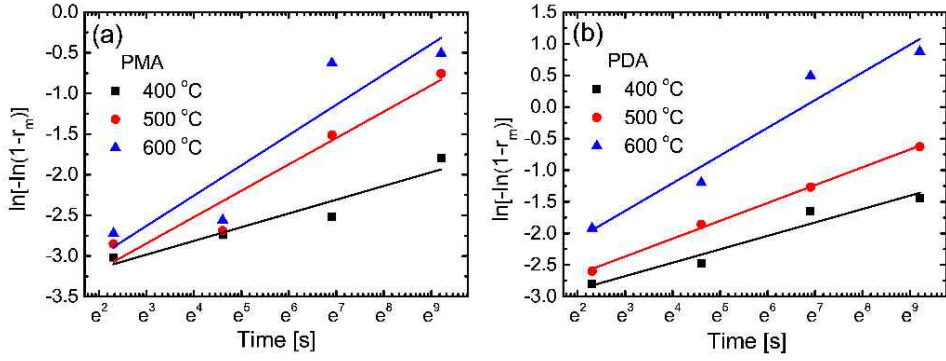
Figure 3.3. Best-linear-fitted lines of Johnson–Mehl–Avrami model of transformed monoclinic phase after a) postmetallization annealing and b) postdeposition annealing at 400, 500, and 600 °C under different natural logarithm time scale.

	PMA			PDA		
	Slope	y-intercept	k	Slope	y-intercept	k
400 °C	0.169	−3.49	1.06×10^{-9}	0.212	−3.31	1.65×10^{-7}
500 °C	0.324	−3.82	7.67×10^{-6}	0.282	−3.21	1.14×10^{-5}
600 °C	0.373	−3.75	4.28×10^{-5}	0.438	−2.96	1.16×10^{-3}

Table 3-1. Various constant values obatined from the best fitted line of Johnson–Mehl–Avrami of transformed monoclinic phase after postmetallization annealing and postdeposition annealing at 400, 500, and 600 °C.
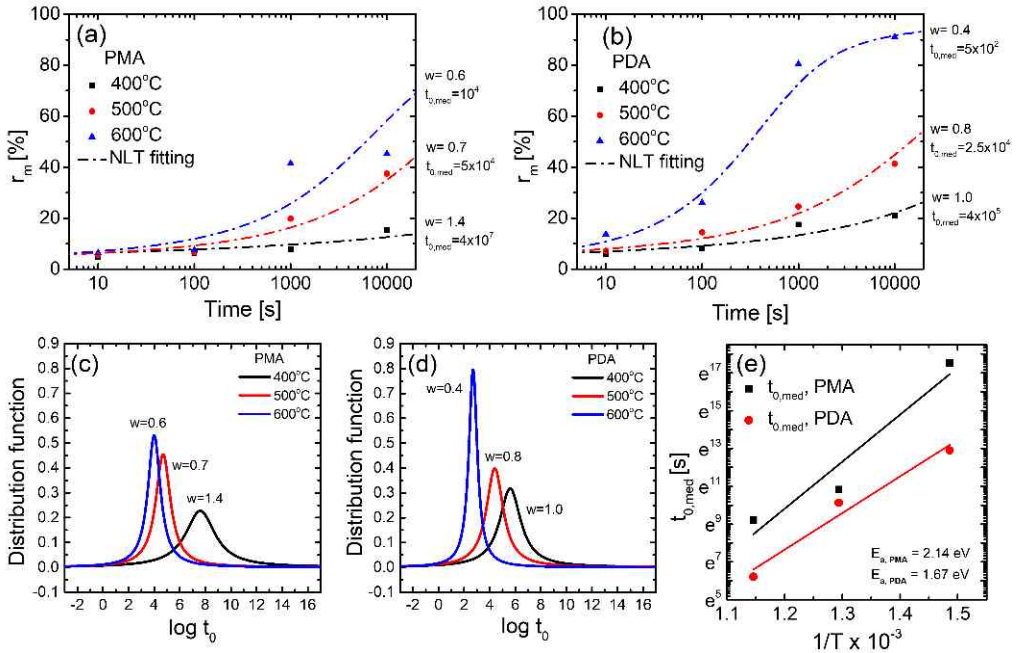
Figure 3.4. Nucleation-limited transformation model integrated fitting on transformed monoclinic phase with respect to annealing time at 400, 500, and 600 °C for a) postmetallization annealing and b) postdeposition annealing $Hf_{0.5}Zr_{0.5}O_2$ thin film. Distribution function versus logarithm t_0 is plotted for c) postmetallization annealing and d) postdeposition annealing samples with w values embedded within the figures, and e) Arrhenius plot of characteristic nucleation time, $t_{0,med}$, with the activation energies of 2.14 and 1.67 eV f.u.−1, respectively.

52
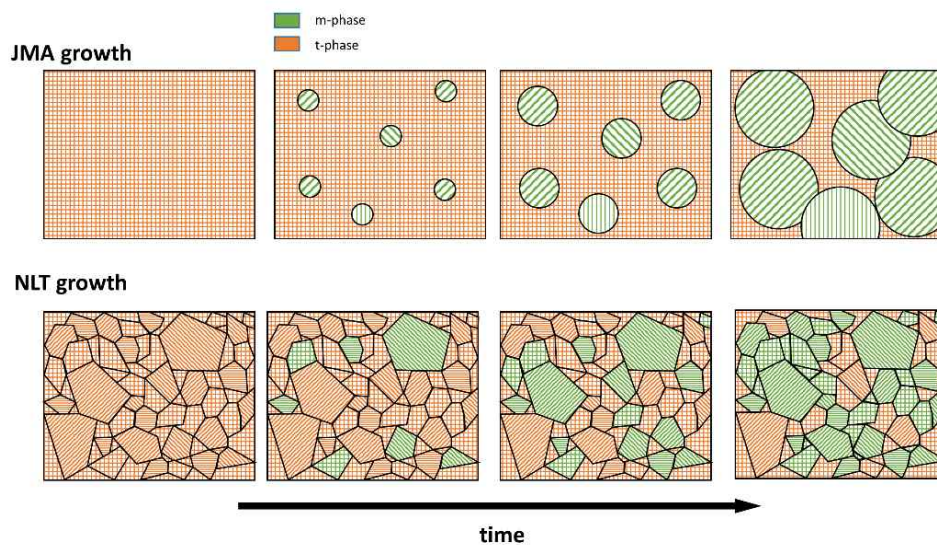
Figure 3.5. Schematic diagram showing the difference between nucleation and growth behavior of tetragonal phase to monoclinic phase transition based on Johnson–Mehl–Avrami model and nucleation-limited transformation with respect to annealing time. First figure on the far left for each model represents the pristine $Hf_{0.5}Zr_{0.5}O_2$ thin film.
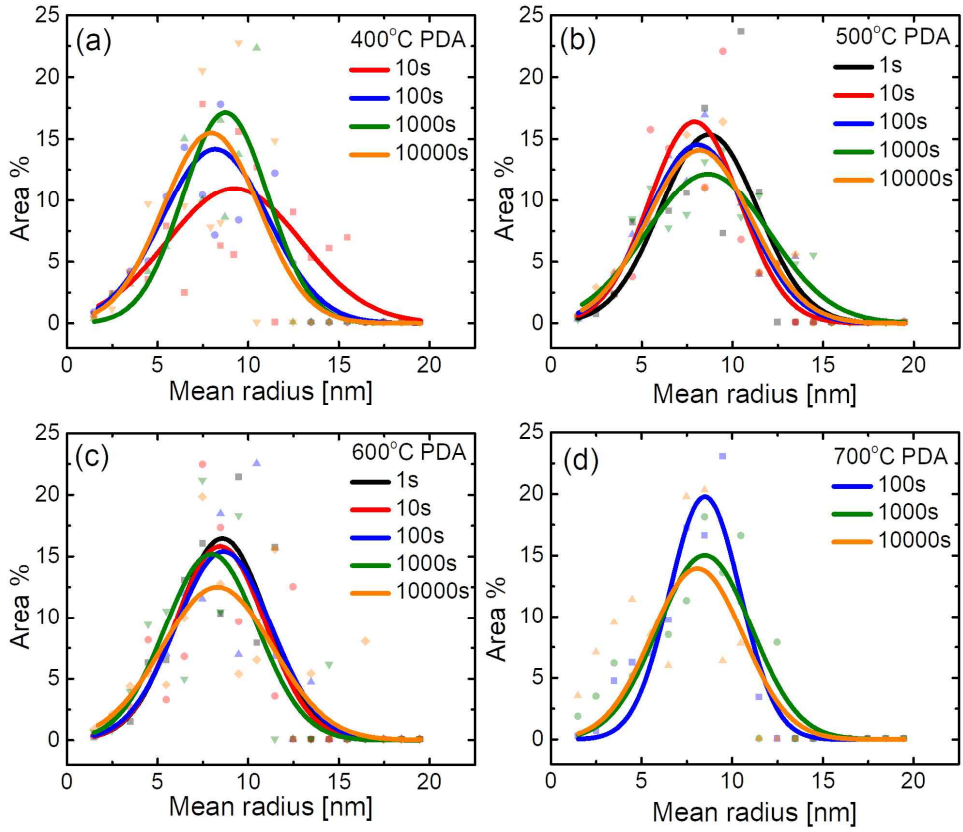
Figure 3.6. Grain size distribution of ≈10 nm $Hf_{0.5}Zr_{0.5}O_2$ thin film after postdeposition annealing at a) 400 °C, b) 500 °C, c) 600 °C, and d) 700 °C using watershed method implemented by Gwyddion software. Gaussian distributions for dispersed data are shown with solid lines.
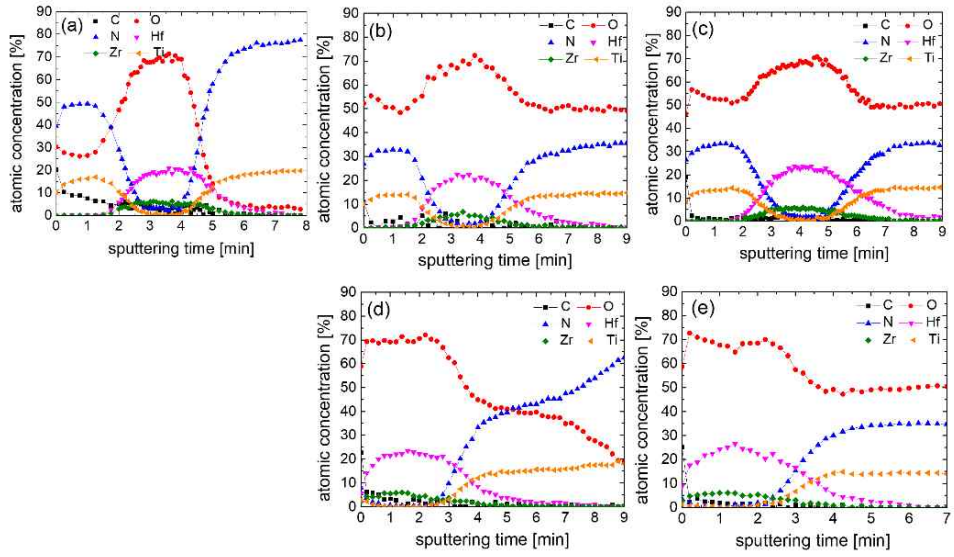
Figure 3.7. Auger electron spectroscopy depth profiles of the ≈10 nm $Hf_{0.5}Zr_{0.5}O_2$ thin film after a) rapid thermal annealing at 600 °C for 20 s. Subsequent postmetallization annealing for b) 10^3 and c) 10^4 s and postdeposition annealing for d) 10^3 and e) 10^4 s were conducted.
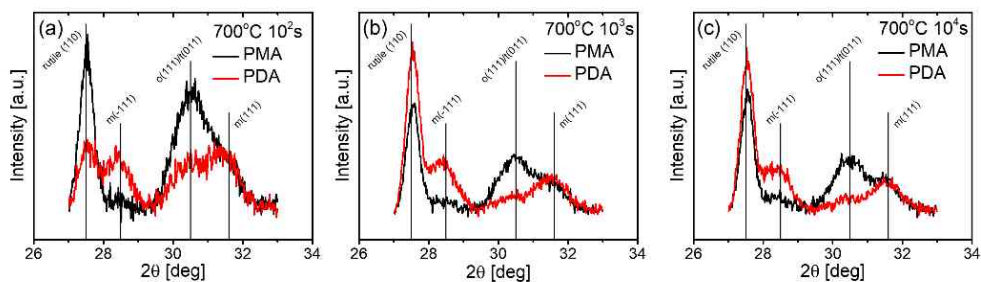
Figure 3.8. The grazing-angle incidence X-ray diffraction patterns of ~10 nm Hf$_{0.5}$Zr$_{0.5}$O$_2$ thin film after postmetallization and postdeposition rapid thermal annealing at 700 °C for a) 10^2, b) 10^3, and c) 10^4 s with rutile (110) TiO$_2$ phase at 27.5°. Representative phase peaks are indicated as solid lines.
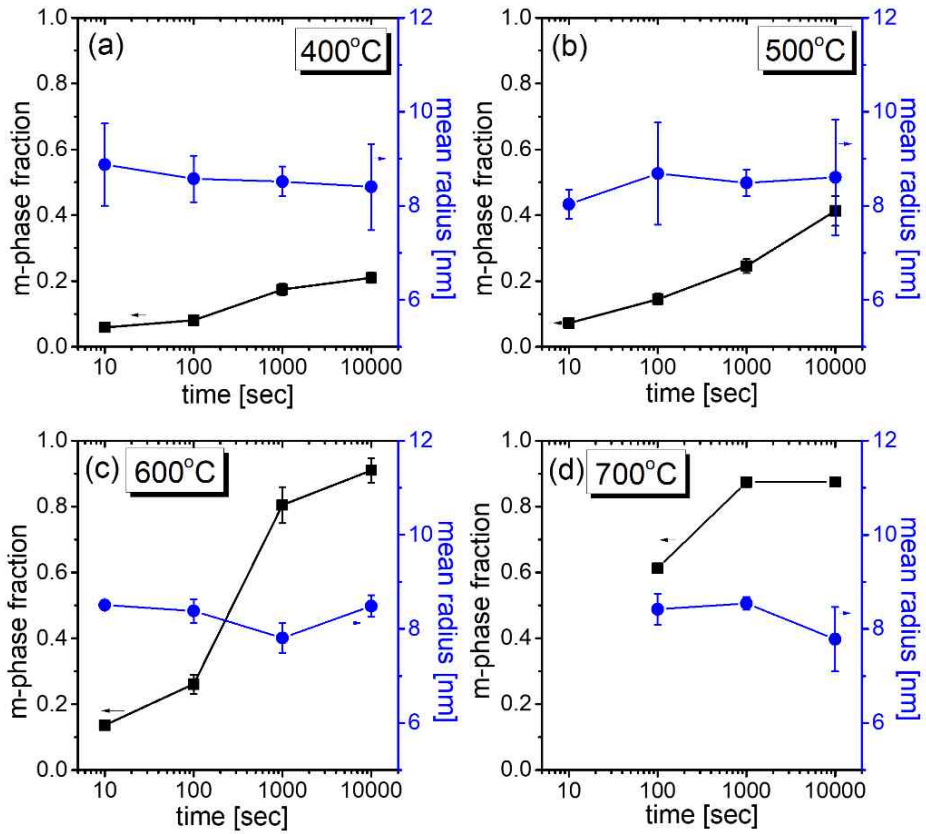
Figure 3.9. Monoclinic phase fraction (left axis) and mean radius of grains (right axis) of ≈ 10 nm $Hf_{0.5}Zr_{0.5}O_2$ thin film with respect to the rapid thermal annealing time at a) 400 °C, b) 500 °C, c) 600 °C, and d) 700 °C.
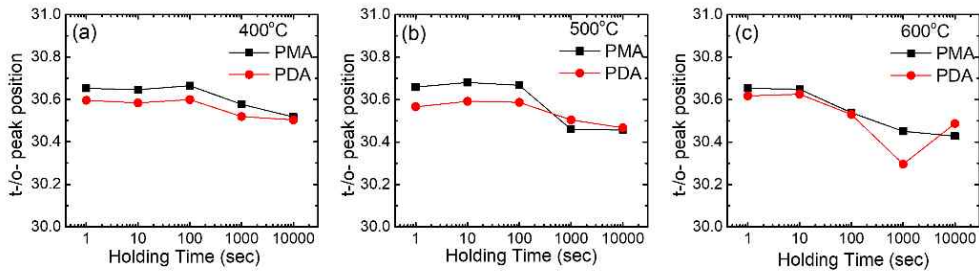
Figure 3. 10. Tetragonal/orthorhombic phase peak position at ~30.5° change of the grazing-angle incidence X-ray diffraction patterns of ~10 nm $Hf_{0.5}Zr_{0.5}O_2$ thin film with respect to the annealing time variance at a) 400 °C, b) 500 °C, and c) 600 °C for post-metallization and post-deposition annealing.

3.4. Conclusion

In conclusion, the variations in the relative fraction of the m-phase in ALD HZO film as a function of annealing time and temperature were studied mainly via the GIXRD and peak deconvolution. The HZO films were first crystallization annealed with the TiN top electrode at 600 °C for 20 s, and further annealing at different time and temperature was performed with or without the TiN capping layer. The JMA and NLT models were used to calculate the activation energy barrier of the m-phase formation. The dimensionality factor in JMA formulation, however, oddly came out to be less than 1, which conveyed a sense of nucleation retardation. Therefore, the NLT model was utilized to explain nucleation and growth behavior within HZO thin film further. It turned out that a capping layer hampered the nucleation and growth rate with higher and more distributed value of the characteristic nucleation time than non-capped films with $t_{0,med}$ activation energy barrier values of 2.14 and 1.67 eV f.u.−1 for PMA and PDA films, respectively. Almost constant grain size even after the prolonged annealing time proved that the grain size variation did not contribute much to the phase transformation kinetics. The rutile TiO_2 phase formed at an annealing temperature of 600 and 700 °C constrained further m-phase formation. Formation of the TiO_2 indirectly indicated that intermixing with the electrode and the oxide layer is inevitable. While the Ti and N diffusion potentially lowers the t-phase free energy over the non-FE m-phase, a TiN TE produced the tensile stress on the

oxide layer, encouraging the favorable condition to generate FE phase within the HZO thin film. Previous researches focused on the thermodynamic approach to explain the origin of ferroelectricity within doped HfO_2 thin films and embedded various factors into the density functional theory model to search for the most influential factor. However, this technique showed a wide gap between the calculated and experimental results. This study suggests that not only the contributing thermodynamics factors but also the kinetic effects, which could be further supplemented by the TiN capping layer effect, should be considered.

3.5. Bibliography

[1] R. Materlik, C. Kunneth, A. Kersch, *J. Appl. Phys.* **2015**, *117*, 134109.

[2] T. S. Boscke, J. Muller, D. Brauhaus, U. Schroder, U. Bottger, *Appl. Phys. Lett.* **2011**, *99*, 102903.

[3] C. Kunneth, R. Materlik, A. Kersch, *J. Appl. Phys.* **2017**, *121*, 205304.

[4] X. Sang, E. D. Grimley, T. Schenk, U. Schroeder, J. M. Lebeau, *Appl. Phys. Lett.* **2015**, *106*, 162905.

[5] M. H. Park, H. J. Kim, Y. J. Kim, W. Lee, T. Moon, C. S. Hwang, *Appl. Phys. Lett.* **2013**, *102*, 242905.

[6] M. H. Park, H. J. Kim, Y. J. Kim, T. Moon, C. S. Hwang, *Appl. Phys. Lett.* **2014**, *104*, 072901.

[7] M. H. Park, H. J. Kim, Y. J. Kim, W. Jeon, T. Moon, C. S. Hwang, *Phys. Status Solidi RRL* **2014**, *8*, 532.

[8] M. H. Park, H. J. Kim, Y. J. Ki, W. Lee, H. K. Kim, C. S. Hwang, *Appl. Phys. Lett.* **2013**, *102*, 112914.

[9] S. Mueller, J. Mueller, A. Singh, S. Riedel, J. Sundqvist, U. Schroeder, T. Mikolajick, *Adv. Funct. Mater.* **2012**, *22*, 2412.

[10] J. Muller, U. Schroder, T. S. Boscke, I. Muller, U. Bottger, L. Wilde, J. Sundqvist, M. Lemberger, P. Kucher, T. Mikolajick, L. Frey, *J. Appl. Phys.* **2011**, *110*, 114113.

[11] T. S. Boscke, St. Teichert, D. Brauhaus, J. Muller, U. Schroder, U. Bottger, T. Mikolajick, *Appl. Phys. Lett.* **2011**, *99*, 112904.

[12] E. Yurchuk, J. Muller, S. Knebel, J. Sundqvist, A. P. Graham, T. Melde, U. Schroder, T. Mikolajick, *Thin Solid Films* **2013**, *533*, 88.

[13] R. Batra, T. D. Huan, G. A. Rossetti Jr., R. Ramprasad, *Chem. Mater.* **2017**, *29*, 9102.

[14] M. H. Park, Y. H. Lee, H. J. Kim, Y. J. Kim, T. Moon, K. D. Kim, S. D. Hyun, T. Mikolajick, U. Schroeder, C. S. Hwang, *Nanoscale* **2018**, *10*, 716.

[15] A. Toriumi, Y. Nakajima, K. Kita, *ECS Trans.* **2011**, *41*, 125.

[16] M. H. Park, Y. H. Lee, H. J. Kim, Y. J. Kim, T. Moon, K. D. Kim, J. Muller, A. Kersch, U. Schroeder, T. Mikolajick, C. S. Hwang, *Adv. Mater.* **2015**, *27*, 1811.

[17] M. H. Park, Y. H. Lee, H. J. Kim, T. Schenk, W. Lee, K. D. Kim, F. P. G. Fengler, T. Mikolajick, U. Schroeder, C. S. Hwang, *Nanoscale* **2017**, *9*, 9973.

[18] C.-K. Lee, E. Cho, H.-S. Lee, C. S. Hwang, S. Han, *Phys. Rev. B* **2008**, *78*, 012102.

[19] D. Cunningham, *Honors Scholar Theses*, University of Connecticut, Storrs, Connecticut **2014**, p. 359.

[20] L. Xu, T. Nishimura, S. Shibayama, T. Yajima, S. Migita, A. Toriumi, *Appl. Phys. Express* **2016**, *9*, 091501.

[21] E. H. Kisi, *J. Am. Ceram. Soc.* **1998**, *81*, 741.

[22] T. J. Park, J. H. Kim, J. H. Jang, C.-K. Lee, K. D. Na, S. Y. Lee, H.-S. Jung, M. Kim, S. Han, C. S. Hwang, *Chem. Mater.* **2010**, *22*, 4175.

[23] W. Weinreich, L. Wilde, J. Muller, J. Sundqvist, E. Erben, J. Heitmann, M. Lemberger, A. J. Bauer, *J. Vac. Sci. Technol., A* **2013**, *31*, 01A119.

[24] Z. Fan, J. Deng, J. Wang, Z. Liu, P. Yang, J. Xiao, X. Yan, Z. Dong, J. Wang, J. Chen, *Appl. Phys. Lett.* **2016**, *108*, 012906.

[25] T. Li, N. Zhang, Z. Sun, C. Xie, M. Ye, S. Mazumdar, L. Shu, Y. Wang, D. Wang, L. Chen, S. Ke, H. Huang, *J. Mater. Chem. C* **2018**, *6*, 9224.

[26] M. H. Park, H. J. Kim, Y. J. Kim, T. Moon, K. D. Kim, C. S. Hwang, *Nano Energy* **2015**, *12*, 131.

[27] H. J. Kim, M. H. Park, Y. J. Kim, Y. H. Lee, W. Jeon, T. Gwon, T. Moon, K. D. Kim, C. S. Hwang, *Appl. Phys. Lett.* **2014**, *19*, 105.

[28] Y. Zhou, W. Lin, F. Yang, W. Fang, J. Huang, Q. Li, *Chem. Phys.* **2014**, *441*, 23.

[29] B. M. Hudak, S. W. Depner, G. R. Waetzig, A. Talapatra, R. Arroyave, S. Banerjee, B. S. Guiton, *Nat. Commun.* **2017**, *8*, 15316.

[30] Y. Ishibashi, Y. Takagi, *J. Phys. Soc. Jpn.* **2017**, *31*, 2.

[31] M. C. Weinberg, D. P. Birnie III, V. A. Shneidman, *J. Non-Cryst. Solids* **1997**, *219*, 89.

[32] M. Avrami, *J. Chem. Phys.* **1939**, *7*, 1103.

[33] J. Y. Jo, H. S. Han, J. G. Yoon, T. K. Song, S. H. Kim, T. W. Noh, *Phys. Rev. Lett.* **2007**, *99*, 267602.

[34] Y. W. So, D. J. Kim, T. W. Noh, *Appl. Phys. Lett.* **2005**, *86*, 092905.

[35] A. N. Shiryayev, *Selected Works of A. N. Kolmogorov*, Springer, Dordrecht, Netherlands **1992**, p. 188.

[36] M. Avrami, *J. Chem. Phys.* **1940**, *8*, 212.

[37] G. Haas, A. Menck, H. Brune, J. V. Barth, J. A. Venables, K. Kern, *Phys. Rev. B* **2000**, *61*, 11105.

[38] M. Avrami, *J. Chem. Phys.* **1941**, *9*, 177.

[39] U. Schroeder, E. Yurchuk, J. Muller, D. Martin, T. Schenk, P. Polakowski, C. Adelmann, M. I. Popovici, S. V. Kalinin, T. Mikolajick, *Jpn. J. Appl. Phys.* **2014**, *53*, 08LE02.

[40] D. Zhou, J. Muller, J. Xu, S. Knebel, D. Brauhaus, U. Schroder, *Appl. Phys. Lett.* **2012**, *100*, 082905.

[41] J. Muller, T. S. Boscke, D. Brauhaus, U. Schroder, U. Bottger, J. Sundqvist, P. Kucher, T. Mikolajick, L. Frey, *Appl. Phys. Lett.* **2011**, *99*, 112901.

[42] J. Muller, T. S. Boscke, U. Schroder, S. Mueller, D. Brauhaus, U. Bottger, L. Frey, T. Mikolajick, *Nano Lett..* **2012**, *12*, 4318.

[43] D. Martin, J. Muller, T. Schenk, T. M. Arruda, A. Kumar, E. Strelcov, E. Yurchuk, S. Muller, D. Pohl, U. Schroder, S. V. Kalinin, T. Mikolajick, *Adv. Mater.* **2014**, *26*, 8198.

[44] N. Capron, P. Broqvist, A. Pasquarello, *Appl. Phys. Lett.* **2007**, *91*, 192905.

[45] M. H. Park, H. J. Kim, Y. H. Lee, Y. J. Kim, T. Moon, K. D. Kim, S. D. Hyun, C. S. Hwang, *Nanoscale* **2016**, *8*, 13898.

[46] T. Shimizu, K. Katayama, T. Kiguchi, A. Akama, T. J. Konno, O. Sakata, H. Funakubo, *Sci. Rep.* **2016**, *6*, 32931.

[47] M. H. Park, C.-C. Chung, T. Schenk, C. Richter, M. Hoffmann, S. Wirth, J. L. Jones, T. Mikolajick, U. Schroeder, *Adv. Electron. Mater.* **2018**, *4*, 1700489.

[48] D. Necas, P. Klapetek, *Cent. Eur. J. Phys.* **2012**, *10*, 181.

[49] Y. H. Lee, H. J. Kim, T. Moon, K. D. Kim, S. D. Hyun, H. W. Park, Y. B. Lee, M. H. Park, C. S. Hwang, *Nanotechnology* **2017**, *28*, 305703.

[50] K. D. Kim, M. H. Park, H. J. Ki, Y. J. Kim, T. Moon, Y. H. Lee, S. D. Hyun, T. Gwon, C. S. Hwang, *J. Mater. Chem. C* **2016**, *4*, 6864.

[51] P. D. Lomenzo, Q. Takmeel, C. Zhou, C. M. Fancher, E. Lambers, N. G. Rudawski, J. L. Jones, S. Moghaddam, T. Nishida, *J. Appl. Phys.* **2015**, *117*, 134105.

[52] P. D. Lomenzo, P. Zhao, Q. Takmeel, S. Moghaddam, T. Nishida, M. Nelson, C. M. Fancher, E. D. Grimley, X. Sang, J. M. LeBeau, J. L. Jones, *J. Vac. Sci. Technol., B: Nanotechnol. Microelectron.: Mater., Process., Meas., Phenom.* **2014**, *32*, 03D123.

[53] G. Karbasian, R. dos Reis, A. K. Yadav, A. J. Tan, C. Hu, S. Salahuddin, *Appl. Phys. Lett.* **2017**, *111*, 022907.

[54] D. A. Porter, K. E. Easterling, M. Y. Sherif, *Phase Transformations in Metals and Alloys*, 2nd ed., CRC Press, USA **2009**.

[55] M. Seo, S. K. Kim, S. H. Han, C. S. Hwang, *Chem. Mater.* **2010**, *22*, 4419.

[56] T. Shiraishi, K. Katayama, T. Yokouchi, T. Shimizu, T. Oikawa, O. Sakata, H. Uchida, Y. Imai, T. Kiguchi, T. J. Konno, H. Funakubo, *Appl. Phys. Lett.* **2016**, *108*, 262904.

[57] T. Shimizu, T. Yokouchi, T. Shiraishi, T. Oikawa, P. S. Sankara Rama Krishnan, H. Funakubo, *Jpn. J. Appl. Phys.* **2014**, *53*, 09PA04.

4. Ru Bottom Electrode Effects on the Ferroelectricity of $Hf_{0.5}Zr_{0.5}O_2$ Thin Films

4.1. Introduction

Since the discovery of unprecedented ferroelectric (FE) orthorhombic phase (o-phase) in Si doped-HfO_2 thin film, origin of its ferroelectricity has been widely investigated.[1] Fluorite-structure doped HfO_2 possesses many advantages over conventional perovskite materials like $Pb(Zr,Ti)O_3$ (PZT) or $SrBi_2Ta_2O_9$ (SBT). Doped HfO_2 can be scaled down to few nm scale without losing its ferroelectricity, it is atomic layer deposition (ALD) friendly for three dimensional structure, and is Si compatible. [2] FE property which arises from the presence of non-centrosymmetric o-phase is realized under certain circumstances when external factors such as thickness[3], asymmetric stress[3], top electrode capping[1], annealing[4], and doping[5,6] come into play. Although these external effects are considered, it has not been possible to fully demonstrate the experimental results by implementing the first principle calculation. In fact, aside from the thermodynamic point of view, which is the main basis of the first principle calculation conducted in the past, the kinetics effect also seems to play a critical role to render FE o-phase.

Imperfect demonstration of experimental results using modeling still implies the lack of understanding of the FE origin of doped HfO_2 thin film, which brings electrode effect into attention since it seems to play critical role yet not much studies have been proposed. Although a number of studies of doped HfO_2 are based on TiN TE and BE, other type of electrode has been chosen as well. There were reports on different TE effect on Zr doped HfO_2 thin film. Pt TE showed degraded FE behavior due to symmetric strain applied to the film and RuO_2 showed a poor FE behavior due to Ru diffusion into the dielectric layer. [7,8] Park et al. showed that the effect of the Pt TE is less influential than the Pt BE effect, indicating that the BE effect could be more phenomenal than the TE effect. Park et al. presented the effect of (111) Pt BE on the FE o-phase formation and showed that since Zr doped HfO_2 undergoes symmetric strain which hinders the o-phase formation. [7] Hoffmann et al. showed that the $2P_r$ value can be as high as ~80 $\mu C/cm^2$ at 4 MV/cm for Gd doped HfO_2 thin film on TaN BE. Park et al. reported on the Zr doped HfO_2 on Ir with $2P_r$ of ~33 $\mu C/cm^2$ at 2.5 MV/cm and commented that oxygen supply from IrO_x resulted in the enhanced ALD behavior in initial steps that created formation of the smaller in-plane tensile strain and the larger grain size which was not very favorable for the o-phase formation.[3] Lin et al. showed that pure ZrO_2 film can show ferroelectricity on Pt BE with $2P_r$ of ~27 $\mu C/cm^2$, which is contradictory to the report by Park et al.. [9] Although a clear explanation behind why it showed such result was not presented, it showed that the choice of the BE is important.

There has not been a report on doped HfO_2 on Ru BE. Ru is a stable metal and still is conductive when oxidized to RuO_2 (resistivity ~35 $\mu\Omega{\cdot}cm$) which is a large advantage in terms of fabrication process. When TiN electrode is used, it is easily oxidized to TiON or TiO_2 which acts as a parallel capacitor and decreases the actual field across the FE layer which again increases the operating voltage. Also, conducting oxide is known to improve fatigue problem. Oxygen vacancies can be easily generated as TiN acts as an oxygen sink and takes away the oxygen from the FE layer. This could deteriorate the leakage problem. However, RuO_2 with higher formation energy (-201.190 kJ/mol) than TiO_2 (-833.972 kJ/mol) so doped HfO_2 will not easily give up the oxygen. [20] Seo et al. have reported that the formation of rutile TiO_2 can promote the formation of tetragonal phase (t-phase) while anatase TiO_2 promotes monoclinic phase (m-phase). [19] Also, Kim et al. have reported that O_3 oxidant during ALD process oxidizes Ru electrode and forms RuO_2 which promotes rutile TiO_2 formation. [18] Although lattice constant of rutile TiO_2 is slightly different from that of rutile RuO_2, if the lattice mismatch is quite matched, rutile RuO_2 can hinder m-phase and promote t-phase, which can transform to FE o-phase.

Lee et al. reported that when JMA fitting was conducted on the amount of the m-phase transformation of the Zr doped HfO_2 thin film during PMA and PDA at 700ºC, it produced much smaller slope compared to that of 600, 500, or 400 ºC although it should have shown higher slope due to higher thermal energy provided upon phase transformation. [12] However, due to rutile TiO_2 formation from the top and bottom

69

TiN electrode, phase transformation from the t-/o-phase to the m-phase was significantly reduced. Similar to the work by Seo et al., the structure of the rutile phase of TiO_2 seems to be quite similar to that of the t-phase of HfO_2, hindering the formation of the m-phase. [19] Therefore, rutile RuO_2 which has a similar crystal structure to rutile TiO_2 is expected to hinder the non-FE m-phase formation during growth. In this work, the influence Ru or RuO_2 BE on the FE property of Zr doped HfO_2 is investigated during ALD process.

4.2. Experimental

The polycrystalline (Hf,Zr)O$_2$ thin films were grown by a atomic layer deposition on Ru(30nm)/TiN(8nm)/SiO$_2$(100nm)/Si substrate. Hf[N(C$_2$H$_5$)CH$_3$]$_4$, Zr[N(C$_2$H$_5$)CH$_3$]$_4$, and O$_3$ (with a concentration of 180gm^{-3}) were used for Hf precursor, Zr precursor, and an oxygen source, respectively, as shown in Fig. 4.1. Pt(30nm)/RuO$_2$(30nm) top electrode with an area of 8 x 10^4 um^2 was fabricated by DC magnetron sputtering at 110°C substrate temperature. Annealed samples were post-metallization-annealed at 500°C for 30 sec in N$_2$ ambience. The The grain size analysis was conducted using a watershed method implemented by Gwyddion software.[10] The composition and the film thickness were examined using X-ray fluorescence (Quant'X, Thermo SCIENTIFIC) and the depth profiling was conducted by AES (PHI-700, ULVAC-PHI) analysis. The crystalline structure was analyzed using the GIXRD (incidence angle = 0.5°) mode of the X-ray diffractometer (X'pert pro, PANalytical) equipped with a Cu Kα X-ray source. The P-V loops of the Pt/RuO$_2$/(Hf,Zr)O$_2$/Ru/TiN/SiO$_2$/Si capacitors were tested using an axiACCT TF-2000 analyzer at a frequency of 1kHz in virtual ground mode. Capacitance – voltage (C-V) and current – voltage (I-V) characteristics were also checked using Hewlett Packard 4194 impedance analyzer and Hewlett Packard 4145B semiconductor parameter analyzer, respectively, to confirm the feasible dielectric performance of all the capacitors. All bias was applied to top Pt electrode while the BE was grounded.

4.3. Results and Discussions

Since not many studies of doped HfO_2 were conducted on Ru BE, it was necessary to confirm the self-saturation behavior during ALD process as shown in Fig. 4.2. Feeding and purge time of metal precursor and oxidant were varied for each TEMA-Hf and TEMA-Zr, and showed good self-saturation behavior. This indicates that the film is successfully grown during ALD process. When ALD process temperature was varied, as shown in Fig. 4.3, it showed that 300 °C is the critical temperature above which the chemical vapor deposition (CVD) process begins to occur. In order to maximize the local preferential growth of HZO on Ru electrode, the temperature between ALD and CVD were chosen. Linearly increasing thickness with respect to the ALD cycle numbers, it shows that the temperature range is in between ALD and CVD. About 2.1 Å/cycle and 1.7 Å/cycle growth per cycle (GPC) were obtained which is quite high compared to the GPC of ~1.2 Å/cycle for HZO on TiN BE. [3,7,8] Since the processing temperature is between the ALD and CVD process, the GPC came out to be quite high. Further explanation on the abnormal high growth of HZO thin film on Ru electrode will be discussed later in the chapter.

Grazing incidence X-ray diffraction (GIXRD) analysis was conducted at as-deposited state without post annealing process as shown in Fig. 4.4. Surprisingly, HZO thin film showed X-ray peak at ~30.5° indicating that the film has been crystallized as t-/o-phase on Ru bottom electrode. HZO film usually shows

amorphous state on TiN BE [3,7,8] but there seems to be enough thermal energy and small lattice mistmatch between the t-/o-phase and Ru electrode promoting the locally preferential growth behavior.

Fig. 4.4 shows the close-up of the peaks that were present in wide angle X-ray data. It is a challenging task to differentiate the phase difference between the t- and the o-phase through XRD response due to their structural similarity. According to the Vegard's law, the peak position of the t-phase and the o-phase is approximately estimated to be 30.8 and 30.4°, respectively. As process temperature increases, the peak intensity increases, indicating that the more the thermal energy provided, the more crystallinity the film obtains. Also Fig. 4.4 shows that as the process temperature increases, o(020/002) and t(200) peak intensity increase, indicating that Ru BE has a large impact on the structure formation of the HZO thin film. T. Schenk et al. reported that the factor to enhance the FE behavior of La doped HfO_2 is the high crystallinity of the o-phase formation along (020) and (002) direction. [11] HZO prepared in this work seems to possess similar phases, indicating the possible high P_r within the film.

When normal θ-2θ mode was conducted, only the peak at ~30.5° was shown indicating that (111) o-phase or (011) t-phase were grown normal to the surface of the film. Such locally preferential growth of HZO thin film was not seen when the film was grown on TiN BE. [3] Such growth on Ru BE could be the cause of high GPC on Ru. According to the report by Park et al., local preferential growth of (111) HZO on (111) Pt BE produced higher GPC than on TiN BE due to competition between the

surface energy and the interfacial energy. [7] Because (111) oriented HZO thin film had low surface and interface energy when grown locally epitaxially on (111) oriented Pt BE, it showed higher GPC than on TiN BE. Similar behavior is occurring on Ru BE indicating that the direction of the film growth and the BE are highly related during growth. Fig. 4.4 and Fig. 4.5 show that Ru is highly crystallized toward (002) direction. If the film is grown on crystallized BE, it will have lower surface energy compared to that of amorphous TiON or less crystallized TiN BE with lack of preferred orientation. Therefore, it will be easier for the film to grow homogenously and crystallize on crystallized BE, which is the case in this work.

As process temperature increases, not only the peak intensity increases but also the peak position shifts to the lower 2θ position, as shown in Fig. 4.5. This implies that either more o-phase is formed as process temperature increases or the film is under high in-plane strain condition, both of which promote the FE property. Also, it can be seen that the m-phase starts to appear at process temperature of 330 ℃, indicating that the m-phase becomes stabilized above certain temperature even with the structural similarity between HZO and Ru BE. Since the phase change is a thermally activated process, as also shown in Chapter 3, high temperature would give enough thermal energy to overcome the activation energy barrier between the t-/o-phase and the m-phase.

Fig. 4.6 shows the atomic force microscopy (AFM) image of the HZO thin film deposited at different process temperature of 290, 310, and 330 ℃. The roughness

affects both the crystallinity and electrical behavior. However, the film deposited at 290 and 310 °C showed similar root-mean-square (RMS) value of 1.44 and 1.27 nm, respectively. The RMS value for the film deposited at 330 °C was 7.6 nm with oval shape of hillock-like formation. Sputtered $Hf_{0.5}Zr_{0.5}O_2$ thin film annealed under O_2 ambience showed such behvaior which caused by the oxidation of TiN BE layer.[12] Although TiN BE was not used, in this work, TiN adhesion layer under Ru BE might have oxidized during O_3 oxidant feeding step at high process temeprature of 330 °C. Also, replaced nitrogen with oyxygen could rise to the surface as the gas form which could push up the dielectric layer, causing high roughness. Hence, process tempertaure of 310 °C seems to be the boundary temperature with no abnormal hillock formation or any protrusion.

Fig. 4.7 shows the grain size distribution data obtained through Gwyddion program using images obtained from SEM. Details of the method can be found in other works. [10] The figure shows that the grain size difference of the film deposited at 290, 310, and 330 °C is minimal, and the summary of the grain size and roughness with the respect to the process temperature is shown. Compared to grain size of the HZO thin film grown on TiN BE, grain size of HZO thin film on Ru BE shows a similar value. Such grain size induces o-phase rather than t-phase due to the surface energy effect,[21] which is why the HZO thin film on Ru BE shows ferroelectricity even though the t-phase should be more stable phase on rutile RuO_2, if present. Formation of RuO_2 will be discussed further later in the chapter.

Since the temparture of 310 $^{\circ}$C could be still high, the uniformity of the film was checked by depositing ~40 nm HZO on both Ru and TiN BE. Fig. 4.8 shows the columnar growth of the HZO thin film with high conformity showing that process temperature of 310 $^{\circ}$C would not be too high to affect the film layout.

Fig. 4.9 shows the polarization-electric field (P-E) hysteresis of the ~11.6 nm as-deposited HZO thin film without post-annealing. It is surprising that the film shows full polarization switching behavior with $2P_r \sim 32$ $\mu C/cm^2$ at 4 MV/cm. When the field cycling is conducted with 4 MV/cm, the film showed high leakage current leading to early breakdown below 10^5 field cycling number. When the field-cycling is conducted using 2.5 MV/cm, the film showed a wake-up behavior above 10^5 field cycling and hardbreak at 2.15 x 10^5. Wake-up behavior is a common behavior in FE mateirals that during field-cycling, the defects are redistributed, depining the polarization and increasing the P_r. It is worth noting in Fig. 4.9 that the pristine as-deposited film without any wake-up showed only one current switching peak, indicating that the film is crystallized into the o-phase rather than the t-phase.

Fig. 4.10 shows the film thickness dependence on the polarization switching behavior. Since HZO thin film is not a perfect epitaxial film, BE effect will be significant at thinner film and its effect will decrease as film thickness increases. As expected, the dielectric consatnt decreases as film thickness increases, indicating that high amount of the t-phase is present in 7.6 nm and the m-phase starts to appear at 21

nm. The abasence of the double peak which indicates the presence of the t-phase could be due to the low electric field bias applied to the thin film.

When XRD pattern was obtained as shown in Fig. 4.10, 21 nm film showed the m-phase formation. When compared with HZO thin film deposited on the TiN BE with post-annealing treatment, [22] the HZO film on Ru BE seems to show less amount of the m-phase at 28.5 and 31.6° as film thickness increases. Also, the annealing temperature affects the m-phase formation as well at film thickness of ~10 nm. Compared with the XRD pattern obtained in this work, it is highly meaningful to obtain highly crystallized HZO thin film with similar P_r behavior with low m-phase formation even when the film thickness is above 21 nm.

Based on the the work by Kim et al. and Seo et al., it was expected that Ru BE would be oxidized to RuO_2 during initial ALD growth.[18,19] If Ru is oxidized to rutile RuO_2, it would promote the t-phase and hinder the m-phase due to the small lattice mismatch. The XPS anlysis was conducted to confirm if there has been the RuO_2 formation which would produce the different XPS peak from Ru electrode, as shown in Fig. 4.11 (a). When XPS analysis is conducted, C-C peak should be calibrated to 285 eV due to possible peak shifts from sample charging and other undesired effects during sample preparation. However, Ru has its $3d_{3/2}$ orbital peak near 284 eV, which overlaps with the peak from C-C peak. Therefore, for accurate analysis, Ru $3p_{3/2}$ orbital near 461.2 eV is selected. When the peak was fitted with two sets of peaks, there was a very small RuO_2 peak present. Also, when X-ray fluorescence (XRF) was

measured on the before and after the HZO deposition on Ru BE, as shown in Fig. 4. 11 (b), Ru layer density decreased, indicating that Ru has been oxidized to RuO_2 or RuO_x. However, when time-of-flight secondary ion mass spectrometry (TOF-SIMS) analysis was conducted, as shown in Fig. 4. 11 (b), very little signal of RuO_2 was obtained, indicating that the amount of RuO_2 layer is not significant after the deposition of HZO thin film.

In-plane strain calculation was conducted to see if the film is under proper in-plane tensile strain. Using GIXRD pattern, in-plane strain calclation was conducted and Fig. 4.12 shows that ~11.6 nm HZO film deposited at 310 ºC on Ru BE goes through the same in-plane strain % as that deposited on TiN BE with PMA. [3] When the in-plane strain percentage is above 1.5 %, it is known that condition to obtain o-phase is fulfilled. It seems that Ru electrode, with little support of RuO_2, promotes the the o-phase formation with proper lattice mismatch. In order to see that deposition temperature is not the main factor of t-/o-phase formation, HZO film was also deposited on TiN at the same temeparature. It shows that normal process temperature of HZO thin film on TiN BE renders the amorphous phase at as-deposited state and significant m-phase starts to appear at high process temperature, which was not shown for the film deposited on Ru BE.

When the endurance test was conducted for different film thickness, as shown in Fig. 4.13, all samples went thourgh hard breakdown between 10^5-10^6 cycling. Compared to endurance limit of HZO thin film deposited on TiN BE, the endurance

performance is highly poor. When the high cycling field is applied, the leakage current issue rises, and when the field is low, fatigue problem occurs. It is known that field cycling at coercive field region promotes fatigue beahvior.[13] Overall, it is necessary to enhance the endurance performance by reducing the leakge current.

The initial growth of HZO thin film deposited at 310 °C seems to create large amount of defects, pinning the polarization domain. When the growth bevhaior is compared for HZO on TiN and Ru BE, it can be seen that activation energy changes from 6.96 kJ/mol to 18.21 kJ/mol at tempearture of 290 °C on TiN BE, whereas it changes from 6.36 kJ/mol to 26.36 kJ/mol at tempearture of 310 °C on Ru BE, as shown in Fig. 4.14. Change in activation energy implies that the adsorption of metal precursors chnages its behavior from ALD to CVD growth. The thermal decomposition of metal precursor is not influenced by the type of the BE, and high GPC indicates that the deposition temperature is quite high. Although it has been reported that C concentration increases as process temperature decreases during ALD growth, [14] its concentration increases as process temperature increases during CVD growth. Due to the high concentration of C impuriteis, the leakage current issues were present for film depsoited at 310 °C.

Auger electron spectroscopy (AES) analysis in Fig. 4.15 shows the depth profile for Zr doped HfO$_2$ thin film deposited at 290 and 310 °C. It can be seen that C concentraiton is higher for the film deposited at high temperautre, which would be the cuase of high leakage current. Therefore, it was necessary to decrease the process

temperature even though the crystallinity could decrease. TEMA-Hf and TEMA-Zr shows self-saturation growth behavior on 285 °C as well, as shown in Fig. 4.16. Although GPC of Zr doped HfO_2 on TiN decreased from 1.7 Å/cycle to 1.2 Å/cycle, indicating that the process temperature dropped to ALD window range, the GPC of the film deposited on Ru electrode still showed high GPC. As explained, locally preferential growth promoted the growth and increased the GPC.

Fig. 4.17 shows the P-E analysis of 7.7, 9.9, 19.7 nm HZO thin film deposited at 290 °C deposition temperature after 10^5 field cycling without any post-annealing. Although it seems that the film is not as leaky as the film deposited at 310 °C, low dielectric constant extracted from e-E plot indicates that the film is not as fully crystallized. Also, large m-phase can be seen for 19.7 nm which did not induce any FE switching behavior. It is conjectured that since the film did not have enough thermal energy to locally grow preferentially on Ru electrode, the m-phase inhibition effect was not as significant leading to stable m-phase as thickness increases. When the field-cycling was conducted, overall endurance was enhanced compared to that of 310 °C. However, the film could not endure high field cycling of 3.0 and 3.5 MV/cm, leading to hard breakdown. At 2.5 MV/cm, the film showed fatigue behavior, as shown in Fig. 4.18.

The early hard breakdown may be due to defects that were created during the film growth, which led to post-annealing. The post-annealing process was conducted at 300, 400, 500 °C at N_2 and O_2 ambience, as shown in Fig. 4.19. However, the

annealing condition only degraded the FE behavior. According to the Park et al., post-annealing process led to Ru and Pt diffusion into dielectric layer leading to degraded FE behavior. [8] Fig. 4.20 shows the AES results of HZO thin film with and without post-annealing. There are some Ru amount that diffuse into the HZO layer before post-annealing. However, significant amount of Pt and Ru diffuses into the HZO layer which is the same as the result reported by Park et al. [8] Therefore, annealing process does not render any positive effects on the FE behavior on HZO film on Ru electrode.

This comes to the conclusion that post-annealing does not induce any positive effects and should there be no post-annealing. Since as-deposited film showed high leakage current leading to early break down, Al_2O_3 (AO) layer was inserted. It has been reported that insertion of Al causes increase in the conduction band offset, decreasing the leakage current. [15] 2 cycles of AO have been inserted 6 cycles before the total super cycle ends. Fig. 4.21 shows that leakage current has been suppressed when the deposition temperature changes from 310 to 290 ºC and even further when 2 cycles of AO layer were inserted. P-E hysteresis behavior shows high $2P_r$ values even at high electric field due to leakage current suppression. However, although reduced leakage current led to a longer endurance cycle number, fatigue problem still was not solved.

It has been reported that the fatigue behavior is closely related to the pulse width, amplitude and temperature, which is interconnected to several fatigue mechanism of domain wall pinning, oxygen vacancy re-distribution and injection.[16] RuO_2 is a

conducting oxide electrode which should work as oxygen vacancy sink, taking away oxygen vacancies from the dielectric layer and provide oxygen. However, it is not the case in this work. There seems to be a chare trapping that holds the carriers, hindering the movement and leads to fatigue behavior. Also, as field cycling continues, it seems that dead layer exists holding the charges. If the fatigue is due to the migraiton of free carriers toward the bound charges of the domain walls, fatigue rate should differ since such process requires time, and the slower the switching, the stronger the fatigue. [17] Fig. 4.22 shows the endurance behavior as field-cycling continues for ~6.53 nm of HZO thin film. When the frequency is increased from 100 kHz to 500 kHz and 1 MHz, the fatigue rate seems to decrease, indicating that the fatigue is due to the bound charges of the free carriers. There could be many reasons for such fatigue behavior such as grain size and porosity. As the grain size decreases and the porosity increases, the fatigue becomes more dramatic. [23,24] Considering that HZO film grown on Ru has lower density of 7.9 g/cm^3 than that on TiN of 8.7 g/cm^3, as shown in Fig. 4.23, it seems necessary to make the film denser.

At field cycling frequency of 1 MHz, the film showed very small fatigue behavior with $2P_r$ of ~17 $\mu C/cm^2$ at field cycling number of 10^8. Recent studies have dealt with as-deposited FE film, since post-annealing process renders leakage problem combined with difficulty of crystallization with annealing as the film thickness keeps decreasing. However, no report has shown the endurance property of as-deposited doped HfO_2 thin film, possibly from leakage current or fatigue issues that was present

in this study. Although the fatigue problem was not completely solved for HZO thin film on Ru, the FE behavior of HZO film at as-deposited state is still remarkable. Therefore, it is necessary to figure out whether it is the Ru itself or small presence of RuO_2 that is rendering the in-situ crystallization of HZO film.

To confirm the presence of RuO_2 layer, transmission electron microscopy (TEM) analysis was conducted as shown in Fig. 4.24. It can be clearly seen that HZO film has been fully crystallized even without the post-annealing process. When fast fourier transform (FFT) was conducted on the images, HZO majorly showed o-phase with d-spacing of 2.9-2.98 Å for (111) direction which is quite similar with that obtained from the HZO on TiN BE. [25] Ru BE showed (002) direction as expected from XRD measurements. The presence of RuO_2 is difficult to determine because of its thin thickness and distinguishing the interface between oxide layer and the electrode is challenging. When TEM image was conducted on RuO_2 between TiO_2 and Ru, it was difficult to distinguish each layer as well. [26] Therefore, only the fact that HZO has been well crystallized on Ru BE can be confirmed from TEM analysis.

Even though the deposition temperature of 290 ℃ is within the ALD window, GPC of the HZO on Ru BE is quite high as was shown in Fig. 4.16. To analyze the very initial growth period, shorter than 10 feeding cycle was invested and shown in Fig. 4.25. According to Lee et al., oxide electrode with high formation energy can easily give away the oxygen to dielectric layer deposited on top, causing the initial growth to be highly reactive. [20] In their report, $SrTiO_3$ (STO) grew very quickly on IrO_2,

RuO$_2$, and Ru BE due to the oxygen supply from the BE. Also, in their other report, they have figured out that Ru is the material that can easily oxidize and reduce. This characteristic allows Ru BE to oxidize to rutile RuO$_2$ in the initial step of the ALD process and reduce to Ru during metal precursor feeding. [27] They called this step as substrate-enhanced growth mode. When the thickness gets thicker, dielectric layer gets less influenced by the oxygen supply from the BE and GPC becomes less radical. This saturated-constant GPC occurs during linear-growth mode. It is very likely that such phenomenon is occurring on HZO on Ru BE. During initial ALD growth, Ru oxidizes to rutile RuO$_2$ during O$_3$ feeding step. As subsequent metal precursor starts feeding, it takes the oxygen from RuO$_2$ and becomes metal oxide by reducing RuO$_2$ to Ru. As O$_3$ feeds again, it not only re-oxidizes the Ru but also the metal precursor that is attached either Ru or metal oxide, resulting in more dramatic oxygen scavenging effect than the previous step. As thickness gets thicker, oxygen is no longer supplied from the BE and reaches constant, less radical GPC. The reason why RuO$_2$ was not detected in either XPS or TOF-SIMS (unlike the result from Kim et al.[26]) is RuO$_2$ has been almost completely reduced after few ALD cycling. Considering that HfO$_2$ and ZrO$_2$ has the formation energy of -991 kJ/mol and -1041 kJ/mol compared to that of -833.972 kJ/mol for TiO$_2$, HZO film grabs the oxygen tighter than TiO$_2$ which even causes more reduction of RuO$_2$. To aid in understanding, a schematic figure is prepared in Fig. 4.26.

To further confirm that rutile RuO_2 promotes the HZO t-/o-phase, ~10 nm of HZO thin film was grown on rutile RuO_2 BE. As can be clearly seen by XRD analysis shown in Fig. 4.27, t-/o-phase is highly grown on RuO_2 compared to other BE at the same temperature. Also, O_3 feeding time was varied to manually create the RuO_2 layer from Ru, and as O_3 feeding time increases, higher XRD peak intensity was observed with higher GPC. This implies that longer O_3 feeding makes RuO_2 thicker which can supply more oxygen to HZO layer, boosting up the GPC during intial ALD growth. Therefore, it can be certain that rutile RuO_2 promotes the t-/o-phase within HZO thin film. As mentioned earlier, since the grain size of the film falls into the range where o-phase is stable over t-phase, ferroelectricity was observed for the as-deposited HZO film. Although there is a fatigue problem to be solved, this study could be the starting point that leads to enhanced FE behavior for as-deposited film at a film thickness as low as ~6.5 nm.
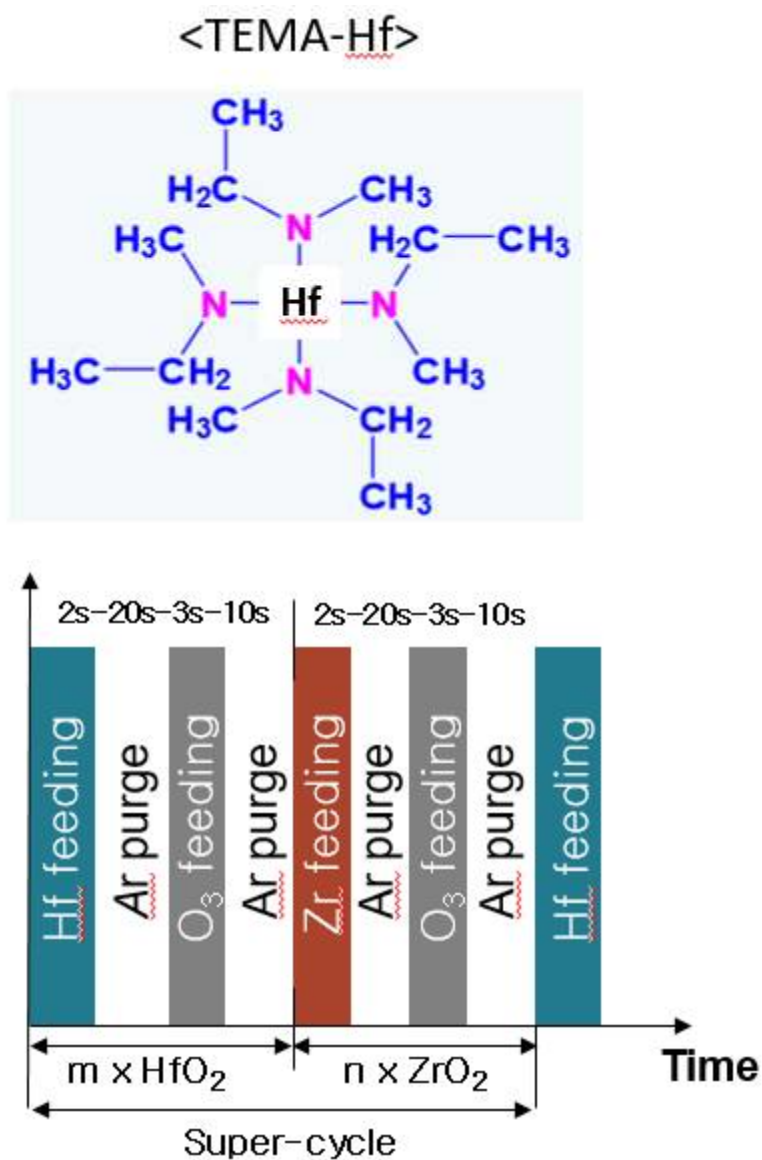
Figure 4.1. Chemical state of TEMA-Hf and ALD cycle step for depositing $Hf_{0.5}Zr_{0.5}O_2$ thin film.
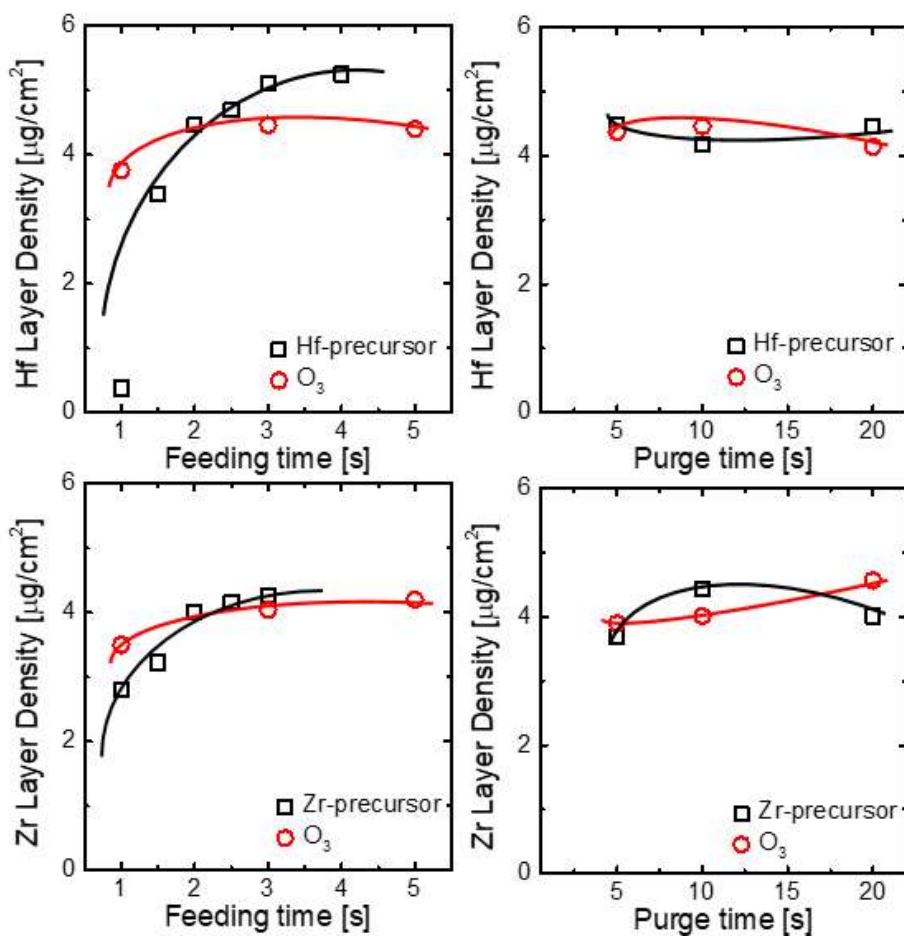
Figure 4.2. Self-saturation behavior using TEMA-Hf and TEMA-Zr for HfO$_2$ and ZrO$_2$, respectively, with respect to metal presursor and O$_3$ feeding time and purge time.
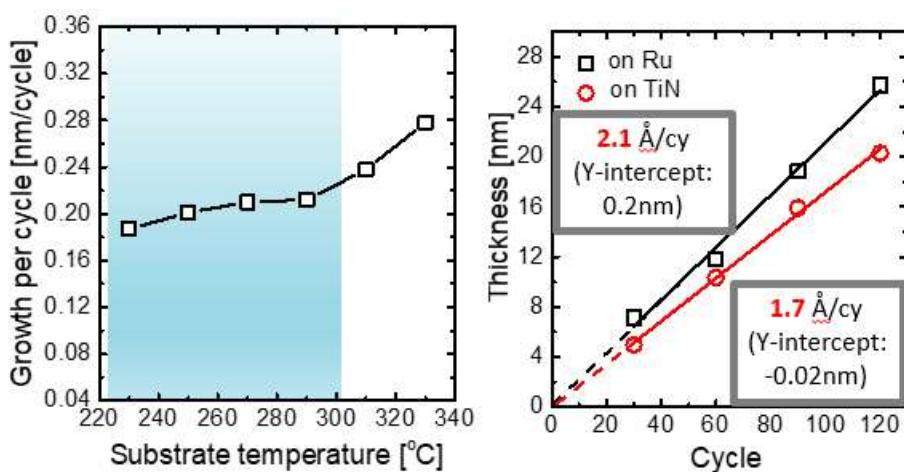
Figure 4.3. Self-saturation behavior using TEMA-Hf and TEMA-Zr for HfO_2 and ZrO_2, respectively, with respect to metal presursor and O_3 feeding time and purge time.
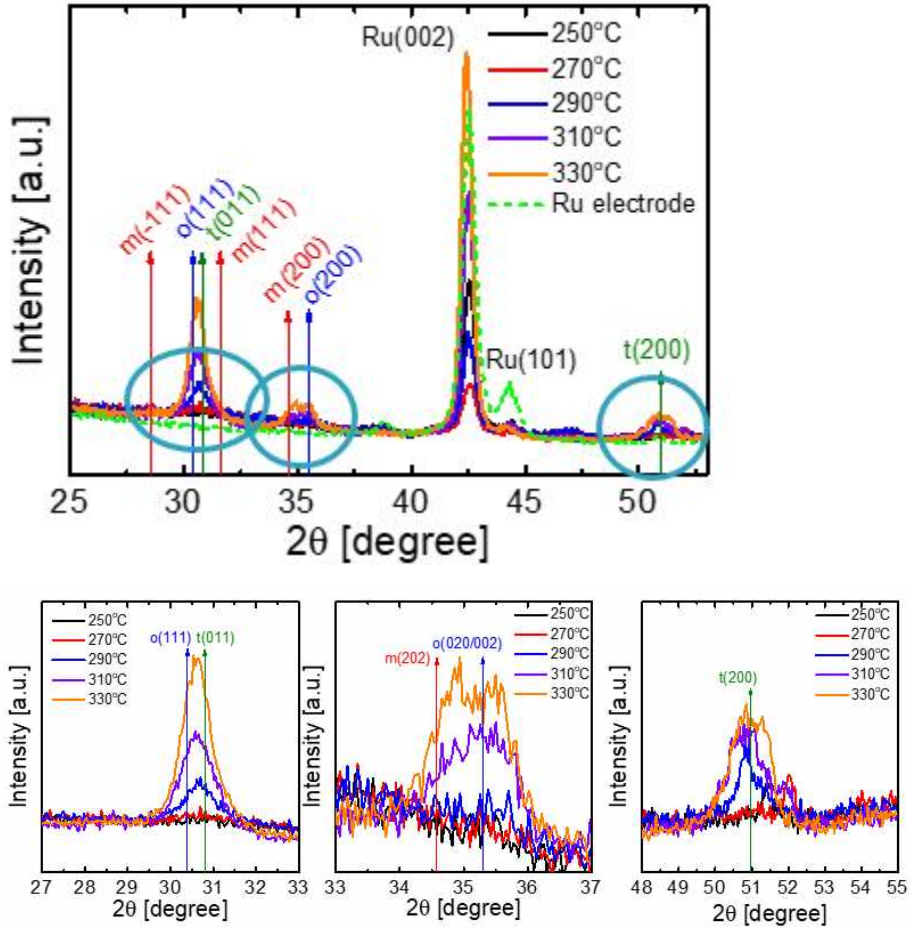
Figure 4.4 Grazing incidence angle X-ray diffraction pattern for ~10 nm $Hf_{0.5}Zr_{0.5}O_2$ thin film deposited at different deposition temperature. Three figures below show an enlarged view of circle region indicated at the top figure.
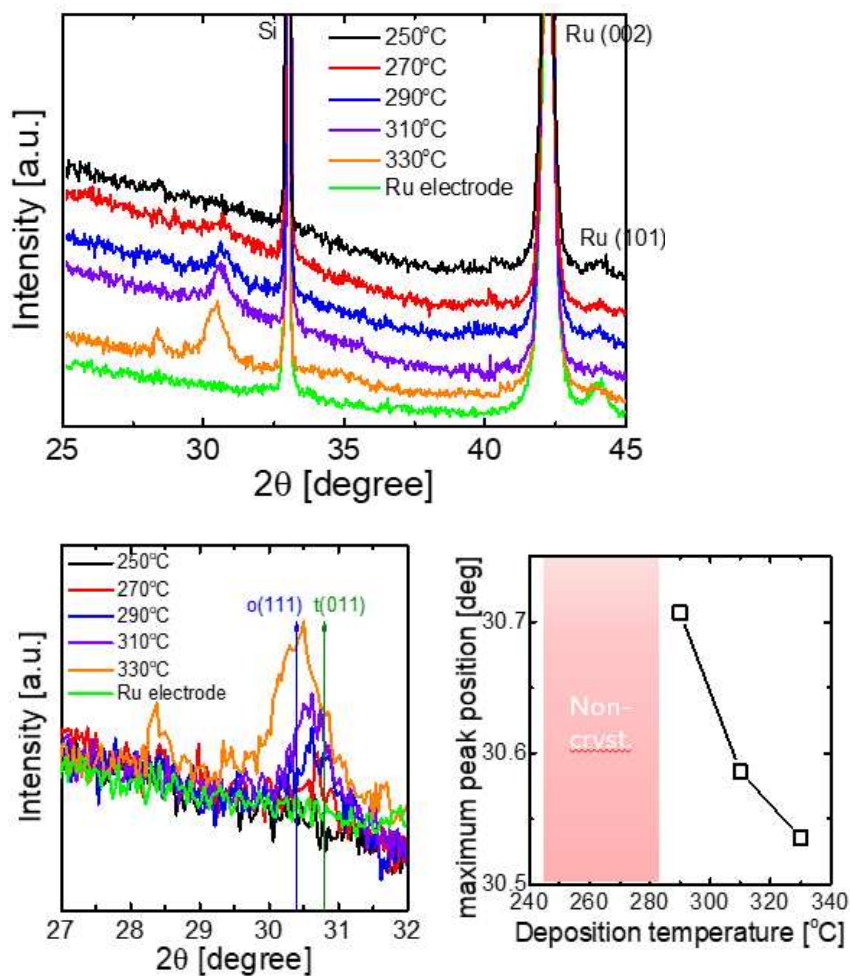
Figure 4.5. Normal θ-2θ X-ray diffraction pattern for ~10 nm $Hf_{0.5}Zr_{0.5}O_2$ thin film deposited at different temperature. Bottom left figure shows enlarged pattern at 27-32° and bottom right figure shows the temperature above which crystallization starts ocurring.
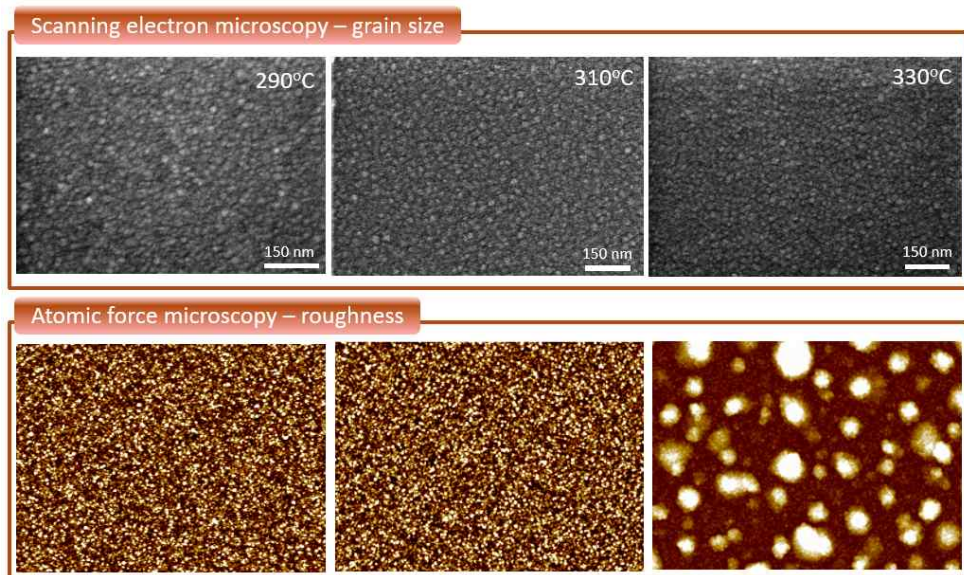
Figure 4.6. Scanning electron microscopy and atomic force microscopy images of~10 nm $Hf_{0.5}Zr_{0.5}O_2$ thin film deposited at 290, 310, and 330 °C deposition temperature.
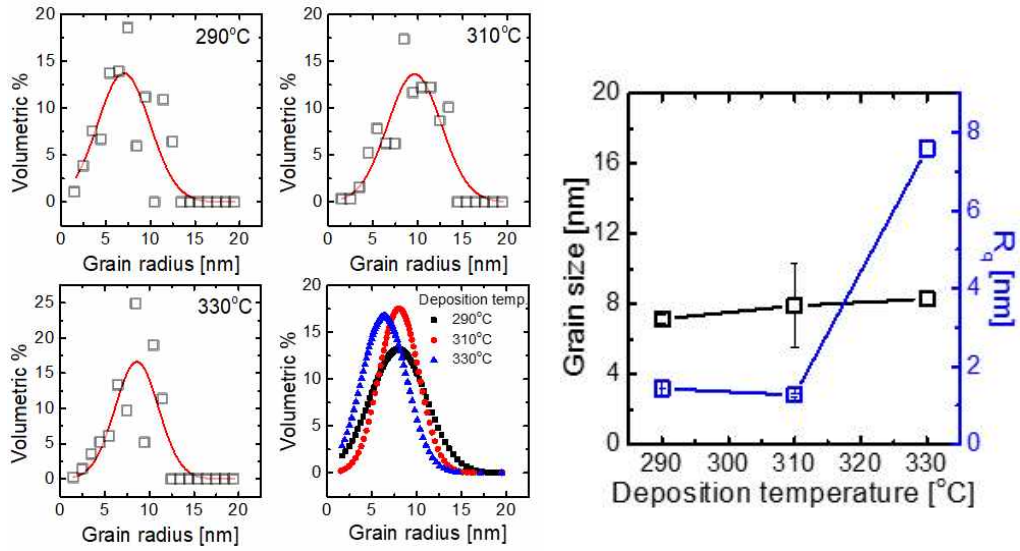
Figure 4.7. Left figure shows grain size distribution data for 290, 310, 330º deposition temperature using Gwyddion software. Right figure shows combination of grain size and mean roughnesss, R_q value, with respect to the deposition temperature

RuO$_2$(20nm)/HZO(40nm)/Ru(30nm)/TiN(8nm)/SiO$_2$
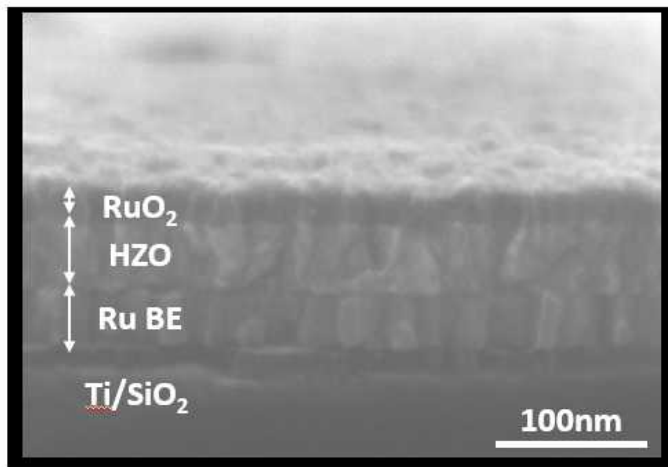
RuO$_2$(20nm)/HZO(40nm)/TiN(50nm)/SiO$_2$
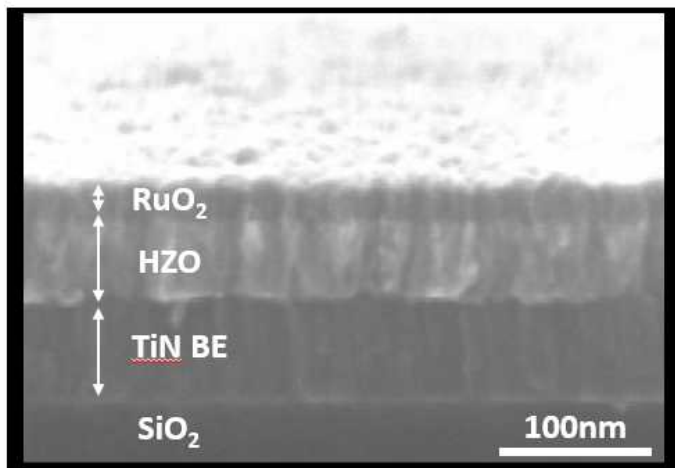
Figure 4.8. Scanning electron microscopy images of ~40 nm Hf$_{0.5}$Zr$_{0.5}$O$_2$ thin film on Ru and TiN bottom electrode
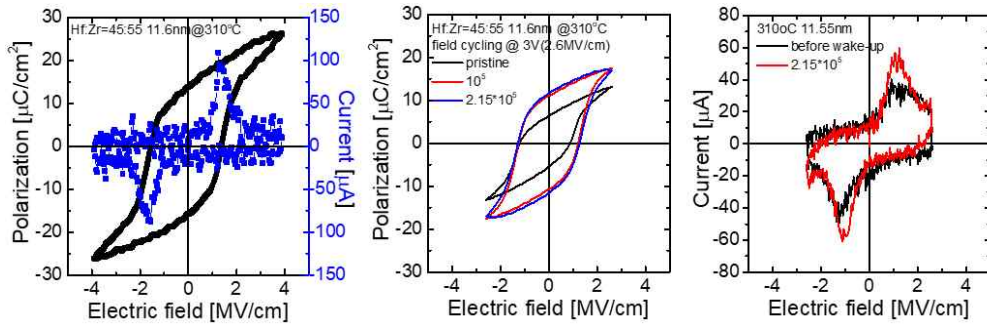
Figure 4.9. P-E analysis of ~11.6 nm $Hf_{0.45}Zr_{0.55}O_2$ thin film deposited at 310°C. Center figure shows the wake-up behavior and right figure shows current-electric field data
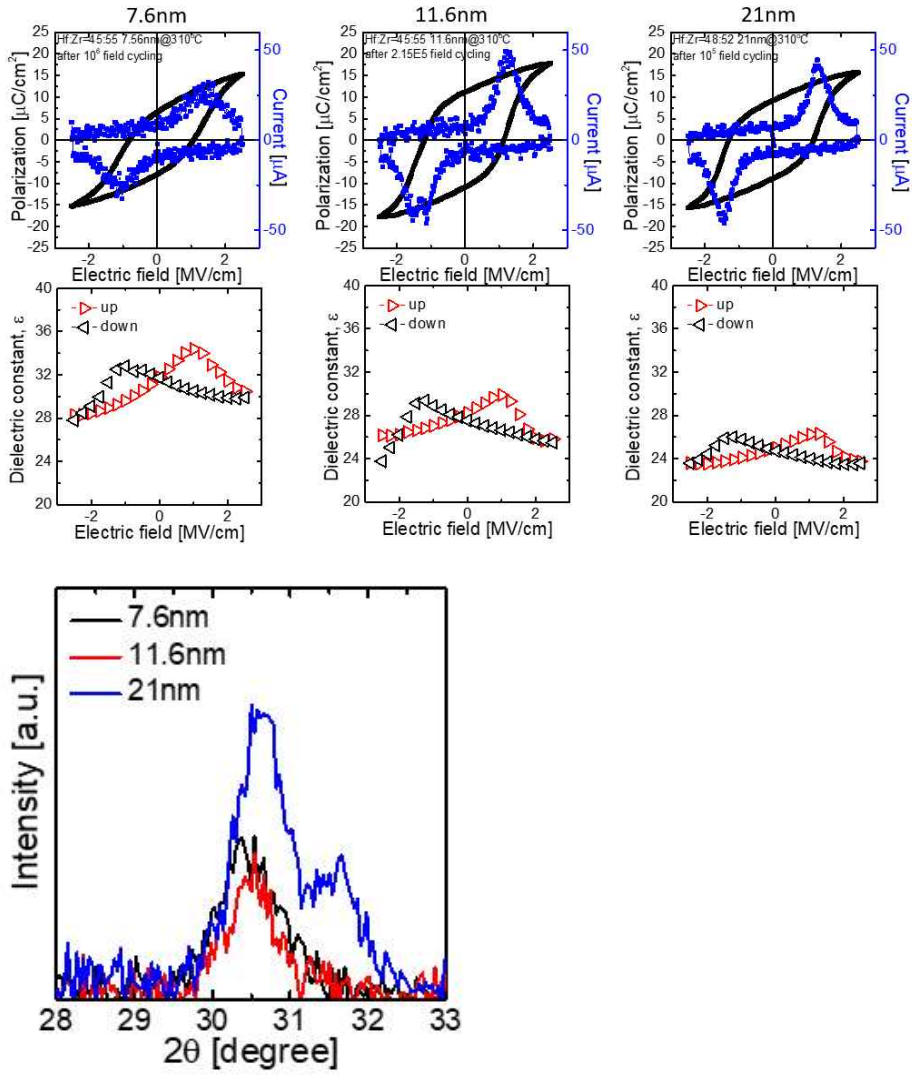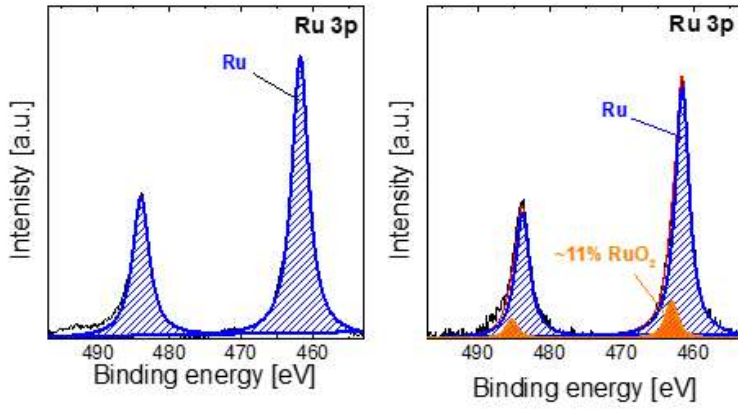
Figure 4.10. P-E and ε-E analysis for (Hf,Zr)O$_2$ thin film deposited at different

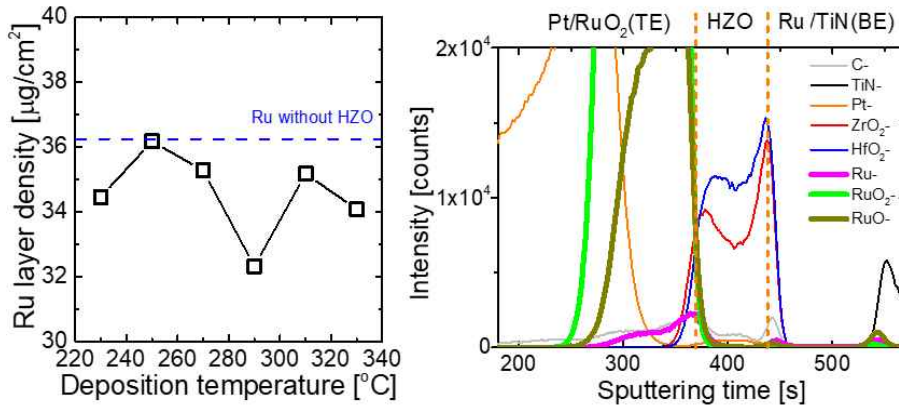temperature. Bottom figure shows X-ray diffraction pattern for different thickness

(a)

(b)

Figure 4.11. (a) X-ray photoelectron spectroscopy of Ru 3P orbital for ~10 nm $Hf_{0.5}Zr_{0.5}O_2$ thin film using interface analysis mode. (b) X-ray fluorescence before and after deposition of $Hf_{0.5}Zr_{0.5}O_2$ and time of flight secondary ion mass spectrometry of ~ 10 nm $Hf_{0.5}Zr_{0.5}O_2$ thin film.
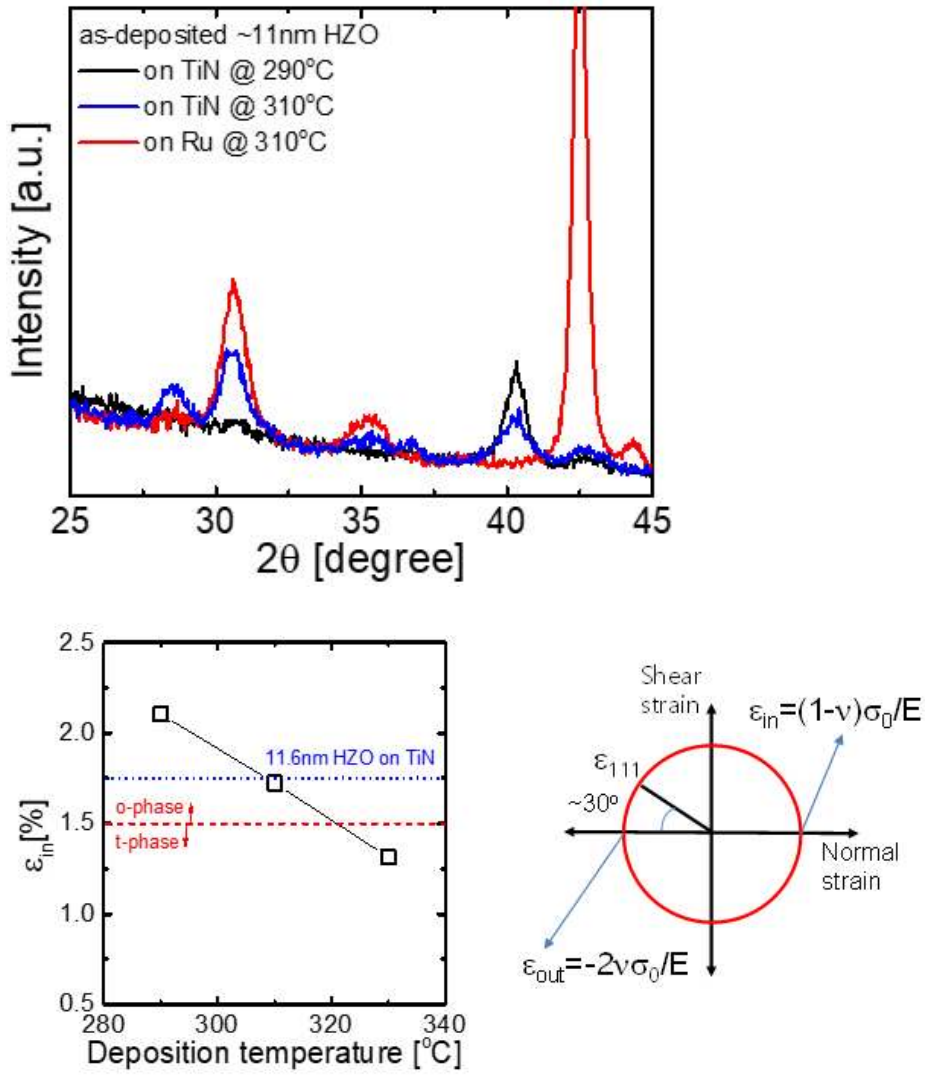
Figure 4.12. Grazing incidence angle X-ray diffraction pattern for ~11 nm $Hf_{0.5}Zr_{0.5}O_2$ thin film deposited at different temperature on TiN and Ru bottom electrode. Bottom left figure shows the Mohr Circle used to calculate the in-plane strain % shown on the bottom right figure.
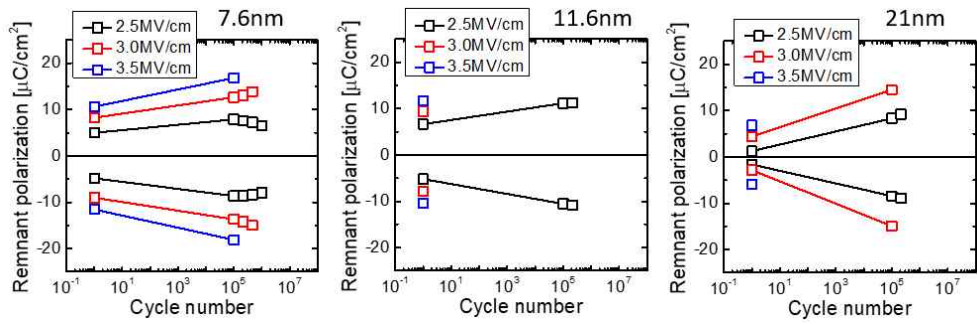
Figure 4. 13. Endurance test for $Hf_{0.5}Zr_{0.5}O_2$ thin film deposited at different thickness using different electric field.
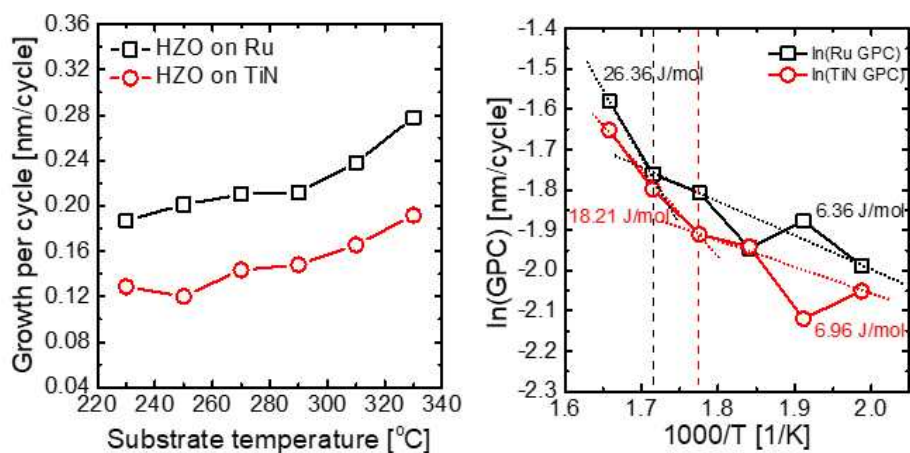
Figure 4.14. Growth per cycle of $Hf_{0.5}Zr_{0.5}O_2$ thin film deposited on Ru and TiN bottom electrode.
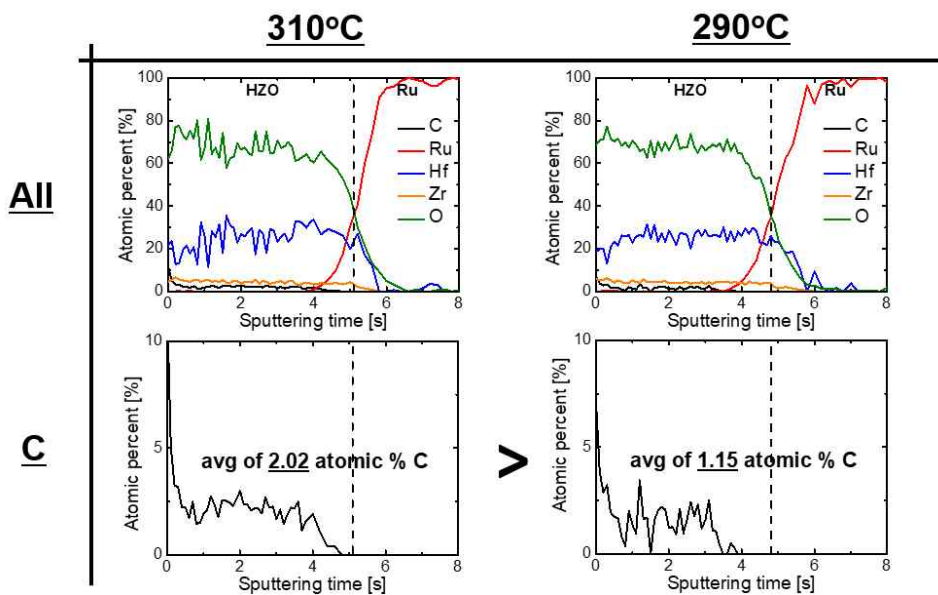
Figure 4.15. Auger electron spectroscopy for $Hf_{0.5}Zr_{0.5}O_2$ thin film deposited at 310 and 290 $^{\circ}$C.
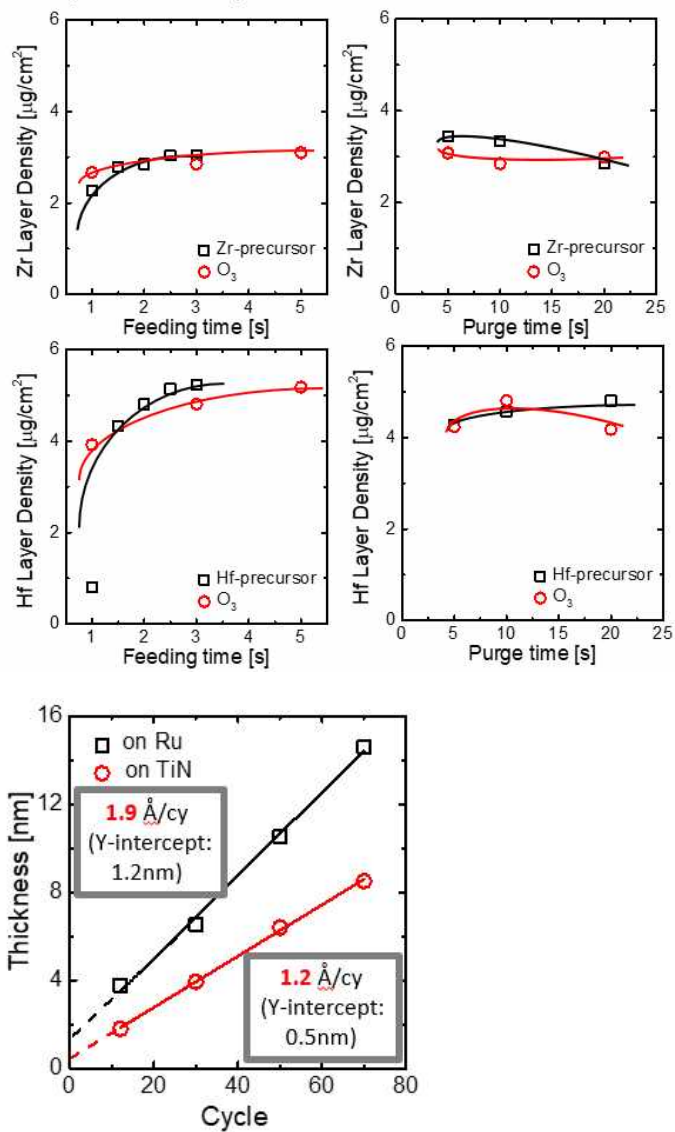
◆ Deposition temperature at 310°C -> 290°C

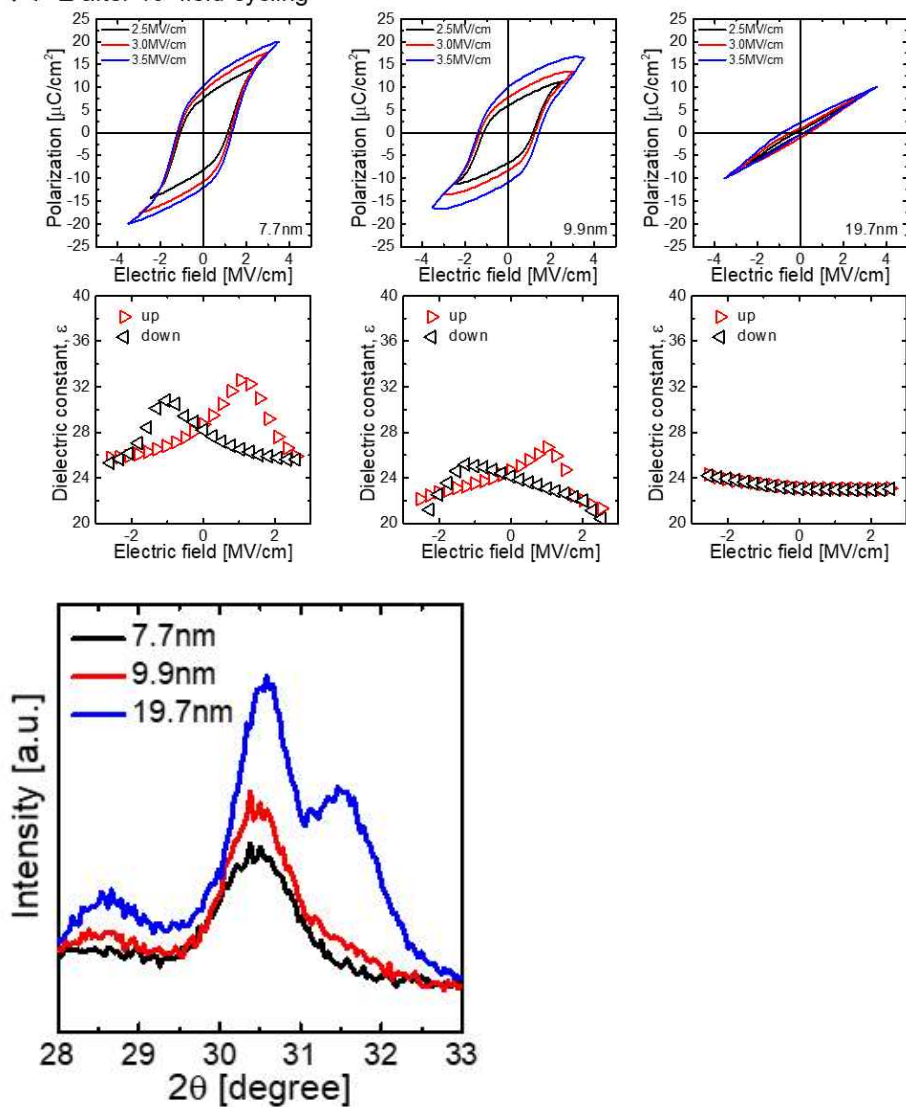Figure 4.16. Self-saturation behavior for HfO_2 and ZrO_2 when the deposion temperature changed from 310 to 290°C.

101

Figure 4.17. P-E and ε-E analysis after 10^5 field cycling. Bottom figure shows the X-ray diffraction pattern with at different thickness.

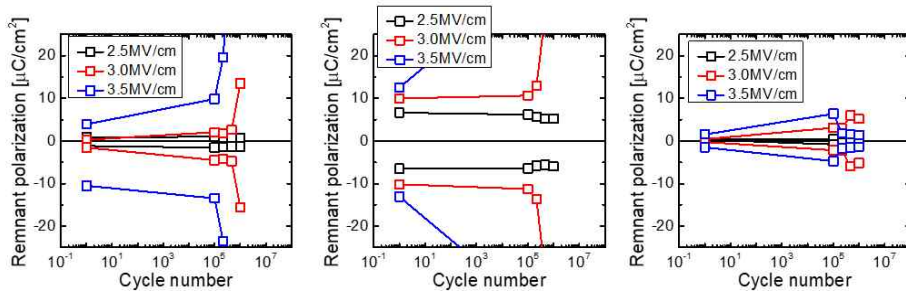Figure 4.18. Endurance test for $Hf_{0.5}Zr_{0.5}O_2$ thin film deposited at different thickness using different electric field at 290 ºC deposition temperature.
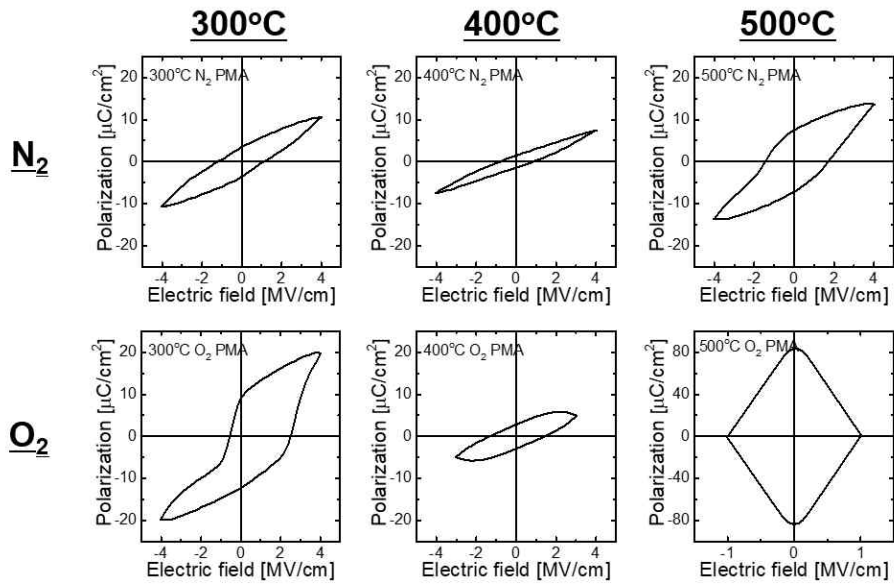
Figure 4.19. P-E analysis after post-metallization annealing at 300, 400, 500 °C under N_2 and O_2 ambience
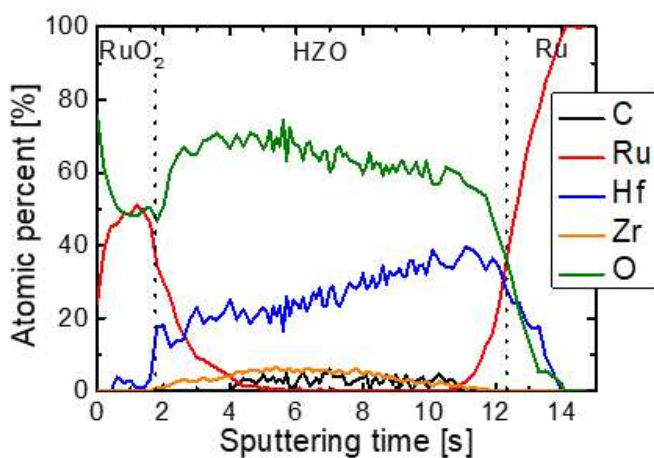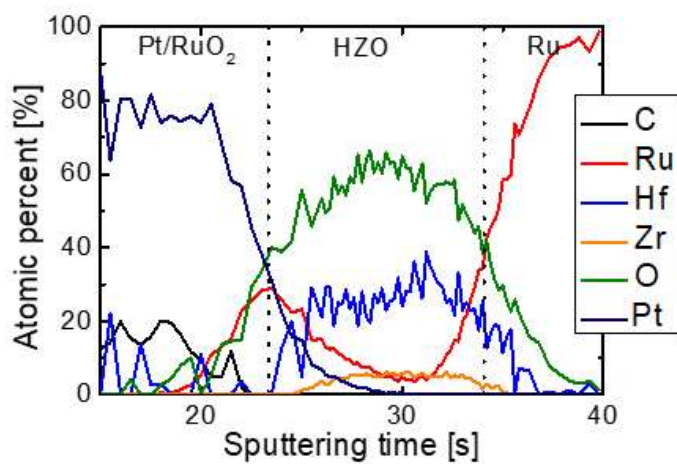
Figure 4.20. Auger electron spectroscopy of $Hf_{0.5}Zr_{0.5}O_2$ thin film deposited on Ru before and after post-metallization-annealing
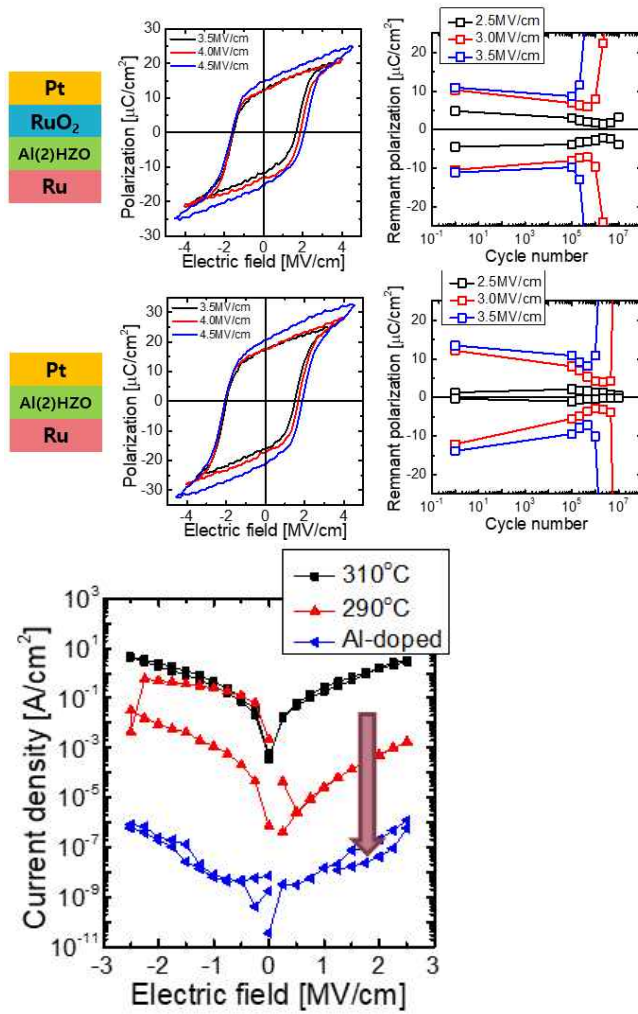
Figure 4.21. P-E and endurance analysis after insertion of 2 Al$_2$O$_3$ layers. Bottom figure shows the J-E curve for Hf$_{0.5}$Zr$_{0.5}$O$_2$ thin filmi deposited at different temperature and Al$_2$O$_3$ layer insertion
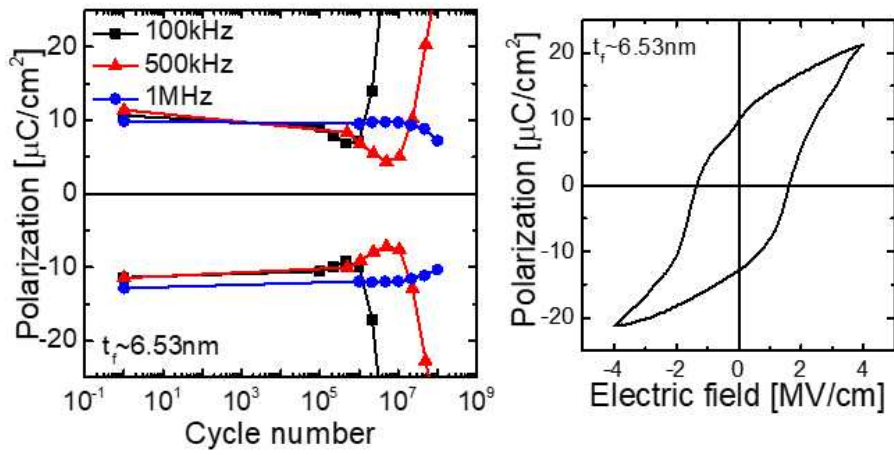
Figure 4.22. Endurance test at different frequency and P-E hysteresis of ~6.53 nm of $Hf_{0.5}Zr_{0.5}O_2$ thin film.
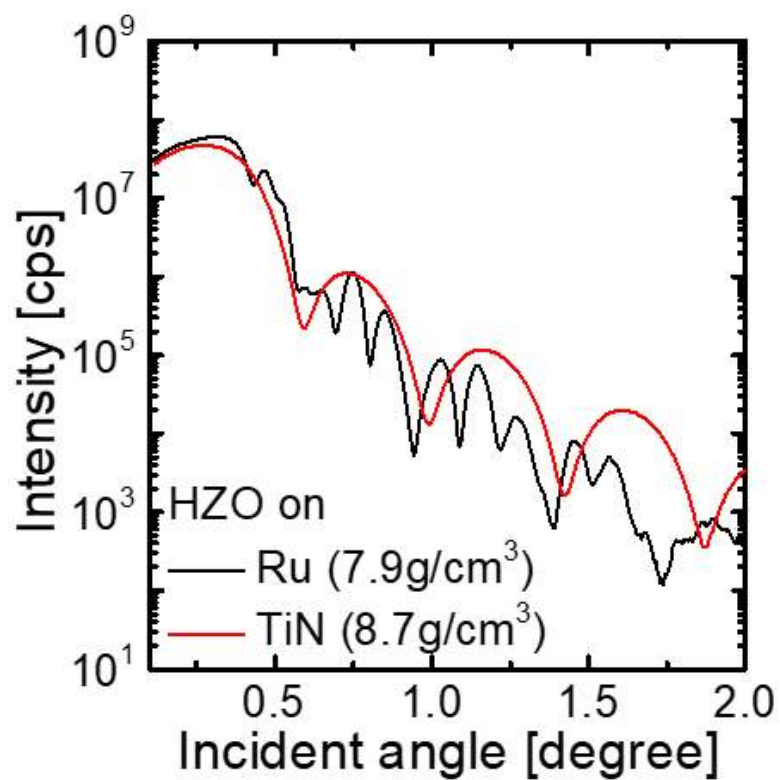
Figure 4.23. X-ray reflectivity of ~10 nm $Hf_{0.5}Zr_{0.5}O_2$ thin film grown on TiN and Ru BE.
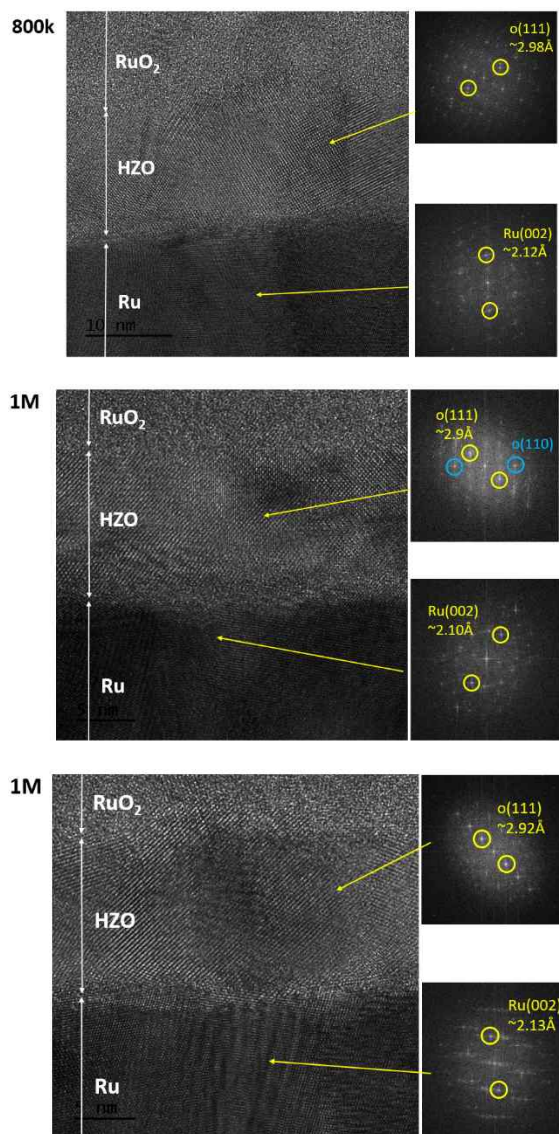
Figure 4.24. Transmission electron microscope images of RuO_2 / ~12 nm $Hf_{0.5}Zr_{0.5}O_2$ / Ru bottom electrode.
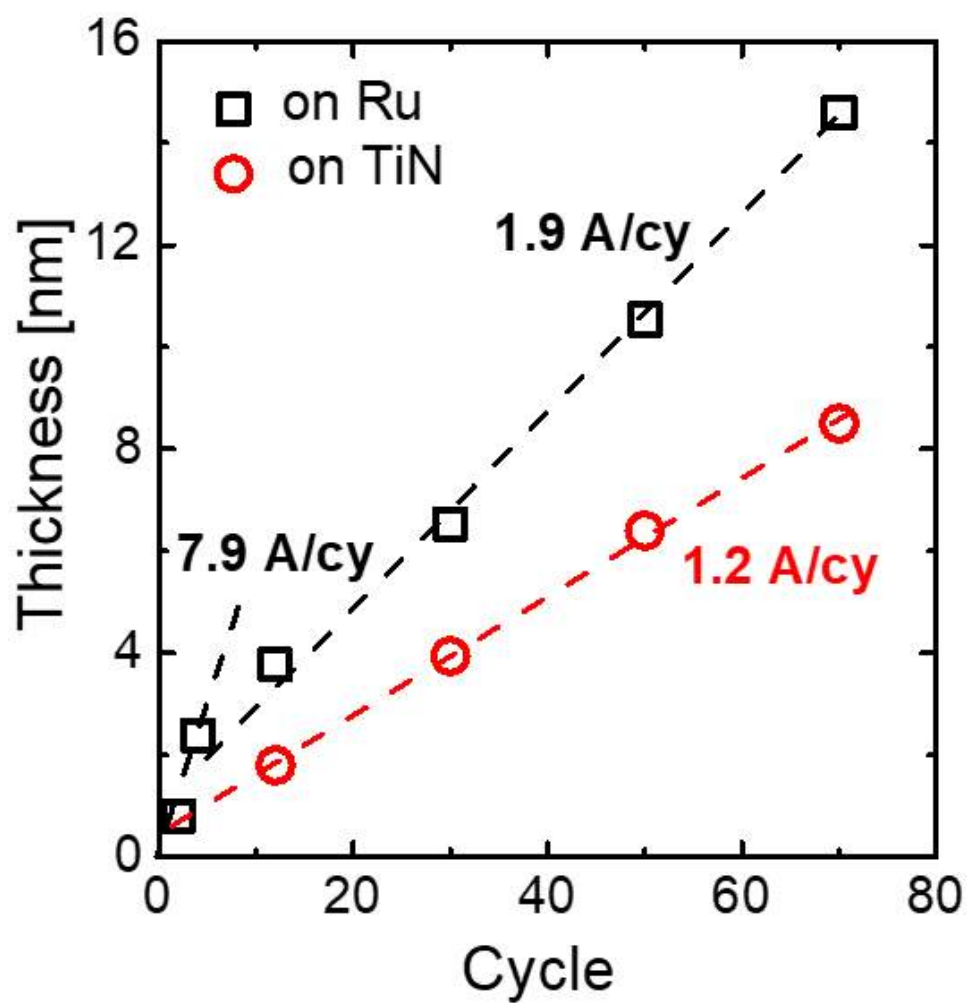
Figure 4.25. Thickness versus cycle of $Hf_{0.5}Zr_{0.5}O_2$ thin film on TiN and Ru bottom electrode. Initial growth of $Hf_{0.5}Zr_{0.5}O_2$ thin film on Ru showed 7.9 Å/cycle.
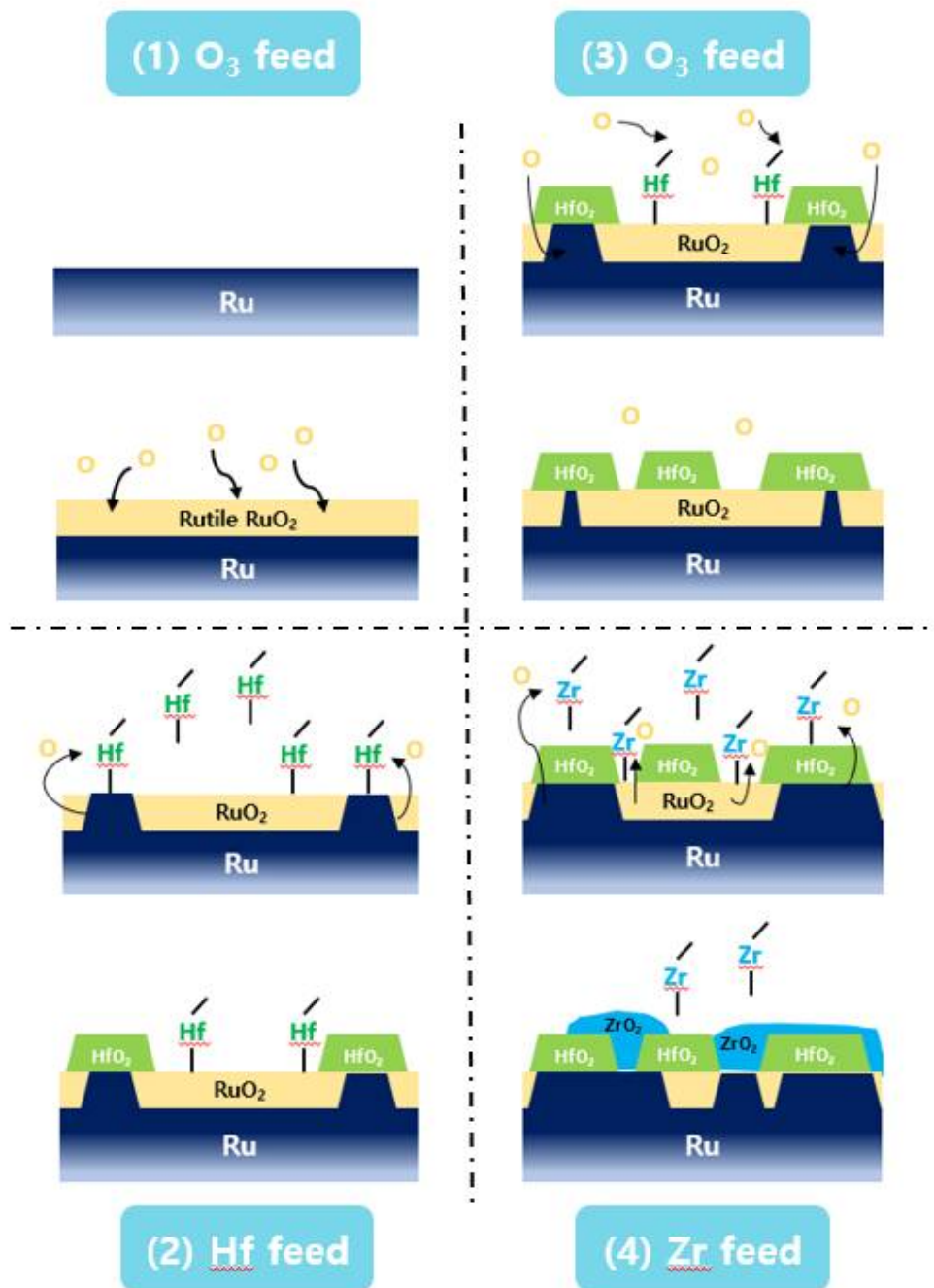
Figure 4.26. Schematics of Ru redox reaction during initial ALD growth.

111
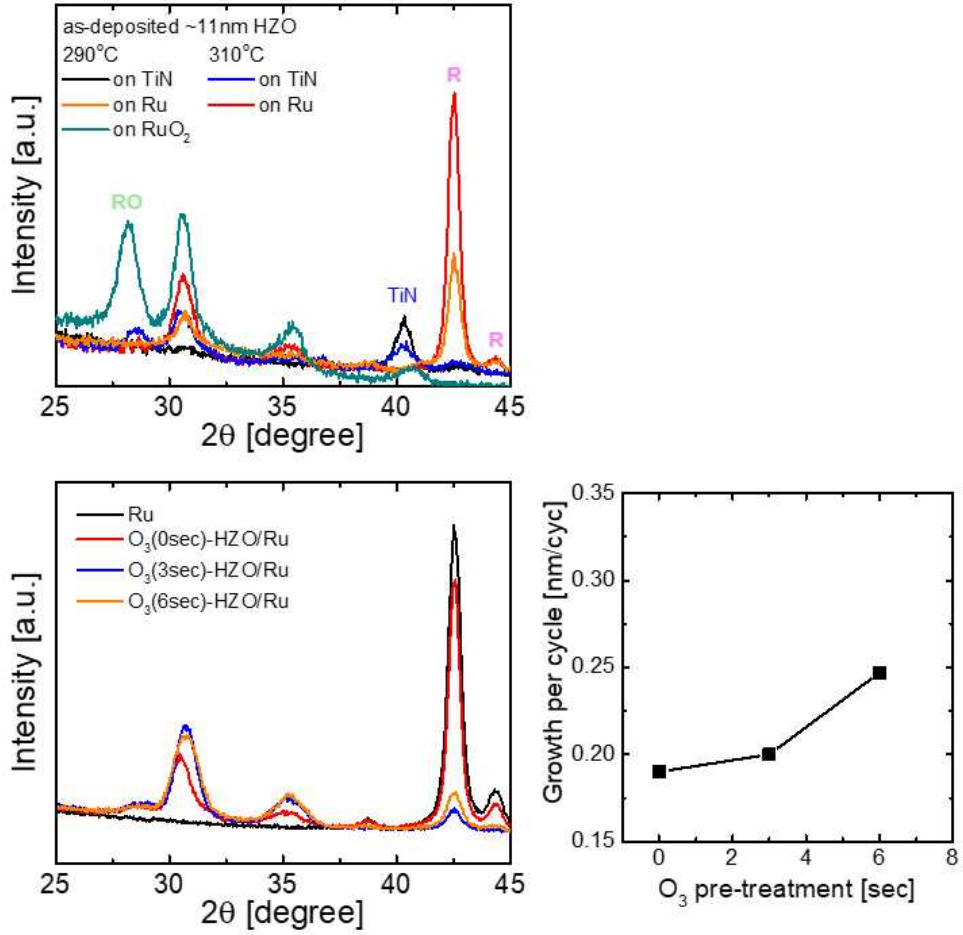
Figure 4.27. (top) X-ray diffraction pattern for $Hf_{0.5}Zr_{0.5}O_2$ thin film deposited on various bottom electrodes. (bottom right) X-ray diffraction pattern for $Hf_{0.5}Zr_{0.5}O_2$ thin film with initial pre-feeding of O_3 for 3 and 6 seconds. (bottom left) Growth per cycle as O_3 pre-feeding time varies.

4.4. Conclusion

In summary, ~10 nm of HZO thin film has been deposited on Ru BE using TEMA-Hf and TEMA-Zr using ALD. During the initial ALD growth, rutile RuO2 layer was formed which promoted the formation of the t-/o-phase within the HZO film. This was confirmed by RuO_2 BE and high GPC of HZO thin film on Ru and O_3 pre-treated Ru, which was much higher than that on TiN BE. Oxidized RuO_2 was reduced again during metal precursor feeding step, which was why RuO_2 was not detected in either XPS or TOF-SIMS analysis. The as-deposited film showed $2P_r$ of ~23 $\mu C/cm^2$ at 2.5 MV/cm which is almost comparable to ~10 nm HZO deposited on TiN BE with post-annealing process. The small lattice mismatch between rutile RuO_2 and t-/o-phase of HZO rendered in-plane tensile strain above 1.5 % which came out to be the same as that obtained for HZO thin film deposited on TiN BE after post-annealing process.

Although FE behavior is outstanding at as-deposited state, high leakage current hindered high endurance performance. This could cause from the C impurities which was confirmed by AES. In order to decrease the C impurities, the deposition temperature was lowered to 290 ºC, which falls under the ALD temperature range. However, lower deposition temperature led to lower effect from the Ru electrode which induced formation of the m-phase or amorphous phase in the film, confirmed by smaller dielectric constant. Due to smaller C impurities, endurance cycling was tested and the film endured longer cycling than that deposited at 310 ºC. However,

the hard break down occurred near 10^5 cycling number, which is much lower than 10^7 cycling number obtained from HZO thin film deposited on TiN after post-annealing. The choice of the TE can affect the endurance behavior but changing the TE to Pt did not induce much difference indicating that the fatigue behavior could be arising from the Ru BE. When the measuring frequency is varied, the fatigue rate decreased as frequency increased, indicating that the fatigue is arising from the migration of free carriers toward the bound charges of the domain walls. Although there exists much enhancement to do, ~6.53 nm of HZO showed $2P_r$ value of ~17 $\mu C/cm^2$ at cycling number of 10^8.

4.5. Bibliography

1. T. S. Böscke , J. Müller , D. Bräuhaus , U. Schröder , U. Böttger , *Appl. Phys. Lett.* 2011 , 99 , 102903.

2. J. F. Scott , *Ferroelectric Memories* , Springer-Verlag , Berlin, Germany 2000 .

3. M. H. Park , H. J. Kim , Y. J. Kim , T. Moon , C. S. Hwang *Appl. Phys. Lett.* 2014, 104 , 072901

4. J. Müller , T. S. Böscke , D. Bräuhaus , U. Schröder , U. Böttger , J. Sundqvist , P. Kücher , T. Mikolajick , L. Frey , *Appl. Phys. Lett*. 2012. 99 , 112901.

5. J. Müller , U. Schröder , T. S. Böscke , I. Müller , U. Böttger , L. Wilde , J. Sundqvist , M. Lemberger , P. Kücher , T. Mikolajick , L. Frey *, J. Appl. Phys.* 2011, 110, 114113

6. J. C. Slater , *J. Chem. Phys*. 1964, 41, 3199 .

7. M. H. Park, H. J. Kim, Y. J. Kim, W. Lee, H. K. Kim, C. S. Hwang *Appl. Phys. Lett.* 2013, 102, 112914

8. M. H. Park, H. J. Kim, Y. J. Kim, W. Jeon, T. Moon, c. S. Hwang *Phys. Status Solidi RRL,* 2014, 1-4

9. B-T Lin, Y-W Lu, J. Shieh, M-J Chen *Journal of the European Ceramic Society* 2017, 37, 1135-1139

10. D. Necas, P. Klapetek, *Cent. Eur. J. Phys.* 2012, 10, 181.

11. T. Schenk, C. M. Fancher, M. H. Park, C. Richter, C. Kunneth, A. Kersch, J. L. Jones, T. Mikolajick, U. Schroeder, ″On the origin of the large remanent polarization in La:HfO$_2$″ under review

12. Y. H. Lee, H. J. Kim, T. Moon, K. D. Kim, S. D. Hyun, H. W. Park, Y. B. Lee, M. H. Park, C. S. Hwang *Nanotechnology* 2017, 28, 305703

13. S-K Hong, H. J. Kim, H. G. Yang, *J. Electrochem. Soc.* 2002, 149, 10, F152

14. K. D. Kim, M. H. Park, H. J. Kim, Y. J. Kim, T. Moon, Y. H. Lee, S. D. hyun, T. Gwon, C. S. Hwang *J. Mater. Chem. C* 2016, 4, 6864

15. W. Jeon, S. H. Rha, W. Lee, Y. W. Yoo, C. H. an, K. H. Jung, S. K. Kim, C. S. Hwang *ACS Applied Materials and Interfaces* 2014, 10, 6, 7910

16. M. Pesic, F. P. G. Fengler, L. Larcher, A. Padovani, T. Schenk, E. D. Grimley, X. Sang, J. M. LeVeau, S. Slesazeck, U. Schroeder, T. Mikolajick *Adv. Funct. Mater.* 2016, 26, 4601-4612

17. F. Huang, X. Chen, X. Liang, J. Qin, T. Zhang, T. Huang, Z. Wang, B. Peng, P Zhou, H. Lu, L. Zhang, L. Deng, M. Liu, Q. Liu, H. Tian, L Bi Phys. *Chem. Chem. Phys* 2017, 19, 3486-3497

18. S. K. Kim, K. M. Kim, W. D. Kim, C. S. Hwang, *Appl. Phys. Lett*, 2004, 18, 85, 4112

19. M. Seo, S. K. Kim, J. H. Han, C. S. Hwang *Chem. Mater.* 2010, 22, 4419

20. S. W. Lee, J. H. Han, S. Han, W. Lee, J. H. Jang, M. Seo, S. K. Kim, C. Dussarrat, J. Gatineau, Y-S. Min, C. S. Hwang *Chem. Mater.*2011, 23, 2227.

21. R. Materlik, C. Kunneth, A. Kersch, *J. Appl. Phys.* 2015, *117*, 134109.

22. M. H. Park, H. J. Kim, Y. J. Kim, W. Lee, T. Moon, C. S. Hwang, *Appl. Phys. Lett.* 2013, *102*, 242905.

23. F. Yan, P. Bao, H. L. W. Chan, C.-L. Choy, Y. Wang *Thin Solid Films* 2002, 406, 282

24. X. J. Lou, *J. Appl. Phys.* 2009, 105, 024101

25. H. J. Kim, M. H. Park, Y. J. Kim, Y. H. Lee, W. Jeon, T. Gwon, T. Moon, K. D. Kim, C. S. Hwang *Appl. Phys. Lett.* 2014, 19, 105, 192903

26. S. K. Kim, G. W. Hwang, W.-D. Kim, C. S. Hwang *Electrochem. Solid State Lett.* 2006, 9 (1) F5-F7

27. S. W. Lee, J. H. Han, S. K. Kim, S. Han, W. Lee, C. S. Hwang *Chem. Mater.* 2011, 23, 976-983.

5. Conclusion

In this dissertation, the study on the ~10 nm of ferroelectric $Hf_{0.5}Zr_{0.5}O_2$ thin film was conducted with regards to the top and the bottom electrode. First part of the dissertation covered the nucleation and growth behavior of ~10 nm $Hf_{0.5}Zr_{0.5}O_2$ thin film with and without the TiN top electrode during post-annealing process. It was found out that the phase transformation from the tetragonal phase to monoclinic phase is hindered when the top electrode is capped during post-annealing process. Classical John-Mehl-Avrami model could not describe the nucleation and growth behavior of polycrystalline $Hf_{0.5}Zr_{0.5}O_2$ thin film, which led to new nucleation-limited-transformation model, taking dispersion time of nucleation into account. As a result, TiN top electrode not only deterred the phase transformation from the tetragonal to the monoclinic phase, but also disperses the nucleation time.

Second part of the dissertation covers the effect of the bottom electrode, Ru. When rutile RuO_2 is formed during initial atomic layer deposition process, due to the small lattice mismatch between the rutile phase and the HfO_2 tetragonal phase, the monoclinic phase formation was hindered and tetragonal/orthorhombic phase was promoted even without post-annealing process. Decreasing the deposition temperature from 310 to 290 ºC induced less C impurity and smaller leakage current, yet it required further suppression by using Al_2O_3 layer insertion. However, the fatigue problem occurred which was due to migration of free carriers toward the

118

bound charges of the domain walls. To be free from such effect, the measuring frequency was increased to 1 MHz, and ~6.53 nm of $Hf_{0.5}Zr_{0.5}O_2$ thin film showed $2P_r$ value of ~17 $\mu C/cm^2$ at cycling number of 10^8.

It is believed that this study of the top and bottom electrode would enhance the understanding the formation of the ferroelectric phase within $Hf_{0.5}Zr_{0.5}O_2$ thin film, and promote further studies to improve its performances at thinner films for future technology node.

List of Publications

1. Referred Journal Articles (SCI)

\<First author\>

1. **<u>Y. H. Lee</u>**, S. D. Hyun, H. J. Kim, J. S. Kim, C. Yoo, T. Moon, K. D. Kim, H. W. Park, Y. B. Lee, B. S. Kim, J. Roh, M. H. Park, C. S. Hwang "Nucleation-Limited Ferroelectric Orthorhombic Phase Formation in $Hf_{0.5}Zr_{0.5}O_2$ Thin Films" *Adv. Elec. Mater.* 1800436 (2018)

2. **<u>Y. H. Lee</u>**, H. J. Kim, T. Moon, K. D. Kim, S. D. Hyun, H. W. Park, Y. B. Lee, M. H. Park, C. S. Hwang "Preparation and Characterization of Ferroelectric $Hf_{0.5}Zr_{0.5}O_2$ Thin Films Grown by Reactive Sputtering" *Nanotechnology* 28, 30, 305703 (2017)

\<Co-author\>

1. M. H. Park, H. J. Kim, G. Lee, J. Park, **<u>Y. H. Lee</u>**, Y. J. Kim, T. Moon, K. D. Kim, S. D. Hyun, H. W. Park, H. J. C, J.-H. Choi, C. S. Hwang "A comprehensive study on the mechanism of ferroelectric phase formation in hafniazirconia nanolaminates and superlattices" *Applied Physics Reviews*, 6, 041403 (2019)

2. M. H. Park, **<u>Y. H. Lee</u>**, C. S. Hwang "Understanding ferroelectric phase formation in doped HfO2 thin films based on classical nucleation theory"

Nanoscale 11, 19477-19487 (2019)

3. K. D. Kim, Y. J. Kim, M. H. Park, H. W. Park, Y. J. Kwon, Y. B. Lee, H. J. Kim, T. Moon, **Y. H. Lee**, S. D. Hyun, B. S. Kim, C. S. Hwang "Transient negative capacitance effect in atomic-layer-deposited Al_2O_3/$Hf_{0.3}Zr_{0.7}O_2$ bilayer thin film" *Adv. Funct. Mater*. 1808228 (2019)

4. M. H. Park, **Y. H. Lee**, T. Mikolajick, U. Schroeder, C. S. Hwang "Thermodynamic and kinetic origins of ferroelectricity in fluorite structure oxides" *Adv. Elec. Mater.* 1800522 (2018)

5. M. H. Park, **Y. H. Lee**, H. J. Kim, Y. J. Kim, T. Moon, K. D. Kim, S. D. Hyun, C. S. Hwang "Morphotropic Phase Boundary of $Hf_{1-x}Zr_xO_2$ Thin Films for Dynamic Random Access Memories" *ACS Appl. Mater. Interfaces* 10, 49, 42666 (2018)

6. S. D. Hyun, H. W. Park, Y. J. Kim, M. H. Park, **Y. H. Lee**, H. J. Kim, Y. J. Kwon, T. Moon, K. D. Kim, Y. B. Lee, B. S. Kim, C. S. Hwang "Dispersion in Ferroelectric Switching Performance of Polycrystalline $Hf_{0.5}Zr_{0.5}O_2$ Thin Films" *ACS Appl. Mater. Interfaces* 10, 41, 35374 (2018)

7. T. Moon, H. J. Lee, K. D. Kim, **Y. H. Lee**, S. D. Hyun, H. W. Park, Y. B. Lee, B. S. Kim, C. S. Hwang "Diode Property and Positive Temperature Coefficient of Resistance of Pt/Al_2O_3/Nb:$SrTiO_3$" *Adv. Elect. Mater.* 4, 12, 1800388 (2018)

8. M. H. Park, **Y. H. Lee**, T. Mikolajick, U. Schroeder, C. S. Hwang "Review and perspective on ferroelectric HfO_2-based thin films for memory applications" *MRS*

Communications 8, 3, 795-808 (2018)

9. M. H. Park, **<u>Y. H. Lee</u>**, H. J. Kim, Y. J. Kim, T. Moon, K. D. Kim, S. D. Hyun, T. Mikolajick, U. Schroeder, C. S. Hwang "Understanding the formation of the metastable ferroelectric phase in hafnia-zirconia solid solution thin films" *Nanoscale* 10, 716-725 (2018)

10. Y. J. Kim, H. W. Park, S. D. Hyun, H. J. Kim, K. D. Kim, **<u>Y. H. Lee</u>**, T. Moon, Y. B. Lee, M. H. Park, C. S. Hwang "Voltage Drop in a Ferroelectric Single Layer Capacitor by Retarded Domain Nucleation" *Nano Lett.* 17, 7796-7802 (2017)

11. K. D. Kim, **<u>Y. H. Lee</u>**, T. Gwon, Y. J. Kim, H. J. Kim, T. Moon, S. D. Hyun, H. W. Park, M. H. Park, C. S. Hwang "Scale-up and optimization of HfO_2-ZrO_2 solid solution thin films for the electrostatic supercapacitors" *Nano Energy* 39, 390-399 (2017)

12. M. H. Park, **<u>Y. H. Lee</u>**, H. J. Kim, T. Schenk, W. Lee, K. D. Kim, F. P. G. Fengler, T. Mikolajick, U. Schroeder, C. S. Hwang "Surface and grain boundary energy as the key enabler of ferroelectricity in nanoscale hafnia-zirconia: a comparison of model and experiment" *Nanoscale* 9, 9973-9986 (2017)

13. T. Moon, H. J. Jung, Y. J. Kim, M. H. Park, H. J. Kim, K. D. Kim, **<u>Y. H. Lee</u>**, S. D. Hyun, H. W. Park, S. W. Lee, C. S. Hwang "Research Update: Diode performance of the Pt/Al_2O_3/two-dimensional electron gas/$SrTiO_3$ structure and its time-dependent resistance evolution" *APL Materials* 5, 042301 (2017)

2. Conferences

1. **<u>Y. H. Lee</u>**, M. H. Park, H. J. Kim, T. Moon, K. D. Kim, S. D. Hyun, H. W. Park, Y. B. Lee, B. S. Kim, C. S. Hwang "Effective phase transformation kinetics of ferroelectric $Hf_{0.5}Zr_{0.5}O_2$ films by the presence of the top electrode" High-k oxides by ALD, Poland, March 7-10 (2018) poster

2. **<u>Y. H. Lee</u>**, M. H. Park, Y. J. Kim, H. J. Kim, T. Moon, K. D. Kim, S. D. Hyun, C. S. Hwang "Examination on the effects of various sputter deposition conditions on ferroelectric $Hf_{0.5}Zr_{0.5}O_2$ films" ISAF/ECAPD/PFM Conference 2016, Darmstadt, August 21-25 (2016) poster

3. **<u>Y. H. Lee</u>**, M. H. Park, Y. J. Kim, H. J. Kim, T. Moon, K. D. Kim, S. D. Hyun, C. S. Hwang "Preparation and characterization of ferroelectric $Hf_{0.5}Zr_{0.5}O_2$ films by RF-sputtering method" KJC-FE11, Sungkyunkwan University, Seoul, Korea, August 9-11 (2016) poster

4. **<u>Y. H. Lee</u>**, M. H. Park, Y. J. Kim, H. J. Kim, T. Moon, K. D. Kim, S. D. Hyun, C. S. Hwang "Characterization of Ferroelectric $Hf_{0.5}Zr_{0.5}O_2$ Films by RF-sputtering Method" 12th Korean Dielectric Symposium, Muju, January 1-February 2 (2016) poster

5. **<u>Y. H. Lee</u>**, M. H. Park, Y. J. Kim, H. J. Kim, T. Moon, K. D. Kim, S. D. Hyun, C. S. Hwang "Preparation and Characterization of Ferroelectric $Hf_{0.5}Zr_{0.5}O_2$ Films by RF-Sputtering Method" 23rd Korean Semiconductor Workshop, Kangwon,

February 22-24 (2016) poster

6. **Y. H. Lee** "RF Sputtering and Characterization of Ferroelectric $Hf_{0.5}Zr_{0.5}O_2$ Films" 1st International Symposium on Emerging Functional Materials, Songdo, November 4-6 (2015) poster

Y. H. Lee, M. H. Park, H. J. Kim, Y. J. Kim, T. Moon, K. D. Kim, C. S. Hwang "The Ferroelectric and Antiferroelectric Properties of HfO_2/ZrO_2 Nanolaminate Systems" ISAF-ISIF-PFM-2015, Singapore, May 24-27 (2015) poster

Abstract (in Korean)

2011년 독일 드레스덴에 있는 NaMLab 에서 강유전성을 보이는 HfO_2 물질을 처음 발표 한 후로부터 많은 연구가 진행 되어 왔다. 강유전성을 나타내는 $Pca2_1$ 상의 HfO_2 는 두께가 감소됨에 따라서 특성이 열화되는 기존 페로브스카이트 물질과 다르게 몇 nm 수준에서도 강유전성 특징을 보이기 때문에 scaling 과 3차원 구조 측면에서 강점을 갖고 기존 Si 공정에 잘 부합함에 따라 차세대 메모리 물질로 꼽힌다. 두께, 도펀트, 열처리 조건, 상부 전극 효과 및 열역학에 기반 된 제1원리 계산 등 강유전성을 나타내는 HfO_2 물질 거동의 원인에 대해서 많은 연구가 진행 되어 왔다. 하지만 동력학 측면에서는 많은 보고가 되어있지 않고 Ru 하부 전극을 사용한 실험 결과도 많이 보고 되어 오지 않았기 때문에 이 학위 논문에서는 위의 두 효과에 대해서 살펴보고자 한다.

열역학에 기반한 제1원리 계산 결과의 경우 계산 상수를 바꿔봐도 실험 결과와 일치하지 않는 한계점을 보인다. 이런 한계점을 극복하고자 동력학적인 측면에서 강유전성 발현 현상에 대해서 접근할 필요가 있다. 학위 논문 첫번째 파트에서는 Zr 도핑된 HfO_2 박막에서 열처리를 진행 할 때 tetragonal 상에서 monoclinic 상으로 상전이가 일어나는데 상부

전극의 존재 유무에 따른 activation energy 변화값을 구할 수 있다. 본 실험에서는 10 nm 의 $Hf_{0.5}Zr_{0.5}O_2$ 박막을 증착하여 TiN 상부 전극 증착 및 열처리 시간과 온도 조건에 따라서 상전이가 일어나는 정도를 X-ray 회절 분석법을 통해 구하며 Arrhenius plot 을 통해 activation energy 를 계산 할 수 있다. 고전적인 Johnson-Mehl-Avrami 모델으로 다결정인 $Hf_{0.5}Zr_{0.5}O_2$ 박막의 nucleation and growth 거동을 분석할 경우 한계점을 보였으며 새로 제안하는 nucleation-limited-transformation 모델을 사용하여 $Hf_{0.5}Zr_{0.5}O_2$ 박막의 nucleation and growth 성장 거동을 잘 대변할 수 있다.

두번째 파트에서는 Ru 하부 전극이 $Hf_{0.5}Zr_{0.5}O_2$ 박막에 미치는 영향에 대해 고찰한다. Ru 하부 전극 위에서 오존을 산화제로 사용하여 $Hf_{0.5}Zr_{0.5}O_2$ 박막을 원자층 증착법으로 증착할 때 초기 성장에서 rutile 상의 RuO_2 가 생기게 되는데 이는 tetragonal phase 와 lattice mismatch 가 크지 않아 local preferential 한 $Hf_{0.5}Zr_{0.5}O_2$를 성장시키고 비강유전성인 monoclinic phase 를 억제 시킨다. 한 방향으로 결정화가 잘 된 Ru 전극이 in-situ 결정화를 유도 하였으며 결과적으로 Ru 하부 전극 위에 증착 된 $Hf_{0.5}Zr_{0.5}O_2$ 박막의 경우 후 열처리 없이 결정화가 되는 거동을 보이는데 이는 TiN 하부 전극 위에 증착한 뒤 열처리 한 박막과 비슷한 잔류 분극 값을 보였다. 하지만 후 열처리가 없는 Ru 위

박막의 경우 높은 누설 전류를 보였으며 Al$_2$O$_3$ 를 삽입하여 누설 전류를 억제해도 fatigue 문제가 해결 되지 않았다. 이는 domain wall pinning 에 의한 결과이고 이에 대한 효과를 최소화 하고자 frequency 를 바꿔 측정 하였을 때 10^8 의 전계 사이클링에서 $17\,\mu\text{C/cm}^2$ 의 2P$_r$ 을 얻었다.